J. Mech. Phys. Solids 178 (2023) 105341

Contents lists available at ScienceDirect

Journal of the Mechanics and Physics of Solids

journal homepage: www.elsevier.com/locate/jmps

# Variational free energy based macroscopical modeling of ferroelectroelasticity

Felix Sutter *, Marc Kamlah

*Institute for Applied Materials, Karlsruhe Institute of Technology (KIT), Hermann-von-Helmholtz-Platz 1, 76344 Eggenstein-Leopoldshafen, Germany*

ARTICLE INFO

*Keywords:*
Ferroelectric materials
Free energy based framework
Incremental variational principles
Macroscopic material model
Microscopically motivated internal state variables
Mixed finite element methods

ABSTRACT

In this paper, a thermodynamically consistent minimum-type variational model for ferroelectric materials in a macroscopical continuum approach is presented. The motivation for this results from the lack of models in the literature that have on the one hand a Helmholtz free energy based variational structure and on the other hand are able to represent all important characteristic phenomena of ferroelectrics under quasi-static conditions. First of all, a unified variational theory for the material response of dissipative electro-mechanical solids in line with the framework of the generalized standard materials (GSM) is outlined. A macroscopic ferroelectric model with microscopically motivated internal state variables representing the switching processes taking place at the material microscale is adapted to the above mentioned variational structure. Additionally, a mixed variational principle for the global electro-mechanical boundary value problem is introduced in order to embed the Helmholtz free energy based local theory in a suitable finite element formulation. The solution processes for the resulting local and global variational problems is described in detail to enable easy implementation. The capability of the presented methods to reproduce the real behavior of ferroelectric systems is demonstrated by numerical examples. Here, a comparison to experimental results from the literature is a particular focus.

## 1. Introduction

Nowadays, so-called smart materials are used in many technical applications. One of the most important areas is sensing- and actuation applications, such as micro-electromechanical systems (MEMS) for high-precision positioning. The class of materials most commonly used in this technical field are ferroelectric ceramics, for instance, lead zirconate titanate (PZT) or barium titanate ($BaTiO_3$) (Setter and Waser, 2000). Due to their pronounced piezoelectric properties, they represent an optimal choice. For the development of technical systems with ferroelectrics, precise knowledge of their material behavior is required. In particular, the non-linear material behavior that occurs under the action of high electrical fields or mechanical stresses is of interest. Due to the switching processes of the domains occurring on the material microstructure, dissipative effects characterized by hysteretic material behavior play a decisive role. To predict the response of polycrystalline ferroelectric materials as realistically as possible, powerful material models are required. These models should be able to depict the electro-mechanically coupled behavior including all characteristic phenomena of ferroelectric ceramics, namely the dielectric hysteresis, butterfly hysteresis, ferroelastic hysteresis as well as mechanical depolarization behavior. In the literature, there is an abundance of approaches for the modeling of ferroelectric

* Corresponding author.
*E-mail addresses:* felix.sutter@kit.edu (F. Sutter), marc.kamlah@kit.edu (M. Kamlah).

https://doi.org/10.1016/j.jmps.2023.105341
Received 15 October 2022; Received in revised form 23 March 2023; Accepted 31 May 2023
Available online 13 June 2023

materials, which differ greatly in their degree of detail and their associated computational costs. However, the increasing level of detail does not guarantee that the ability to predict real material behavior increases.

### 1.1. Literature review on macroscopical ferroelectric material models

In this paper, we want to limit our focus to macroscopical continuum models which assume a smeared homogeneous representation of the material with averaged properties in the neighborhood of a material point. Models that contain spatially resolved considerations of the individual grains and domains, such as phase field approaches (Wang et al., 2004; Su and Landis, 2007), will not be considered here. Also, micro-electromechanical models (like e.g. in Hwang et al., 1995, Lu et al., 1999, Kessler and Balke, 2001 and Huber et al., 1999), requiring an enormous number of internal variables for simulating polycrystalline behavior, are not the subject of further discussion.

Those models based on a macroscopical continuum theory can be divided into two different categories. By *macroscopic phenomenological models* the experimentally observed material behavior for a ferroelectric polycrystal is reproduced. Here, the model constituents are often based on those used in classical plasticity theories. For the material memory, the dissipative effects are mapped using a limited number of internal variables. Typically, such models lack a physical link between the observed phenomena and the underlying mechanisms. Uniaxial phenomenological ferroelectric models are presented, for instance, in Cocks and McMeeking (1999), Kamlah and Tsakmakis (1999), Klinkel (2006b) and Laxman et al. (2018). More general multiaxial formulations can be found in McMeeking and Landis (2002), Landis (2002a), Kamlah and Böhle (2001), Schwaab et al. (2012), Klinkel (2006a), Linnemann et al. (2009), Schröder and Romanowski (2005), Miehe and Rosato (2011), Elhadrouz et al. (2005, 2006), Zouari et al. (2011), Maniprakash et al. (2016a,b) and Maniprakash (2016), among others. Detailed reviews about macroscopic phenomenological models are given in Kamlah (2001) and Landis (2004). Discussions about some aspects of the modeling framework as well as implementation details can be found in Stark et al. (2016) and Semenov et al. (2010).

The second category of models, which is a particular focus of this paper, corresponds to an intermediate approach of phenomenological macroscopic models that incorporate additional information from microscopic mechanisms in the material into their approaches. First, Kamlah and Jiang (1999) presented such a *microscopically motivated model* by introducing internal state variables containing information of an averaged domain state at the microscopic scale. The macroscopic quantities remanent polarization and remanent strain can then be derived from the microscopically motivated internal variables. Later, a multiaxial generalization was done by Kamlah and Wang (2003a) and a finite element implementation was realized in Laskewitz and Kamlah (2010) and Laskewitz (2007) including a discussion on the occurring numerical problems. Based on these works, Mehling et al. (2007) and Mehling (2007) introduced a modified version of this model with a slightly different choice of microscopically motivated internal variables. Further models for ferroelectric materials that are dealing with similar 'hybrid' approaches in a macroscopic framework are given by Stark et al. (2016a,b) and Idiart and Bottero (2020).

In the following, a selection of (from the authors' point of view) very important aspects in the non-linear modeling of ferroelectric materials in terms of computational stability and applicability to real-world problems will be discussed. In this context, an attempt is made to classify the models available in the literature with regard to the different aspects (see also Fig. 1).

#### 1.1.1. Variational formulation

In order to deal with the problem that is to be solved within a material model as well as possible and to enable a very efficient solution process, some models can be embedded in a variational structure. To achieve such a variational structure, one can use the framework of the *generalized standard materials (GSM)* (Halphen and Nguyen, 1975). In line with this, Miehe et al. (2011) as well as Mielke and Timofte (2006) present a unified theory based on incremental variational principles for electro-mechanical coupled problems also including dissipative effects. The big advantage of using this framework is that the problem is reduced to solving a non-linear optimization problem, which can be done with modern numerical methods straight forward in a very efficient way. Due to the local problem being related to a potential, a symmetrical algorithmic material tangent of the model is guaranteed at all times, which makes also the solution process of the global problem by finite element method significantly more efficient. However, the advantages of a variational formulation of the material model and the associated improvement in computational stability and efficiency have so far only been very rarely exploited in the field of ferroelectrics. Ferroelectric material models embedded into a variational structure are given e.g. in Miehe and Rosato (2011), Pechstein et al. (2020), Meindlhumer et al. (2021), Pechstein et al. (2021) and Idiart and Bottero (2020).

#### 1.1.2. Thermodynamical potential

To be able to predict the material behavior as physically plausible as possible, material models should be formulated thermodynamically consistent. The first basic concept of a thermodynamically consistent model for ferroelectric materials was given by Bassiouny et al. (1988). An important aspect in the thermodynamically consistent modeling of electro-mechanical problems is the selection of the underlying energy form. These differ in the choice of the *independent variables*. The most popular option is the *electric Gibbs energy* $G_2(\boldsymbol{\varepsilon}, \vec{E})$ using the strain state and the electric field as the independent variables, which is most suitable for the implementation into a finite element code. Unfortunately, such a formulation provides a *convex-concave* saddle-point structure of the underlying variational principle and thus also leads to a non-positive definite material tangent of the model, see also the discussion in Miehe et al. (2011). Thermodynamically consistent ferroelectric material models formulated in terms of the electric Gibbs energy are outlined e.g. in Mehling et al. (2007), Klinkel (2006a), Linnemann et al. (2009), Schröder and Romanowski (2005), Miehe and Rosato (2011), Maniprakash et al. (2016a,b) and Maniprakash (2016). The most convenient choice for a pure material point

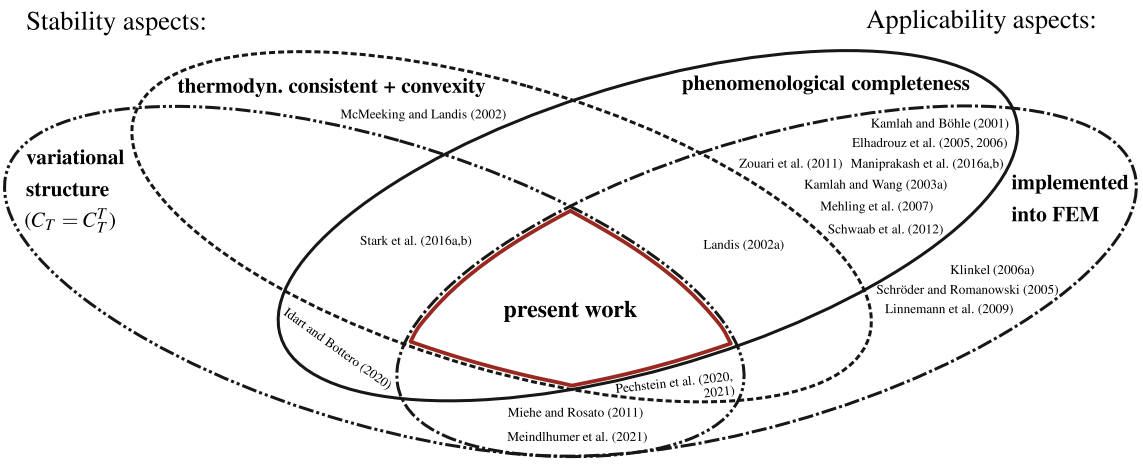


**Fig. 1.** Classification of multiaxial macroscopic ferroelectric continuum models selected from the literature with regard to aspects of numerical stability and applicability to real engineering problems. The authors point out that the present illustrations do not claim to be complete, but are only intended to show a representative trend.

consideration is a formulation based on *Gibbs free energy* $G(\boldsymbol{\sigma}, \vec{E})$. Here, the choice of the *intensive* quantities as independent variables, i.e. mechanical stress and electric field, are the easiest way to predefine an input state. A corresponding variational principle has a pure maximization structure. Embedding such models in finite element environments requires more sophisticated mixed element formulations, see e.g. in Sze and Pan (1999), Cannarozzi and Ubertini (2001) and Pechstein et al. (2018). Models based on Gibbs free energy are given in Kamlah and Jiang (1999), Kamlah and Wang (2003a), Meindlhumer et al. (2021) and Idiart and Bottero (2020). From the thermodynamical point of view, the canonical and the most favorable formulation of a ferroelectric material model is based on the *Helmholtz free energy* $\psi(\boldsymbol{\varepsilon}, \vec{D})$. Its variational principle in terms of both *extensive* quantities strain and the electric displacement provides a pure *convex* minimization structure and therefore a positive definite linear material tangent of the model. This characteristic has the big advantage of a unique solution and therefore a stable constitutive material response (Miehe et al., 2011). A drawback of using such a formulation is the non-straightforward integration into a suitable finite element formulation which is certainly the reason why only a minority of the existing models are formulated in Helmholtz free energy. In McMeeking and Landis (2002), Landis (2002a), Stark et al. (2016a,b) and Pechstein et al. (2020, 2021) thermodynamically consistent models based on Helmholtz free energy are presented. For more information about the different energy forms and their relations defined by partial Legendre transformations can be found in Ikeda (1996).

### *1.1.3. Considered characteristic effects*

The applicability of a model can be judged by its phenomenological completeness. This refers to the ability of a fully multiaxial model to represent the properties characteristic of ferroelectric materials. These are the dielectric, the butterfly and the ferroelastic hystereses, as well as the mechanical depolarization behavior. In addition, the rotation of the polarization direction should be depictable by the model. However, in this discussion, we want to neglect the rate-dependency of these effects (e.g. considered in Miehe and Rosato, 2011 and Maniprakash et al., 2016b), as well as temperature dependency (e.g. Maniprakash, 2016) and we want to restrict ourselves to quasi-static loading conditions. A frequently made simplification is the neglection of the isolated ferroelastic hysteresis behavior, realized by direct coupling of the irreversible strain to the irreversible polarization, as assumed e.g. in McMeeking and Landis (2002), Schröder and Romanowski (2005), Linnemann et al. (2009), Miehe and Rosato (2011), Pechstein et al. (2020, 2021) and Meindlhumer et al. (2021). The ferroelastic behavior, however, has a non-negligible influence on the overall domain switching effects in ferroelectrics and should be included in a more sophisticated model. Furthermore, in Klinkel (2006a) and Linnemann et al. (2009), for example, it is assumed that the polarization can only arise along a given direction. This makes it impossible to account for a rotation of the polarization direction. Models that can represent the complete range of phenomenological material behavior mentioned here can be found in e.g. Landis (2002a), Kamlah and Böhle (2001), Schwaab et al. (2012), Kamlah and Wang (2003a), Mehling et al. (2007), Mehling (2007), Stark et al. (2016a,b), Maniprakash et al. (2016a,b) and Maniprakash (2016).

### *1.1.4. Suitable finite element formulation*

Another important aspect for the possible applicability of a material model for solving engineering problems is a simple implementation in a finite element environment. In this context, the selection of a suitable finite element formulation to solve the global electro-mechanically coupled boundary value problem plays a crucial role. The most primitive and at the same time also the most frequently used is a formulation using the displacement and the electric scalar potential as degrees of freedom, which was first proposed by Allik and Hughes (1970). The same formulation can be derived by a variational principle using the electric Gibbs energy in the variational potential, which demonstrates that it is particularly suitable for models based on this energy form. This

formulation is very easy to implement, but has some disadvantages due to the underlying saddle point problem (cf. Section 1.1.2). The resulting non-positive definite tangential stiffness matrix can lead to convergence problems, especially in the case of non-linear material behavior, see e.g. Stark et al. (2013). Works in which ferroelectric material models implemented in such a finite element formulation are e.g. Kamlah and Böhle (2001), Laskewitz and Kamlah (2010), Laskewitz (2007), Klinkel (2006a), Linnemann et al. (2009), Schröder and Romanowski (2005), Miehe and Rosato (2011), Mehling (2007), Elhadrouz et al. (2006), Zouari et al. (2011), Maniprakash et al. (2016b) and Maniprakash (2016). In order to circumvent this problem mentioned before, Landis (2002b) proposed a two-dimensional finite element formulation by introducing an electric vector potential as electrical degrees of freedom instead of the scalar potential. Since the electric displacement can then be determined directly from the vector potential, this formulation perfectly fits a material model based on the Helmholtz free energy. A more general three-dimensional formulation was presented by Semenov et al. (2006). However, such a formulation has certain disadvantages. The definition of the boundary conditions for the vector potential is far from obvious and in the general three-dimensional case, an additional gauging term in the variational potential is necessary to ensure a unique solution (Semenov et al., 2006; Stark et al., 2015). Detailed investigations on a finite element implementation of the model in Landis (2002a) into a vector potential formulation can be found in Semenov et al. (2010). Ghandi and Hagood (1997) proposed a mixed formulation using the constitutive relations resulting from a Helmholtz free energy based material description. The corresponding electrical degrees of freedom are the electric displacement vector and the electric scalar potential. The derivation of the same formulation based on a variational principle is shown e.g. in Gil and Ortigosa (2016). Therein the electric Gibbs energy is expressed by a partial Legendre transformation in terms of the Helmholtz free energy. This formulation has, on the one hand, the advantage that it fits a material model based on the Helmholtz free energy (with its convex properties), and on the other hand, the presence of the electric scalar potential as degree of freedom allows a simple definition of the electrical boundary conditions. The disadvantage of this formulation compared to a vector potential formulation is again the intrinsic saddle point structure which stays preserved by its derivation from an electric Gibbs potential. Applications of this finite element formulation in connection with ferroelectric material models can also be found in Schwaab et al. (2012), Kurzhöfer and Schröder (2006) and Streich et al. (2022). A plethora of other mixed finite element formulations for electro-mechanically coupled problems can be found in Sze and Pan (1999), Cannarozzi and Ubertini (2001), Gil and Ortigosa (2016), Ortigosa and Gil (2016), Miehe et al. (2015) and Klinkel and Wagner (2006, 2008), among others. A detailed review of piezoelectric finite element formulations is given by Benjeddou (2000). Finally, it should be mentioned that it has by far not been shown for all models in the literature whether an implementation in a finite element code is meaningful or even possible as they might be too complex for this. Furthermore, an analytical material tangent is not provided for some models and it can be doubted whether this exists at all, which implies that an expensive numerically calculated tangent must be used.

### 1.2. Motivation and content of the present work

In the preceding discussion of macroscopical ferroelectric material models available in the literature with regard to aspects of numerical stability and applicability, it appears that none of the models provenly possess all of the (from the authors' point of view) important properties considered here, cf. also Fig. 1. Thus, to the best of the authors' knowledge, no macroscopic ferroelectric material model exists which 1) has a variational structure, 2) is formulated thermodynamically consistent in terms of the convex Helmholtz free energy, 3) has the ability to represent all important non-linear characteristic phenomena of ferroelectrics, and at the same time 4) is provenly appropriate to be efficiently incorporated into a suitable finite element formulation. In order to close this gap, we introduce in this paper a thermodynamically consistent model in line with those presented in Mehling et al. (2007) and Kamlah and Wang (2003a), but for the first time formulated in terms of Helmholtz free energy and adapted to achieve a symmetric variational structure in the fashion of a generalized standard material. Furthermore, based on the concept presented in Miehe et al. (2011) a highly efficient solution process for the model is obtained by formulation as an incremental variational principle, appearing as a minimization problem due to its convex properties by construction. Moreover, an analytical expression for the symmetric algorithmic material tangent can be derived directly from it. Suitable to this introduced variational model, a mixed finite element formulation initially presented in a large strain framework in Gil and Ortigosa (2016), Ortigosa and Gil (2016) is used to solve the global electro-mechanically coupled boundary value problem. Here it is demonstrated for the first time that this formulation is also ideally appropriate for problems with dissipative effects. The applicability of the presented modeling framework for real-world problems is demonstrated by selected numerical examples. A comparison to experimental results from the literature is a special focus in order to demonstrate the ability of the model to represent all important characteristic phenomena that can be observed in ferroelectric materials. The authors provide the reader with all the necessary details for the implementation of the presented theory.

## 2. Variational formulation of the local material response in dissipative electro-mechanical solids

We consider a material point element of an electro-mechanically coupled continuum with linearized kinematics of small deformations and assume only quasi-static loading scenarios with vanishing inertia effects. In this paper, we restrict ourselves to a class of non-conductive materials with no available free charges and no magnetic effects. The temperature is assumed to be uniform and to stay constant for all processes under consideration. The external loading state of the material point can be described by the mechanical stress tensor $\boldsymbol{\sigma}$ and the electric field vector $\vec{E}$, acting at this certain point in the continuum. From the thermodynamical point of view, these external driving forces represent the *intensive* quantities. They change the thermodynamic state of the system under consideration. This is noticeable through a change in the *extensive* quantities, more precisely the infinitesimal strain tensor $\boldsymbol{\varepsilon}$ and the electric displacement vector $\vec{D}$.

### 2.1. Internal state variables formulation for dissipative electro-mechanical processes

Dissipative processes in electro-mechanically solids take place if the energy supplied from the environment is not completely stored in reversible manner in the material. Such dissipative processes have the restriction to fulfill the second law of thermodynamics (cf. Maugin, 1988)

$$\mathcal{D} := \boldsymbol{\sigma} : \dot{\boldsymbol{\varepsilon}} + \vec{E} \cdot \dot{\vec{D}} - \dot{\psi} \geq 0 \,, \tag{1}$$

commonly called the *Clausius-Duhem* inequality. In this expression, the energy dissipation $\mathcal{D}$ has to stay positive for arbitrary processes. This statement is a physical restriction in order to ensure a realistic material behavior of non-negative entropy production. The energy storage per material unit volume in (1) is described by the *Helmholtz free energy density*[1] $\psi(\boldsymbol{\varepsilon}, \vec{D})$. Its expression in terms of the extensive quantities provides a convex structure of the energy landscape, see e.g. Miehe et al. (2011). The first two terms on the right hand side in (1) act as an external energy supply at the point in the solid under consideration. Detailed foundations of the thermodynamics of electro-mechanical solids can be found in Maugin (1988) and Maugin (1993), among others.

By following the popular concept outlined e.g. in Coleman and Gurtin (1967) and Lubliner (1972), the dissipative effects in the material can be represented by a set of (at his point unknown) internal state variables $\mathfrak{q}$. With these variables, the material point is equipped with a memory of the loading history. In order to incorporate these dissipative effects in the outlined framework, the Helmholtz free energy per unit volume $\psi(\boldsymbol{\varepsilon}, \vec{D}, \mathfrak{q})$ is now assumed to be a function of the internal state variables, additionally. By insertion of the time derivative in (1), we end up with the expression

$$\mathcal{D} = (\boldsymbol{\sigma} - \partial_{\boldsymbol{\varepsilon}}\psi) : \dot{\boldsymbol{\varepsilon}} + (\vec{E} - \partial_{\vec{D}}\psi) \cdot \dot{\vec{D}} - \partial_{\mathfrak{q}}\psi \cdot \dot{\mathfrak{q}} \geq 0 \tag{2}$$

for the dissipation. From (2), we can motivate as sufficient conditions the constitutive equations for the stress tensor $\boldsymbol{\sigma}$ and the electric field vector $\vec{E}$. By assuming these relations, the *Clausis-Duhem* inequality (1) can be reduced to

$$\mathcal{D} = -\partial_{\mathfrak{q}}\psi \cdot \dot{\mathfrak{q}} \geq 0 \tag{3}$$

where $\partial_{\mathfrak{q}}\psi$ in the following is called the energetic internal driving forces. Obviously, these more theoretically motivated forces are acting here as work conjugated quantities to the internal variables $\mathfrak{q}$. An always challenging task in modeling dissipative material behavior, is to find a suitable description of how the evolution of the internal state variables takes place. Such an evolution law has to fulfill the physical restriction to produce a non-negative dissipation in (3) for arbitrary processes.

### 2.2. Incremental variational principles for the local dissipative material response

To derive a proper description for the evolution of the internal state variables $\mathfrak{q}$ and to embed the outlined thermodynamic framework introduced in Section 2.1 into a variational structure, we utilize the theory of the *generalized standard materials (GSM)* (Halphen and Nguyen, 1975). Therefore we assume the existence of a local rate-type potential (cf. Simo and Honein, 1990; Ortiz and Stainier, 1999; Radovitzky and Ortiz, 1999; Miehe et al., 2011)

$$\pi(\boldsymbol{\varepsilon}, \vec{D}, \mathfrak{q}) := \underbrace{\psi(\boldsymbol{\varepsilon}, \vec{D}, \mathfrak{q}) - \psi(\boldsymbol{\varepsilon}_n, \vec{D}_n, \mathfrak{q}_n) + \Delta t \phi(\tfrac{1}{\Delta t}(\mathfrak{q} - \mathfrak{q}_n))}_{\pi^{int}(\boldsymbol{\varepsilon}, \vec{D}, \mathfrak{q})} \underbrace{- \boldsymbol{\sigma} : (\boldsymbol{\varepsilon} - \boldsymbol{\varepsilon}_n) - \vec{E} \cdot (\vec{D} - \vec{D}_n)}_{\pi^{ext}(\boldsymbol{\varepsilon}, \vec{D})} . \tag{4}$$

in an algorithmic representation with an approximation of the rates using the differential quotient $\dot{x} \approx (x - x_n)/\Delta t$. This procedure changes a time-continuous problem to a sequence of incremental problems, each characterized by a minimum principle (Ortiz and Stainier, 1999). To keep the notation as simple as possible the subscript for quantities evaluated at time $t_{n+1}$ are omitted here. The material state at time $t_n$ is assumed to be completely known. Note that in the algorithmic representation in (4), a constant rate of internal state variables within the interval $\Delta t$ is assumed and the external loadings $(\boldsymbol{\sigma}, \vec{E})$ are prescribed implicitly at time $t_{n+1}$ (Miehe et al., 2011). The dissipative contributions to (4) are represented by a dissipation potential $\phi$, which is assumed to depend on the rate of the internal state variables. Note here, that the constraint of the production of positive dissipation in (3) is a priori satisfied by a convex, normalized and non-negative dissipation potential (cf. Miehe, 2002). The specific construction of the dissipation potential $\phi$ used in this work is discussed in Section 4.

Considering the convex properties of the Helmholtz free energy function in (4), a constitutive variational principle for dissipative electro-mechanical material behavior can be formulated by the pure minimization problem (cf. Miehe et al., 2011)

$$\{\boldsymbol{\varepsilon}, \vec{D}, \mathfrak{q}\} = \text{Arg}\left\{ \inf_{\boldsymbol{\varepsilon}} \inf_{\vec{D}} \inf_{\mathfrak{q}} \pi(\boldsymbol{\varepsilon}, \vec{D}, \mathfrak{q}) \right\} \tag{5}$$

for the evaluation of the material state at time $t_{n+1}$. Due to the fact that only the internal part $\pi^{int}$ of the incremental potential in (4) depends on the internal state variables $\mathfrak{q}$, their evaluation can be done independently of the external part $\pi^{ext}$. Therefore the

[1] Helmholtz free energy can be derived performing a Legendre transformation from internal energy $e(\boldsymbol{\varepsilon}, \vec{D}, \eta)$ by a variable change of temperature $\theta$ and entropy $\eta$: $\psi(\boldsymbol{\varepsilon}, \vec{D}, \theta) = \inf_{\eta}\{e(\boldsymbol{\varepsilon}, \vec{D}, \eta) - \theta\eta\}$. In this work, only isothermal processes are under consideration.

solution process can be performed in two steps. A first variational sub-problem updating the internal state variables can then be written as (cf. Miehe et al., 2011)

$$\mathfrak{q} = \text{Arg}\left\{ \inf_{\mathfrak{q}} \pi^{int}(\boldsymbol{\varepsilon}, \vec{D}, \mathfrak{q}) \right\}. \tag{6}$$

We can interpret this relation such that the internal state variables $\mathfrak{q}$ follow during the time increment $\Delta t$ an optimum path in the sense of a minimum problem. Note here the advantages of this algorithmic representation of the local material response. It becomes a very simple optimization problem by discrete evaluation at the end of the finite time increment $t_{n+1}$. By employing the stationarity condition $\delta_{\mathfrak{q}} \pi^{int}(\boldsymbol{\varepsilon}, \vec{D}, \mathfrak{q}) = 0$ of the argument in (6), we end up with the algorithmic representation

$$\boxed{\partial_{\mathfrak{q}} \psi(\boldsymbol{\varepsilon}, \vec{D}, \mathfrak{q}) + \Delta t \partial_{\mathfrak{q}} \phi(\tfrac{1}{\Delta t}(\mathfrak{q} - \mathfrak{q}_n)) = 0} \tag{7}$$

of the commonly called *Biot equation* (Biot, 1965). This relation ensures the equilibrium of the energetic internal driving forces in (3) and the dissipative internal driving forces $\Delta t \partial_{\mathfrak{q}} \phi$ for arbitrary processes. It acts as an additional constitutive differential equation and determines the evolution of the internal state variables (Miehe, 2002). Due to the local character of the internal state variables $\mathfrak{q}$, the evaluation of their evolution equations in (7) can be done at each material point in the continuum independently.

For the optimization of the incremental potential (4) with respect to strain $\boldsymbol{\varepsilon}$ and electric displacement $\vec{D}$, we introduce the reduced incremental internal work potential per unit volume (cf. Miehe et al., 2011)

$$W(\boldsymbol{\varepsilon}, \vec{D}) = \inf_{\mathfrak{q}} \left\{ \pi^{int}(\boldsymbol{\varepsilon}, \vec{D}, \mathfrak{q}) \right\}. \tag{8}$$

With the definition in (8) at hand, the remaining part of the solution of the initially introduced optimization problem in (5) can be written in an algorithmic manner as the constitutive variational principle

$$\{\boldsymbol{\varepsilon}, \vec{D}\} = \text{Arg}\left\{ \inf_{\boldsymbol{\varepsilon}, \vec{D}} \left\{ W(\boldsymbol{\varepsilon}, \vec{D}) - \pi^{ext}(\boldsymbol{\varepsilon}, \vec{D}) \right\} \right\}. \tag{9}$$

By evaluation of the stationarity conditions of the optimization problem (9), we can derive an algorithmic representation of the current state of the stress and the electric field in the form of

$$\boxed{\boldsymbol{\sigma} = \partial_{\boldsymbol{\varepsilon}} W(\boldsymbol{\varepsilon}, \vec{D}) \qquad \text{and} \qquad \vec{E} = \partial_{\vec{D}} W(\boldsymbol{\varepsilon}, \vec{D})} \tag{10}$$

for the material point under consideration. Note here that in contrast to the Helmholtz free energy $\psi(\boldsymbol{\varepsilon}, \vec{D}, \mathfrak{q})$ in (4) the reduced incremental internal work potential $W(\boldsymbol{\varepsilon}, \vec{D})$ is not a function of the internal state variables $\mathfrak{q}$, since they themselves have been determined in dependence on $\boldsymbol{\varepsilon}$ and $\vec{D}$ through (6), before. Therefore the evaluation of the constitutive equations in (10) at time $t_{n+1}$ formally becomes a quasi-hyperelastic function evaluation (Miehe, 2002).

The introduced incremental variational structure allows the computation of consistent and symmetric algorithmic material tangent moduli at time $t_{n+1}$ by building the second-order derivatives

$$\mathbb{C}_T := \begin{bmatrix} \partial_{\boldsymbol{\varepsilon}} \boldsymbol{\sigma} & \partial_{\vec{D}} \boldsymbol{\sigma} \\ \partial_{\boldsymbol{\varepsilon}} \vec{E} & \partial_{\vec{D}} \vec{E} \end{bmatrix} = \begin{bmatrix} \partial^2_{\boldsymbol{\varepsilon}\boldsymbol{\varepsilon}} W & \partial^2_{\boldsymbol{\varepsilon}\vec{D}} W \\ \partial^2_{\vec{D}\boldsymbol{\varepsilon}} W & \partial^2_{\vec{D}\vec{D}} W \end{bmatrix} \tag{11}$$

of the reduced incremental internal work potential (8). A condition for a stable electro-mechanical material behavior is given by a non-negative algorithmic representation of the second-order work expression (cf. Miehe et al., 2011)

$$\Delta\boldsymbol{\sigma} : \Delta\boldsymbol{\varepsilon} + \Delta\vec{E} \cdot \Delta\vec{D} = \begin{bmatrix} \Delta\boldsymbol{\varepsilon} \\ \Delta\vec{D} \end{bmatrix} \cdot \mathbb{C}_T \cdot \begin{bmatrix} \Delta\boldsymbol{\varepsilon} \\ \Delta\vec{D} \end{bmatrix} \geq 0 \qquad \text{for all} \qquad \begin{bmatrix} \Delta\boldsymbol{\varepsilon} \\ \Delta\vec{D} \end{bmatrix} \neq \mathbf{0} \tag{12}$$

and can be satisfied for positive definite material tangent moduli in (11). Due to the definition of the rate-type potential (4) in terms of the convex Helmholtz free energy function $\psi$ and the assumption of a convex dissipation potential $\phi$, the reduced incremental internal work potential $W$ has a bifurcation- and limit point-free convex structure[2], too. This characteristic ensures the basic requirements for the positive definiteness of $\mathbb{C}_T$ and guarantees the uniqueness of the constitutive relations derived in (10) for arbitrary loading processes (Miehe et al., 2011; Gil and Ortigosa, 2016).

The presented properties of the reduced incremental internal work potential $W$ demonstrate that it has actually a potential character. This was achieved through a consistent variational formulation of the material behavior by using the framework of the generalized standard materials. Based on this, the construction of functionals with potential character for the whole electro-mechanical body under consideration in order to achieve a variational structure for the solution of the global boundary value problem becomes possible, see Section 5.

[2] As already mentioned, a frequently chosen formulation of ferroelectric material models is based on the convex-concave electric Gibbs energy density saddle-point function $G_2(\boldsymbol{\varepsilon}, \vec{E}) = \inf_{\vec{D}}\{\psi(\boldsymbol{\varepsilon}, \vec{D}) - \vec{E} \cdot \vec{D}\}$ (cf. Ikeda, 1996) in order to describe the energy storage of the system. Such a formulation leads to non-positive definite material tangent moduli (Miehe et al., 2011; Landis, 2002b).

## 3. Material model with microscopically motivated internal state variables

For the description of the non-linear hysteretic electro-mechanical behavior of ferroelectric materials, we want to follow a modeling approach initially introduced in a simplified one-dimensional formulation by Kamlah and Jiang (1999). In this Gibbs free energy based approach (cf. Ikeda, 1996), microscopically motivated internal state variables are introduced in order to represent history dependence and the dissipative effects occurring in a material point element of a continuum. Later a more general multiaxial formulation was realized by Kamlah and Wang (2003a) and a finite element implementation was done by Laskewitz and Kamlah (2010). In the same fashion, Mehling et al. (2007) introduced a model based on electric Gibbs energy with a slightly different choice of microscopically motivated internal state variables.

The subject of the present section is the presentation of a model variant in line with the already existing approaches outlined above and fitting this into the Helmholtz free energy based variational framework introduced in Section 2.

### 3.1. Microscopical description of ferroelectric materials

Below the Curie temperature, a lattice structure with tetragonal unit cells can be observed in ferroelectric materials on the atomistic length scale. A preferred orientation of such a unit cell is characterized by its c-axis $\vec{c}$, which can be up to a few per cent larger than its a-axis (Jaffe et al., 1971), cf. Fig. 2 a). This distortion with respect to a cubic unit cell in the paraelectric state is defined by the spontaneous strain tensor $\boldsymbol{\varepsilon}^s$. Due to a shift of the positive and negative charge centers a spontaneous net polarization $\vec{p}^s$ is acting as a microdipole in each unit cell and causes in the piezoelectric properties.

A basic feature of ferroelectric materials is the switchability of the orientation of the c-axes and the spontaneous polarization vectors under the action of external mechanical stresses or electrical fields. Here 180° and 90° switchings are two possible scenarios. During 180° switchings the orientation of the spontaneous polarization vector $\vec{p}^s$ changes, but the alignment of the $c$-axis remains untouched. In contrast to this, 90° switchings come along with a rotation of the $c$-axis, and therefore, with an assumed volume preserving change in the state of spontaneous strain $\boldsymbol{\varepsilon}^s$ of the unit cell. It should be emphasized that while 90° switchings can be caused by electric fields and mechanical stresses, 180° switchings can only be realized by electric fields (Moulson and Herbert, 1990). Note here, in such considerations on unit cell level the $c$-axis $\vec{c}$ and the vector of the spontaneous polarization $\vec{p}^s$ are assumed to be always in parallel.

The grains of the polycrystalline microstructure of ferroelectric materials are subdivided into domains containing a certain amount of unit cells with equal spontaneous polarization, see Fig. 2 b). Theoretical considerations suggest that in-between the polarization orientation of two neighboring domains of a grain, a 90° or 180° angle occurs in order to minimize the energy (Moulson and Herbert, 1990). During external mechanical or electrical loadings, the domains cannot all be aligned into the prescribed loading direction due to their unavoidable interaction in the polycrystal. This is the reason why it is not possible to experimentally measure on the macroscopic scale a remanent polarization/strain in the order of magnitude of the theoretical spontaneous polarization/strain of a unit cell (Jaffe et al., 1971; Moulson and Herbert, 1990). Furthermore, averaged orientations of the c-axes $\vec{c}$ and the spontaneous polarization vector $\vec{p}^s$ over a region containing a sufficiently large number of grains would not necessarily deliver the coaxiality observed on the atomistic level. To incorporate the influence of the microscopical material state on the macroscopical measurable quantities into a modeling approach, meaningful considerations are needed for their approximative description.

### 3.2. Microscopically motivated internal state variables

In Section 2.1 a set of internal state variables is introduced in a macroscopic continuum theory for the representation of dissipative effects caused by microstructural processes. For their identification, we should keep in mind the phenomenological considerations outlined in Section 3.1. For a representation of the material state of ferroelectrics, information about micromechanical structural deformations caused by domain switching and the associated changes in the remanent polarization state are required. For this purpose, quantities have to be introduced representing these two properties in an averaged sense for a material point element containing a volume with a sufficiently large number of grains and domains.

To motivate the characterization of the microstructural deformations, we follow the approach initially introduced in Kamlah and Jiang (1999) and utilize the information of the c-axes orientations of the crystal unit cells on the atomistic scale. The $c$-axis of a unit cell can then be described by the unit vector

$$\vec{c}(\vartheta,\varphi)=\begin{bmatrix}\sin\vartheta\cos\varphi\\ \sin\vartheta\sin\varphi\\ \cos\vartheta\end{bmatrix}\qquad\text{with}\qquad \|\vec{c}\|=1 \tag{13}$$

in dependence on the two Euler angles $\vartheta$ and $\varphi$ (Mehling et al., 2007). Each of these orientation vectors $\vec{c}$ is pointing from the origin of a spherical coordinate system to the surface of a unit sphere in Euclidian space. We may now consider the mapping of the orientation vectors of all c-axes of a representative material volume onto a unit sphere. Then for certain directions in this sphere, a higher density of c-axes would possibly be recognizable due to preferable alignments of unit cells in the material volume under consideration. Such thought experiments motivate the definition of a function that describes the distribution of the orientations of the c-axes in the spherical space. For this purpose, a continuous *orientation distribution function*[3] *(ODF)* (cf. Mehling et al., 2007)

$$\hat{F}(\vartheta,\varphi,\boldsymbol{A}) := k_n^F\,\vec{c}\cdot\boldsymbol{A}\cdot\vec{c} \tag{14}$$

[3] Note here the quadratic trigonometric character of this form of the *ODF* cf. (13).

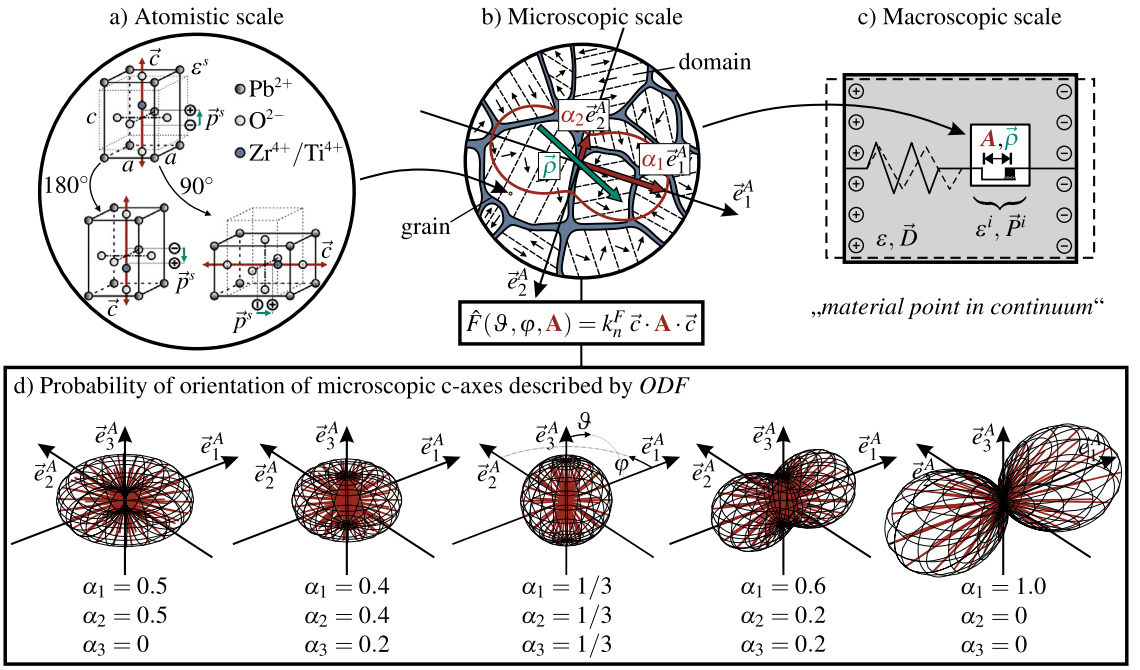


**Fig. 2.** a) Atomistic unit cell configurations of ferroelectric materials with switchable $c$-axis orientation $\vec{c}$ and spontaneous polarization $\vec{p}^s$. b) Material point containing a representative number of grains and domains of the polycrystal while the microscopically motivated internal state variables $\boldsymbol{A}$ and $\vec{\rho}$ represent an averaged state of the microstructure. c) Simplified one-dimensional material point unit element on the macroscopical continuum scale after unloading process with remained macroscopical remanent strain and polarization represented by microscopically motivated internal state variables. d) Variety representations of the orientation distribution function (*ODF*) for several combinations of texture tensor eigenvalues $\alpha_i$.

is introduced representing the probability that a $c$-axis in the volume of a material point is oriented in a certain direction. In this *ODF*, the positive scalar value $k_n^F$ is a normalization factor that is yet to be determined. Indeed the basic characteristics in (14) are given by the symmetrical second-order *texture tensor* $\boldsymbol{A}$ describing the spatial arrangement and distribution of the c-axes for the material point element under consideration. With this tensor at hand, we identified the first microscopically motivated internal state variable

$$\mathfrak{q}_1 := \boldsymbol{A} = \sum_{i=1}^{3} \alpha_i \, \vec{e}_i^{\,A} \otimes \vec{e}_i^{\,A} \tag{15}$$

representing the c-axes orientations of the microstructure (Mehling et al., 2007). In (15) the texture tensor is defined by a spectral decomposition in terms of its eigenvalues $\alpha_i$ and the eigenvectors $\vec{e}_i^{\,A}$. Physically the first (third) eigenvalue can be interpreted as the fraction of c-axes oriented in the most (least) preferable direction indicated by the first (third) eigenvector. With this information, the polycrystalline texture of a material point is characterized in an approximative manner, see Fig. 2 d).

In order to satisfy certain constraints motivated by probabilistic and physical considerations, some restrictions have to be obeyed for the *ODF* (for more details see Mehling et al., 2007). With the assumptions $\alpha_i \geq 0$, $\mathrm{tr}(\boldsymbol{A}) = 1$ and $k_n^F = \frac{3}{4\pi}$ a 'virgin' material state after the sintering process represented by a uniform distribution of the c-axes over the whole unit sphere can be specified as

$$\boldsymbol{A}_0 = \frac{1}{3}\boldsymbol{I}, \tag{16}$$

with the second-order identity tensor $\boldsymbol{I}$, cf. Fig. 2 d) middle.

As mentioned before, the texture tensor and the therein encoded information about preferable orientations of the c-axes of crystal unit cells is not sufficient to fully characterize the macroscopic state of a material point in a ferroelectric. As an example, this can be seen for cases where reorientation of the polarization state occurs without any changes of c-axes alignment, as for 180° switching processes. Therefore a second microscopically motivated internal state variable has to be introduced in order to capture additional information. The direction of the *relative polarization vector*

$$\mathfrak{q}_2 := \vec{\rho} \qquad \text{with} \qquad 0 \leq \|\vec{\rho}\| \leq 1 \tag{17}$$

indicates the preferred orientations of the microdipols in the volume occupied by a material point and its absolute magnitude represents the fraction of unit cells oriented in this direction. The natural upper limit in (17) for the relative polarization vector represents a configuration where all unit cells are oriented in the same direction. On a macroscopic level, one can connect such a state to the saturation value of a polarization averaged over a material point volume.

### 3.3. Connection to macroscopic scale

In the next step, the microscopically motivated internal state variables introduced in Section 3.2 should be embedded in a theory based on macroscopic quantities. A phenomenological framework originally motivated from the theory of elasto-plasticity serves here as a well-established foundation, see e.g. Kamlah (2001), Landis (2004) and the references therein. Inline with this, we may assume an additive split for the electric displacement vector and infinitesimal strain tensor according to

$$\vec{D} := \epsilon_0 \vec{E} + \vec{P}^r + \vec{P}^i = \vec{D}^r + \vec{P}^i(\vec{\rho}) \qquad \text{and} \qquad \boldsymbol{\varepsilon} := \boldsymbol{\varepsilon}^r + \boldsymbol{\varepsilon}^i(\boldsymbol{A}) \tag{18}$$

in *reversible* and *irreversible* parts as first suggested in Bassiouny et al. (1988) and Bassiouny and Maugin (1989). With the introduced dependency of the macroscopic irreversible parts in (18) on the internal state variables, the link is realized to the quantities motivated on the microscopic scale, cf. Fig. 2 c). With the introduction of these relationships, we follow the concept in Kamlah and Jiang (1999), Kamlah and Wang (2003a) and Mehling et al. (2007). The irreversible polarization vector

$$\vec{P}^i(\vec{\rho}) = P^{sat}\vec{\rho} \tag{19}$$

is expressed in a linear relationship to the microscopical relative polarization vector $\vec{\rho}$ weighted by the macroscopic *saturation polarization* $P^{sat}$ experimentally measurable for a polycrystal. In a similar fashion, the irreversible strain tensor

$$\boldsymbol{\varepsilon}^i(\boldsymbol{A}) := \frac{3}{2}\varepsilon^{sat}\boldsymbol{A}^{Dev} \qquad \text{with} \qquad \boldsymbol{A}^{Dev} = \underbrace{\left(\mathbb{I} - \frac{1}{3}\boldsymbol{I}\otimes\boldsymbol{I}\right)}_{\mathbb{P}^{Dev}} : \boldsymbol{A} \tag{20}$$

can be introduced in terms of the deviatoric part of the texture tensor $\boldsymbol{A}$ adapted to the macroscopic scale through the *saturation strain* $\varepsilon^{sat}$ corresponding to a fully oriented state. In (20) $\mathbb{I}_{ijkl} = (\delta_{ik}\delta_{jl} + \delta_{il}\delta_{jk})/2$ represents the symmetric fourth-order identity tensor and $\mathbb{P}^{Dev}$ the fourth-order deviatoric projection tensor. The dependence of the irreversible strain tensor on the deviatoric part of the texture tensor only is motivated by the experimentally observed volume preserving strain changes during a poling process (Lynch, 1996; Cao and Evans, 1993; Zhou et al., 2006a, 2010).

### 3.4. Definition of Helmholtz free energy

With the definitions from Section 3.3 at hand the Helmholtz free energy per unit volume initially introduced in Section 2.1 can be specified in the quadratic form

$$\psi(\boldsymbol{\varepsilon}, \vec{D}, \boldsymbol{A}, \vec{\rho}) = \frac{1}{2}(\boldsymbol{\varepsilon} - \boldsymbol{\varepsilon}^i) : \mathbb{C}^D : (\boldsymbol{\varepsilon} - \boldsymbol{\varepsilon}^i) - (\vec{D} - \vec{P}^i)\cdot\mathbb{h} : (\boldsymbol{\varepsilon} - \boldsymbol{\varepsilon}^i) + \frac{1}{2}(\vec{D} - \vec{P}^i)\cdot\boldsymbol{\beta}^{\varepsilon}\cdot(\vec{D} - \vec{P}^i) + \psi^i(\boldsymbol{A}, \vec{\rho}) \tag{21}$$

again with a split in a reversible and an irreversible part (Bassiouny et al., 1988; Cocks and McMeeking, 1999), the latter of which will be determined in detail in Section 3.6. The material tensors in (21) are the fourth-order *elasticity tensor at constant electric displacement*

$$\mathbb{C}^D(\vec{\rho}) = \mathbb{C}^E + \left(\mathbb{d}(\vec{\rho}) : \mathbb{C}^E\right)^T \cdot \mathbb{h}(\vec{\rho}), \tag{22}$$

the third-order *piezoelectric h-tensor*

$$\mathbb{h}(\vec{\rho}) = \boldsymbol{\beta}^{\varepsilon}(\vec{\rho})\cdot\mathbb{d}(\vec{\rho}) : \mathbb{C}^E \tag{23}$$

and the second-order *impermitivity tensor at constant strain*

$$\boldsymbol{\beta}^{\varepsilon}(\vec{\rho}) = \left(\boldsymbol{\epsilon}^{\sigma} - \mathbb{d}(\vec{\rho}) : \mathbb{C}^E : \mathbb{d}(\vec{\rho})^T\right)^{-1} \tag{24}$$

with an assumed intrinsic dependence on the polarization state of the material. This dependence comes from its definition in terms of the *piezoelectric d-tensor* (cf. e.g. Kamlah and Tsakmakis, 1999; Kamlah and Wang, 2003a)

$$d_{kij} = \left(d_{33} - d_{31} - d_{15}\right)\rho_k\rho_i\rho_j + d_{31}\rho_k\delta_{ij} + \frac{1}{2}d_{15}\left(\delta_{ki}\rho_j + \delta_{kj}\rho_i\right) \tag{25}$$

expressed as a function of the relative polarization vector $\vec{\rho}$. The material parameters $d_{33}$, $d_{31}$ and $d_{15}$ in (25) are the *longitudinal, transversal* and *shear piezoelectric constants*. The history dependence of the piezoelectric effect can be associated with the increasing anisotropy due to the progressive alignment of domains.

In contrast to that, to keep the model as simple as possible the isolated elastic and dielectric contributions in the definitions (22)–(24) are assumed to be isotropic and therefore independent of the evolution process of the internal state variables. First, representing the mechanical stiffness properties, the *elasticity tensor at constant electric field* is assumed as

$$\mathbb{C}^E = \lambda\,\boldsymbol{I}\otimes\boldsymbol{I} + 2\mu\mathbb{I}, \tag{26}$$

with the Lamé constants $\lambda = Y\nu/((1+\nu)(1-2\nu))$ and $\mu = Y/(2(1+\nu))$ in terms of the *Young's modulus* $Y$ and *Poisson's ratio* $\nu$. Second, the *permittivity tensor at constant stress*

$$\boldsymbol{\epsilon}^{\sigma} = (\epsilon_0 + \kappa^{\sigma})\boldsymbol{I} \tag{27}$$

describes the dielectric properties for an unpoled state. Here $\epsilon_0$ represents the *permittivity of the vacuum* and $\kappa^\sigma$ the *dielectric susceptibility* of the material under consideration. The relations of the different material tensors in the theory of piezoelectricity[4] can be found e.g. in Ikeda (1996). A history dependence of the material tensors (26) and (27) is definitely also possible e.g. in the framework of a invariant theory (cf. Schröder and Gross, 2004; Mehling et al., 2007). To maintain the ease of use of the model for engineering purposes we decide to use the more simple formulation introduced above.

The derivatives of the Helmholtz free energy in (21) and the material tensors (22)–(24) are documented in Appendices A and B.

### 3.5. Switching function

We restrict in this paper ourselves to rate-independent dissipative behavior, as frequently adopted in the modeling approach for ferroelectric materials. Thus, we assume that the microstructural switching processes take place independently of the velocity of the external loading. In well-established theories for rate-independent materials (e.g. plasticity of metals) it is commonly assumed that the initiation of the irreversible (and thus dissipative) effects is marked by a threshold value of the acting driving forces. The dissipative processes considered here are the domain switching effects represented by the previously introduced microscopically motivated internal state variables. The corresponding driving forces that dictate their evolution initially introduced in (3) as the work conjugate quantities can now be specified as

$$\mathbf{f}^A = -\partial_{\boldsymbol{A}}\psi \qquad \text{and} \qquad \vec{\mathrm{f}}^{\,\rho} = -\partial_{\vec{\rho}}\psi. \tag{28}$$

Their exact expression can be taken from Appendix A. As switching function, that indicates the load level at which domain switching processes occur in the material and thus an evolution of the microscopically motivated internal state variables is initiated, we choose the quadratic representation[5]

$$f := \frac{(\mathbf{f}^A)^{Dev} : (\mathbf{f}^A)^{Dev}}{(\mathrm{f}_c^A)^2} + \frac{\vec{\mathrm{f}}^{\,\rho} \cdot \vec{\mathrm{f}}^{\,\rho}}{(\mathrm{f}_c^\rho)^2} - 1 \leq 0 \tag{29}$$

already suggested in Kamlah and Wang (2003a). The critical values for the dissipative internal driving forces in the denominators can be identified as $\mathrm{f}_c^A = \sqrt{3/2}\varepsilon^{sat}\sigma^c$ and $\mathrm{f}_c^\rho = P^{sat}E^c$ (Kamlah and Wang, 2003a; Mehling et al., 2007), where $\sigma^c$ and $E^c$ represent the one-dimensional *coercive values* of mechanical stress and electric field. By considering the driving forces of the texture tensor in (29) in terms of deviatoric components, only trace-free incremental changes are induced for this internal state variable. Despite the formulations proposed in Huber and Fleck (2001), Landis (2002a) and Mehling et al. (2007), the switching function in (29) contains no coupling term. It is important to mention that such a term would destroy the symmetry of the material tangent (11) and therefore the variational structure of the local problem. A detailed discussion on the influence of the construction of the switching function on the symmetry of the material tangent can be found in Semenov et al. (2010). With the reduced version (29) some flexibility may get lost in order to fit the model to experimental results, but at this point, it is more important to us to preserve the variational structure of the model. The derivatives of the switching function in (29) can be found in Appendix C.

### 3.6. Hardening and saturation behavior

As discussed in Section 3.5, switching processes of domains are initiated if the electro-mechanical external loading intensity exceeds a critical threshold. At a certain point, an additional increase of load level is mandatory for further switching of domains due to their mutual blocking favored by pure volume preserving microstructural deformations. Such a hardening behavior which is also observed, for instance, in plasticity of metals, should be accounted for in the model. Another characteristic effect observed in ferroelectric materials is the saturation behavior if the reservoir of switchable domains is exhausted. The influence of this behavior should also be reflected in the states of the macroscopic strain and polarization by the model. For this purpose, the admissible range of the microscopically motivated internal state variables must be reasonably limited.

In order to capture the two mentioned effects, the irreversible part of the Helmholtz free energy density can be introduced as (cf. Kamlah and Jiang, 1999; Mehling et al., 2007)

$$\psi^i(\boldsymbol{A}, \vec{\rho}) := \frac{1}{2}c_A \boldsymbol{A}^{Dev} : \boldsymbol{A}^{Dev} + \frac{1}{2}c_\rho \vec{\rho} \cdot \vec{\rho} + \psi^{iA,sat}(\boldsymbol{A}) + \psi^{i\rho,sat}(\boldsymbol{A}, \vec{\rho}) \tag{30}$$

where the first two terms represent a linear kinematic hardening behavior in terms of the internal state variables. The scalar parameters $c_A$ and $c_\rho$ have to be chosen in a way to properly match the experimentally determined phenomenological hardening behavior of the material. With the last two terms in (30), the previously mentioned saturation behavior is to be incorporated into the model by introducing energy barriers. The exact definition of these energy barriers will be discussed in more detail below.

[4] The introduction of the material tensors (22)–(24) as a function of the tensors (25)–(27) may appear somewhat cumbersome at first glance. Indeed, the construction of the tensors (25)–(27) on the basis of material parameters that can be directly determined experimentally is the reason for this.

[5] Note here that a quadratic function has the advantage over a root function of continuous differentiability at the origin.

### 3.6.1. Strain saturation

For the identification of situations where saturation of the irreversible strain should occur, only the state of the c-axes and therefore the texture tensor has to be taken into account. At first, we want to focus on a situation where all c-axes are aligned in a certain direction, either driven by an electric field through 90° or 180° switching or induced by mechanical tensile stress by 90° switching, cf. Fig. 2 d) rightmost for such processes in $\vec{e}_1$-direction. Then the first eigenvector $\vec{e}_1^A$ of the texture tensor would coincide with this direction and the eigenvalues would have to be restricted to $\alpha_1 = 1$, $\alpha_2 = \alpha_3 = 0$ in this saturated state. Furthermore, a second situation is of interest where all c-axes are randomly switched by 90° in a plane perpendicular to a compressive stress direction, cf. Fig. 2 d) leftmost for such processes in $\vec{e}_3$-direction. The eigenvalues of the texture tensor should be bounded to $\alpha_1 = \alpha_2 = 1/2$, $\alpha_3 = 0$ in this case. A necessary condition for the fulfillment of these two saturation states is the non-negativity of the eigenvalues $\alpha_i \geq 0$. Thus, a suitable energy function should describe a barrier that increases towards infinity for $\alpha_i \to 0$ in order to limit the admissible range of the eigenvalues. Equivalent to Mehling et al. (2007), we choose the irreversible part of the free energy incorporating the saturation behavior for the evolution of the texture tensor to

$$\psi^{iA,sat}(\boldsymbol{A}) := \frac{a_A}{m_A} \sum_{i=1}^{3} \alpha_i^{-m_A} = \frac{a_A}{m_A} \mathrm{tr}(\boldsymbol{A}^{-m_A}) \tag{31}$$

where $a_A$ and $m_A$ are scalar parameters adjusting the steepness of the energy barrier. Note that due to a constant trace of the texture tensor (cf. Section 3.5) an upper limit enforced by an additional energy barrier for $\alpha_i \to 1$ is not necessary.

### 3.6.2. Polarization saturation

For the polarization saturation, the situation is slightly different. To identify the room for further increase of the relative polarization $\vec{\rho}$, the information of the alignment of the c-axes and therefore the texture tensor $\boldsymbol{A}$ has to be taken into account, too. Especially in cases where a large number of c-axes mechanically switched out of the electrical preferable poling direction the saturation value of polarization should be limited. To capture this information in a very compact way Mehling et al. (2007) and Landis (2002a) motivated the introduction of a distance variable $\eta(\boldsymbol{A}, \vec{\rho})$. In this paper, we propose a modified quadratic representation of the distance variable in Mehling et al. (2007) as

$$\eta(\boldsymbol{A}, \vec{\rho}) := \|(\xi \boldsymbol{I} + (1-\xi)\boldsymbol{A})^{-1} \cdot \vec{\rho}\|^2 \tag{32}$$

with a newly introduced additional parameter $0 \leq \xi \leq 1$. The advantage of the quadratic form in (32) over those proposed in Mehling et al. (2007) is the continuous differentiability. The parameter $\xi$ in (32) controls the amount of polarization reachable in direction $\vec{e}_3^A$ of the smallest eigenvalue $\alpha_3$. As will be shown below, this modification compensates for the lost flexibility due to the simplified switching function (29) compared to that used in Mehling et al. (2007) in order to preserve the variational structure of the model. More details on the construction of the distance variable can be found in Mehling et al. (2007) and Mehling (2007).

The contribution to the energy function (30) enforcing an upper limit for the distance variable $\eta \to 1$ can be introduced as

$$\psi^{i\rho,sat}(\boldsymbol{A}, \vec{\rho}) := \frac{a_\rho}{m_\rho}(1-\eta)^{-m_\rho} \tag{33}$$

with the two parameters $a_\rho$ and $m_\rho$ which have to be adapted to the measured material behavior.

In Fig. 3, top left, the admissible region enforced by the energy barrier contributions in (31) and (33) is shown for a simplified one-dimensional representation of the internal state variables. The influence on the shape of this region by the parameter $\xi$ in (32) is illustrated here by the choice of different values. With a calculated solution path for an initial poling and a following depolarization process for $\xi = 0.2$, the effect of the energy barriers on the evolution process of the internal variables is demonstrated. The resulting characteristic macroscopic material behavior is demonstrated by the partial dielectric, butterfly and ferroelastic hysteresis as well as the mechanical depolarization response for different values of $\xi$ on the right of Fig. 3.

## 4. Numerical treatment of the local incremental variational problem

In this section, a numerical procedure for an incremental solution of the material model introduced in Section 3 is presented. For this purpose, the model is embedded into the variational structure of the local incremental constitutive problem presented in Section 2 in order to obtain an efficient solution scheme in between a time step[6] $\Delta t = t_{n+1} - t_n$. In this section, algorithms are presented which are adapted to non-linear finite element schemes, providing a solution of the used material model in each global iteration step at each Gauss point. Furthermore, a Helmholtz free energy based framework is assumed in which a finite element solution step delivers the current state of the strain $\boldsymbol{\varepsilon}$ and the electric displacement $\boldsymbol{D}$, frozen within one iteration step of a global solution procedure. A converged solution state of the internal variables $\boldsymbol{q}_n$ related to the previous global time step $t_n$, read from the memory, completes the set of input parameters provided for every material point. All quantities occurring in this section are represented in vector-matrix notation. More precisely, e.g. the microscopically motivated internal state variables introduced in Section 3 and their corresponding internal driving forces are expressed in the form

$$\boldsymbol{q} = \left[A_{11}, A_{22}, A_{33}, 2A_{12}, 2A_{23}, 2A_{13}, \rho_1, \rho_2, \rho_3\right]^T \quad \text{and} \quad \mathbf{f}^q = \left[\mathrm{f}_{11}^A, \mathrm{f}_{22}^A, \mathrm{f}_{33}^A, \mathrm{f}_{12}^A, \mathrm{f}_{23}^A, \mathrm{f}_{13}^A, \mathrm{f}_1^\rho, \mathrm{f}_2^\rho, \mathrm{f}_3^\rho\right]^T. \tag{34}$$

[6] Note that the time introduced in Section 2 related to the rate of the internal variables in the context of a rate-independent constitutive model has no physical meaning on the global finite element level when furthermore neglecting conductivity and inertia effects. The phrase 'time step' should be interpreted more as a load step in this context.

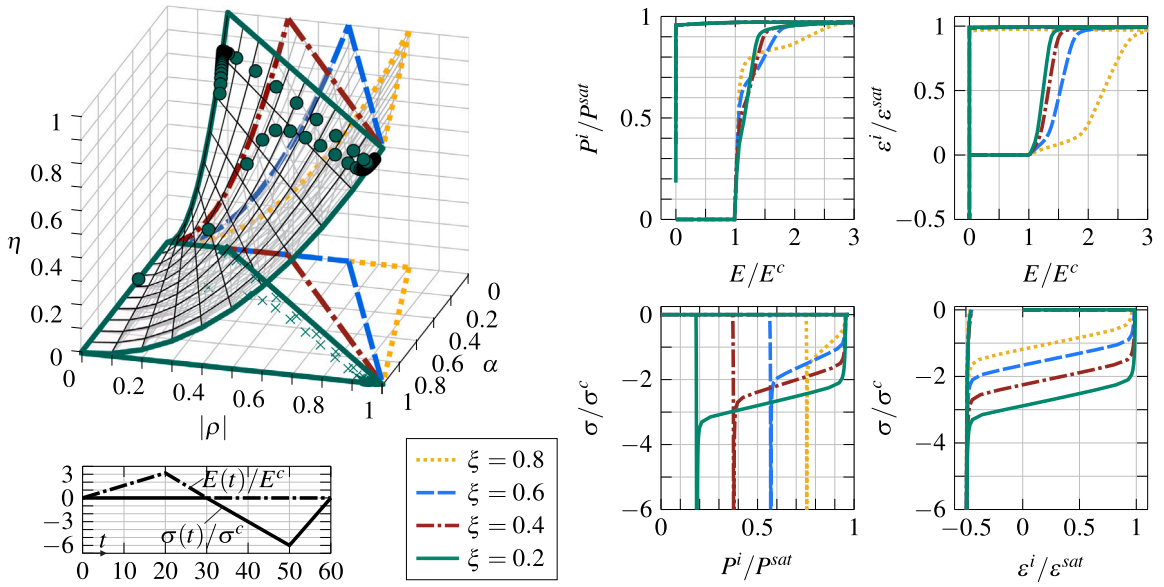


**Fig. 3.** Influence of the parameter $\xi$ on the range of admissible values for a simplified one-dimensional representation of the microscopically motivated internal state variables, cf. detailed discussion in Kamlah and Wang (2003b). The saturation behavior of the macroscopic irreversible polarization/strain for a initial poling and a subsequent depolarization process for different values of $\xi$ is illustrated (in the figure top left, the dots indicate the calculated path for an initial poling and the following depolarization process for $\xi = 0.2$, the crosses are their projections on the $\alpha - \rho$-plane).

### 4.1. Specification of the dissipation potential

In the rate-type potential (4), we postulated the existence of a dissipation potential completely representing the power spent on domain switching effects in a material unit volume. Now we want to focus on a suitable construction of this function fitting to the ferroelectric material model presented in Section 3. In case of rate-independent dissipative material behavior, a suitable algorithmic representation of the dissipation potential can be given by (cf. Miehe et al., 2011)

$$\phi\big(\tfrac{1}{\Delta t}(\boldsymbol{q}-\boldsymbol{q}_n)\big) = \sup_{\mathbf{f}^q,\lambda\geq 0}\Big\{\mathbf{f}^{q\,T}\tfrac{1}{\Delta t}(\boldsymbol{q}-\boldsymbol{q}_n) - \lambda f(\mathbf{f}^q)\Big\}\,. \tag{35}$$

Remarkably, this function appears as a separate maximization problem that has to be optimized simultaneously during the solution process of the local problem. The motivation for this, in case of the first term in (35), is rooted in the *principle of maximum dissipation*, well-established in the theory of classical plasticity, see e.g. Hill (1950) and Lubliner (1984). From this postulate, the physically most sensible state is found if the work done by the internal driving forces $\mathbf{f}^q$ on the evolution of the internal state variables $\boldsymbol{q}$ is maximized. The second term in the optimization problem in (35) is related to the enforcement of the switching function (29) in the sense that has to stay non-positive for arbitrary loading processes. Utilizing the Lagrange multiplier method, this inequality constraint is incorporate into the dissipation potential. The driving forces $\mathbf{f}^q$ in (35) appear as newly introduced independent variables which are to be optimized with regard to the fulfillment of the two discussed requirements namely: maximized dissipation and non-violated switching function.

As pointed out in Section 2.2 the solution process can be performed in two steps. First, solving the variational problem (6) gives a new state of the internal variables $\boldsymbol{q}$, and second, evaluating the constitutive Eqs. (10) delivers an update for the stress $\boldsymbol{\sigma}$ and the electric field $\boldsymbol{E}$. Additionally, the local incremental update has to provide the current state of the algorithmic material tangent $\boldsymbol{C}_T$ (cf. (11)) correlated to the material point under consideration in order to perform the next iteration step of the global problem (76).

### 4.2. Incremental variational update of the internal state variables

In order to obtain a realization of a numerical solution process for the internal state variables at time $t_{n+1}$ representative for a material point, the optimization problem (6) is written as

$$\boldsymbol{q} = \mathrm{Arg}\Big\{\inf_{\boldsymbol{q}}\sup_{\mathbf{f}^q,\gamma}\pi^{int}(\boldsymbol{\varepsilon},\boldsymbol{D},\boldsymbol{q},\mathbf{f}^q,\gamma)\Big\} = \mathrm{Arg}\Big\{\inf_{\boldsymbol{q}}\Big\{\psi(\boldsymbol{\varepsilon},\boldsymbol{D},\boldsymbol{q}) - \psi_n(\boldsymbol{\varepsilon}_n,\boldsymbol{D}_n,\boldsymbol{q}_n) + \sup_{\mathbf{f}^q,\gamma}\big\{\mathbf{f}^{q\,T}(\boldsymbol{q}-\boldsymbol{q}_n) - \gamma f(\mathbf{f}^q)\big\}\Big\}\Big\} \tag{36}$$

by incorporation of the dissipation potential (35). For the Lagrange multiplier, the algorithmic form $\gamma = \lambda\Delta t$ is chosen in (36).

A solution for the optimization problem in (36) is to be determined with the help of a return mapping algorithm extensively used in the field of elasto-plasticity (Wilkins, 1964; Ortiz and Simo, 1986). In this solution scheme, an initial reversible predictor step is performed assuming constant internal state variables within $\Delta t$ in order to check whether the switching function is violated

($f > 0$), and if an evolution of the internal state variables ($\Delta \boldsymbol{q} = \boldsymbol{q} - \boldsymbol{q}_n \neq \boldsymbol{0}$) is required (cf. Section 3.5). For this purpose, a trial state of the switching function $f^{tr}$ has to be assumed with so-called 'best guess'-values for the at this point unknown internal driving forces $\mathbf{f}^q$. A meaningful trial state of the switching function can be assumed as

$$f^{tr} := f(\mathbf{f}^{q,tr}) \qquad \text{with} \qquad \mathbf{f}^{q,tr} = -\partial_{\boldsymbol{q}} \psi(\boldsymbol{\varepsilon}, \boldsymbol{D}, \boldsymbol{q}_n) \tag{37}$$

while estimating the internal driving forces $\mathbf{f}^q$ by expecting validity of the relation in (28) evaluated for the given frozen state of the strain $\boldsymbol{\varepsilon}$, electric displacement $\boldsymbol{D}$ and the state of the internal variables at the end of the previous time step $\boldsymbol{q}_n$.

If the trial state does not violate the switching function ($f^{tr} \leq 0$), the assumption of complete reversible material behavior for the current time step was correct and the solution process of the problem (36) ends with no change in the internal variables. Otherwise, if the trial state exceeds the critical value of the switching function ($f^{tr} > 0$), an updated state of the internal variables at time $t_{n+1}$ is found by solving the optimization problem (36). A solution for the internal state variables $\boldsymbol{q}$ has to satisfy the stationarity condition of (36). Additionally to the incremental form of the Biot equation (7) (cf. Section 2.2), two further sets of equations corresponding to the stationarity of the maximum-type problem in (36) have to be fulfilled. Summarizing these conditions by calculating the Jacobian of the variational problem in (36) with the help of the abbreviation $\boldsymbol{a} = [\boldsymbol{q}^T, \mathbf{f}^{qT}, \gamma]^T$ leads to

$$\partial_{\boldsymbol{a}} \pi^{int} = \begin{bmatrix} \partial_{\boldsymbol{q}} \pi^{int} \\ \partial_{\mathbf{f}^q} \pi^{int} \\ \partial_{\gamma} \pi^{int} \end{bmatrix} = \begin{bmatrix} \partial_{\boldsymbol{A}} \psi + \mathbf{f}^A \\ \partial_{\boldsymbol{\rho}} \psi + \mathbf{f}^{\rho} \\ \boldsymbol{A} - \boldsymbol{A}_n - \gamma (\partial_{\mathbf{f}^A} f)^T \\ \boldsymbol{\rho} - \boldsymbol{\rho}_n - \gamma (\partial_{\mathbf{f}^{\rho}} f)^T \\ -f \end{bmatrix}_{19\times 1} =: \boldsymbol{R} = \boldsymbol{0}, \tag{38}$$

along with the algorithmic version of loading and unloading conditions

$$\gamma \geq 0, \quad f \leq 0, \quad \gamma f = 0. \tag{39}$$

The additional stationarity conditions $(38)_{3-5}$, arising from the special form of the dissipation potential in (35), can be identified as the 'flow' rules for the internal state variables and the negative switching function. Due to the non-linearity of the system of equations in (38), a solution must be found iteratively using Newton's method. For this purpose, we define (38) as the residual vector $\boldsymbol{R}$ of the solution scheme. An incremental update in the Newton-type iteration is given by a Taylor series expansion of (38) as

$$\Delta \boldsymbol{a} = -(\partial_{\boldsymbol{a}} \boldsymbol{R})^{-1} \boldsymbol{R}, \tag{40}$$

where the tangent matrix in (40) can be identified as the Hessian of the variational problem in (36) given by

$$\partial_{\boldsymbol{a}} \boldsymbol{R} := \partial^2_{\boldsymbol{a}\boldsymbol{a}} \pi^{int} = \begin{bmatrix} \partial^2_{\boldsymbol{q}\boldsymbol{q}} \pi^{int} & \partial^2_{\mathbf{f}^q \boldsymbol{q}} \pi^{int} & \partial^2_{\boldsymbol{q}\gamma} \pi^{int} \\ \partial^2_{\mathbf{f}^q \boldsymbol{q}} \pi^{int} & \partial^2_{\mathbf{f}^q \mathbf{f}^q} \pi^{int} & \partial^2_{\mathbf{f}^q \gamma} \pi^{int} \\ \partial^2_{\gamma \boldsymbol{q}} \pi^{int} & \partial^2_{\gamma \mathbf{f}^q} \pi^{int} & \partial^2_{\gamma\gamma} \pi^{int} \end{bmatrix} = \begin{bmatrix} \partial^2_{\boldsymbol{A}\boldsymbol{A}} \psi & \partial^2_{\boldsymbol{A}\boldsymbol{\rho}} \psi & \mathbf{1}_{6\times 6} & \mathbf{0}_{6\times 3} & \mathbf{0}_{6\times 1} \\ \partial^2_{\boldsymbol{\rho}\boldsymbol{A}} \psi & \partial^2_{\boldsymbol{\rho}\boldsymbol{\rho}} \psi & \mathbf{0}_{3\times 6} & \boldsymbol{I}_{3\times 3} & \mathbf{0}_{3\times 1} \\ \mathbf{1}_{6\times 6} & \mathbf{0}_{6\times 3} & -\gamma\, \partial^2_{\mathbf{f}^A \mathbf{f}^A} f & \mathbf{0}_{6\times 3} & -(\partial_{\mathbf{f}^A} f)^T \\ \mathbf{0}_{3\times 6} & \boldsymbol{I}_{3\times 3} & \mathbf{0}_{3\times 6} & -\gamma\, \partial^2_{\mathbf{f}^{\rho} \mathbf{f}^{\rho}} f & -(\partial_{\mathbf{f}^{\rho}} f)^T \\ \mathbf{0}_{1\times 6} & \mathbf{0}_{1\times 3} & -\partial_{\mathbf{f}^A} f & -\partial_{\mathbf{f}^{\rho}} f & 0 \end{bmatrix}_{19\times 19} \tag{41}$$

with $\mathbf{1}_{6\times 6} = \mathrm{diag}[1\,1\,1\,1\,1\,1]$. Note here due to the variational structure of the optimization problem (36) the tangent matrix (41) becomes symmetric, but unfortunately not positive definite for the case under consideration. This circumstance is a property of the Lagrange multiplier method, used for the enforcement of the switching condition in (36), which leads to a saddle point problem[7]. The iteration with incremental updates (40) can be terminated if the norm of the residual vector in (38) vanishes in the numerical sense i.e. $\|\boldsymbol{R}\| = \|\partial_{\boldsymbol{a}} \pi^{int}\| \leq \mathrm{tol}$.

Due to the fact that the energy barrier functions used to limit the internal state variables in (31) and (33) assume finite values even outside the admissible range, these barriers can be penetrated for sufficiently large time steps during the local iteration (40). In most cases, this leads to the divergence of the solution procedure. To remedy this problem, a numerical damping method can be used, in which the current solution increment in (40) is reduced by a damping factor $\beta \in (0, 1)$. The required damping factor is determined by continuously reducing until the solution state is again sufficiently within the admissible range.

[7] Alternatively, the switching condition can also be enforced with a penalty method to circumvent this problem. Such a formulation would lead to a rate-dependent formulation whose solution for a penalty factor approaching infinity would approximate the rate-independent solution, see e.g. Miehe et al. (2011). A comparison of both methods is done e.g. in Fassin et al. (2018). Since the authors did not observe any major convergence problems with the chosen formulation, this modification was not considered necessary.

### 4.3. Incremental variational constitutive update

With a converged solution $\boldsymbol{a}^*$ of the optimization problem (36) at hand, in line with (8), the reduced incremental internal work potential can be written as

$$W(\boldsymbol{\varepsilon}, \boldsymbol{D}) = \pi^{int}(\boldsymbol{\varepsilon}, \boldsymbol{D}, \boldsymbol{a})\Big|_{\boldsymbol{a}=\boldsymbol{a}^*}, \tag{42}$$

evaluated for the current state of the material. In order to compute the constitutive equations in (10), the derivatives of the reduced incremental work potential in (42) have to be obtained. For this purpose, the implicit dependency of the solution vector $\boldsymbol{a}$ must be taken into account. Using the abbreviation $\boldsymbol{e} = [\boldsymbol{\varepsilon}^T, \boldsymbol{D}^T]^T$, the first derivative of the reduced incremental work potential is calculated as

$$\partial_{\boldsymbol{e}} W = \Big[\partial_{\boldsymbol{e}}\pi^{int} + \underbrace{\partial_{\boldsymbol{a}}\pi^{int}}_{=\boldsymbol{R}=0}\,\partial_{\boldsymbol{e}}\boldsymbol{a}\Big]\Big|_{\boldsymbol{a}=\boldsymbol{a}^*} = \partial_{\boldsymbol{e}}\pi^{int}\Big|_{\boldsymbol{a}=\boldsymbol{a}^*} \tag{43}$$

while in the second term of (43) the stationarity conditions (38) can be identified which vanish for the found optimal solution $\boldsymbol{a}^*$. Finally, the constitutive relations (10) for the dependent quantities mechanical stress and electric field at the current time $t_{n+1}$ evaluated for the determined state $\boldsymbol{a}^*$ are given by

$$\begin{aligned}
&\boldsymbol{\sigma} = \partial_{\boldsymbol{\varepsilon}} W = \partial_{\boldsymbol{\varepsilon}}\pi^{int}|_{\boldsymbol{a}=\boldsymbol{a}^*} = \partial_{\boldsymbol{\varepsilon}}\psi|_{\boldsymbol{a}=\boldsymbol{a}^*} = \boldsymbol{C}^D_{6\times6}(\boldsymbol{\rho}^*)\big(\boldsymbol{\varepsilon} - \boldsymbol{\varepsilon}^i(\boldsymbol{A}^*)\big) - \boldsymbol{h}^T_{3\times6}(\boldsymbol{\rho}^*)\big(\boldsymbol{D} - \boldsymbol{P}^i(\boldsymbol{\rho}^*)\big) \qquad \text{and}\\
&\boldsymbol{E} = \partial_{\boldsymbol{D}} W = \partial_{\boldsymbol{D}}\pi^{int}|_{\boldsymbol{a}=\boldsymbol{a}^*} = \partial_{\boldsymbol{D}}\psi|_{\boldsymbol{a}=\boldsymbol{a}^*} = -\boldsymbol{h}_{3\times6}(\boldsymbol{\rho}^*)\big(\boldsymbol{\varepsilon} - \boldsymbol{\varepsilon}^i(\boldsymbol{A}^*)\big) + \boldsymbol{\beta}^{\varepsilon}(\boldsymbol{\rho}^*)\big(\boldsymbol{D} - \boldsymbol{P}^i(\boldsymbol{\rho}^*)\big),
\end{aligned} \tag{44}$$

where $\boldsymbol{C}^D_{6\times6}$ and $\boldsymbol{h}_{3\times6}$ are the vector-matrix representations of the tensors (22) and (23).

### 4.4. Algorithmic consistent tangent moduli

Another information that has to be provided by the material model is the algorithmic material tangent. It is derived by the second derivative of the reduced incremental internal work potential $W(\boldsymbol{\varepsilon}, \boldsymbol{D})$ with respect to its argument, see (11). With the first derivative (43) at hand and using $\partial_{\boldsymbol{a}}\pi^{int}|_{\boldsymbol{a}=\boldsymbol{a}^*} = 0$, the second derivative is given by

$$\partial^2_{\boldsymbol{ee}} W = \Big[\partial^2_{\boldsymbol{ee}}\pi^{int} + \partial^2_{\boldsymbol{ea}}\pi^{int}\,\partial_{\boldsymbol{e}}\boldsymbol{a}\Big]\Big|_{\boldsymbol{a}=\boldsymbol{a}^*} \tag{45}$$

while the sensitivity $\partial_{\boldsymbol{e}}\boldsymbol{a}|_{\boldsymbol{a}=\boldsymbol{a}^*}$ in (45) can be written with the implicit function theorem (de Oliveira, 2014) as

$$\partial_{\boldsymbol{e}}\boldsymbol{a} = -\Big[(\partial^2_{\boldsymbol{aa}}\pi^{int})^{-1}\partial^2_{\boldsymbol{ae}}\pi^{int}\Big]\Big|_{\boldsymbol{a}=\boldsymbol{a}^*}. \tag{46}$$

This results in the material tangent being

$$\boldsymbol{C}_T := \partial^2_{\boldsymbol{ee}} W = \Big[\partial^2_{\boldsymbol{ee}}\pi^{int} - \partial^2_{\boldsymbol{ea}}\pi^{int}(\partial^2_{\boldsymbol{aa}}\pi^{int})^{-1}\partial^2_{\boldsymbol{ae}}\pi^{int}\Big]\Big|_{\boldsymbol{a}=\boldsymbol{a}^*} \tag{47}$$

or more detailed written as

$$\boldsymbol{C}_T = \begin{bmatrix} \partial^2_{\boldsymbol{\varepsilon\varepsilon}} W & \partial^2_{\boldsymbol{\varepsilon D}} W \\ \partial^2_{\boldsymbol{D\varepsilon}} W & \partial^2_{\boldsymbol{DD}} W \end{bmatrix} = \begin{bmatrix} \partial^2_{\boldsymbol{\varepsilon\varepsilon}}\psi & \partial^2_{\boldsymbol{\varepsilon D}}\psi \\ \partial^2_{\boldsymbol{D\varepsilon}}\psi & \partial^2_{\boldsymbol{DD}}\psi \end{bmatrix} - \begin{bmatrix} \partial^2_{\boldsymbol{\varepsilon q}}\psi & \boldsymbol{0}_{6\times10} \\ \partial^2_{\boldsymbol{Dq}}\psi & \boldsymbol{0}_{3\times10} \end{bmatrix} (\partial_{\boldsymbol{a}}\boldsymbol{R})^{-1} \begin{bmatrix} \partial^2_{\boldsymbol{q\varepsilon}}\psi & \partial^2_{\boldsymbol{qD}}\psi \\ \boldsymbol{0}_{10\times6} & \boldsymbol{0}_{10\times3} \end{bmatrix}, \tag{48}$$

evaluated at the frozen states of $\boldsymbol{\varepsilon}$ and $\boldsymbol{D}$ – and the found optimal solution $\boldsymbol{a}^*$ of (36). The required derivatives of the Helmholtz free energy in (48) can be found in Appendix A. Note here that the second term in (48) is only active if the switching function (37) is initially violated and evolution of the internal variables $\boldsymbol{q}$ takes place. It describes, compared to a pure reversible response, the softening behavior due to the evolution of the internal variables.

The very straightforward derivation of the algorithmic material tangent (47) in analytic form represents another advantage that occurs when using the framework of generalized standard materials. It should be noted, that only for a consistent derivation of the algorithmic material tangent by considering all the equations describing the dissipative material behavior, a quadratic convergence behavior during a global finite element iteration is ensured (Simo and Taylor, 1985; Gruttmann and Stein, 1988).

## 5. Variational formulation of the global electro-mechanical boundary value problem and mixed FEM

In this section, variational formulation of the boundary value problem for an electro-mechanical body $\mathcal{B} \subset \mathcal{R}^3$ are in focus. To establish a connection to the theory initially introduced in Section 2, it is assumed that such a body on the global macroscopical level consists of a set of material points of the type considered there. Special attention is paid to a formulation in a Helmholtz free energy based framework in order to benefit from its positive mathematical properties, e.g. the positive definite and symmetric material tangent modulus (cf. Section 2.2). Consequently, a suitable variational principle should be formulated in terms of the reduced incremental work potential per unit volume $W(\boldsymbol{\varepsilon}, \vec{D})$ derived in (8) and additionally contain all relevant balance equations of an electro-mechanical continuum in an integral sense. Having a functional with variational structure at hand, by taking into account the entire volume of $\mathcal{B}$ the basis for a finite element solution of the optimization problem (9) is created. Additionally, possible functional spaces of the different variables should be discussed. An overview of possible variational formulations for electro-mechanical problems is given in Vogel et al. (2012).

### 5.1. Boundary value problem for coupled electro-mechanical problems

In the following the basic equations of an electro-mechanical body $\mathcal{B}$ under consideration are summarized. Assuming a theory of small deformations, the infinitesimal strain tensor is given by

$$\boldsymbol{\varepsilon} := \nabla^s \vec{u} = \frac{1}{2}(\nabla \otimes \vec{u} + \vec{u} \otimes \nabla) \qquad \text{in} \quad \mathcal{B}, \tag{49}$$

describing a connection to the displacement vector $\vec{u}$. Furthermore, every stress state $\boldsymbol{\sigma}$ in the body has to fulfill

$$\nabla \cdot \boldsymbol{\sigma} + \vec{b}_0 = \vec{0} \qquad \text{with} \qquad \boldsymbol{\sigma} = \boldsymbol{\sigma}^T \qquad \text{in} \quad \mathcal{B}, \tag{50}$$

following from the balance of linear and angular momentum under the action of the body forces $\vec{b}_0$.

Neglecting all magnetic effects and assuming the material contains no free body charges, the Maxwell equations reduce to the form

$$\nabla \cdot \vec{D} = 0 \qquad \text{and} \qquad \nabla \times \vec{E} = \vec{0} \iff \vec{E} = -\nabla\varphi \qquad \text{in} \quad \mathcal{B} \tag{51}$$

of the Gauss' law and Faraday's law in order to describe the balances of the electric displacement $\vec{D}$ and electric field $\vec{E}$. The requirement of a curl-free electric field in $(51)_2$ is directly satisfied by its expression as the negative gradient of an electric scalar potential $\varphi$.

The mechanical boundary conditions can be introduced by a decomposition of the boundary of the body under consideration in $\partial\mathcal{B} := \partial\mathcal{B}_u \cup \partial\mathcal{B}_t$ as

$$\vec{u} = \vec{u}_0 \qquad \text{on} \quad \partial\mathcal{B}_u \qquad \text{and} \qquad \boldsymbol{\sigma} \cdot \vec{n} = \vec{t}_0 \qquad \text{on} \quad \partial\mathcal{B}_t, \tag{52}$$

while on $\partial\mathcal{B}_u$ a prescribed displacement vector $\vec{u}_0$ represents the Dirichlet boundary conditions and on $\partial\mathcal{B}_t$ a traction vector $\vec{t}_0$ acting as Neumann boundary conditions. In the same fashion, by decomposing $\partial\mathcal{B} := \partial\mathcal{B}_\varphi \cup \partial\mathcal{B}_\omega$, the electric boundary conditions can be defined as

$$\varphi = \varphi_0 \qquad \text{on} \quad \partial\mathcal{B}_\varphi \qquad \text{and} \qquad \vec{D} \cdot \vec{n} = -\omega_0 \qquad \text{on} \quad \partial\mathcal{B}_\omega, \tag{53}$$

where the Dirichlet boundary conditions are expressed by a predefined electric potential $\varphi_0$ and the Neumann boundary conditions are described by a given surface charge $\omega_0$.

### 5.2. Five-field electro-mechanical variational principle

A variational potential formulated in a Helmholtz free energy based framework for electro-mechanical problems can be written in the form

$$\Pi(\boldsymbol{\varepsilon}, \vec{D}, \boldsymbol{\sigma}, \vec{u}, \varphi) = \int_{\mathcal{B}} \left( W(\boldsymbol{\varepsilon}, \vec{D}) + \nabla\varphi \cdot \vec{D} + \boldsymbol{\sigma} : (\nabla^s \vec{u} - \boldsymbol{\varepsilon}) \right) dV - \int_{\mathcal{B}} \vec{b}_0 \cdot \vec{u} \, dV - \int_{\partial\mathcal{B}_t} \vec{t}_0 \cdot \vec{u} \, dA + \int_{\partial\mathcal{B}_\omega} \omega_0 \varphi \, dA \tag{54}$$

with, in summary, five independent field quantities. This formulation, based on that in Ghandi and Hagood (1997) (cf. discussion in 1.1.4), was initially introduced in the framework of large strain electro-mechanics in Gil and Ortigosa (2016), Ortigosa and Gil (2016) and Franke et al. (2019). In the current paper, it is used for the first time for modeling dissipative processes while restricting it to a small strain regime. In the potential (54), the electric Gibbs energy is replaced by the partial Legendre transformation $G_2(\boldsymbol{\varepsilon}, \vec{E}) = \psi(\boldsymbol{\varepsilon}, \vec{D}) - \vec{E} \cdot \vec{D}$ in order to create a representation dependent on the Helmholtz free energy. Whereby the reduced incremental work potential per unit volume in (8) is used here instead. Furthermore, in (54) the electric field is directly written as the negative gradient of its scalar potential, cf. (51). To increase accuracy and the computational stability, the variational potential (54) is extended by an additional constraint affecting the mechanical field quantities only. In doing so, the kinematic relation (49) is imposed in a variational sense by a Lagrange multiplier approach. This Lagrange multiplier can be identified as the mechanical stress tensor $\boldsymbol{\sigma}$. Variational principles for purely mechanical problems including this additional constraint are commonly called Hu–Washizu formulations (Hu, 1955; Washizu, 1955).

A five-field saddle-point variational principle in terms of the system potential (54) is given by

$$\{\boldsymbol{\varepsilon}, \vec{D}, \boldsymbol{\sigma}, \vec{u}, \varphi\} = \operatorname{Arg}\left\{ \inf_{\boldsymbol{\varepsilon} \in L^2} \inf_{\vec{D} \in L^2} \sup_{\boldsymbol{\sigma} \in L^2} \inf_{\vec{u} \in \mathcal{W}_u} \sup_{\varphi \in \mathcal{W}_\varphi} \Pi(\boldsymbol{\varepsilon}, \vec{D}, \boldsymbol{\sigma}, \vec{u}, \varphi) \right\} \tag{55}$$

in order to determine the unknown quantities, while $L^2$ indicates the Lebesgue space of square-integrable functions. The admissible functional spaces for the displacement field and the electric potential satisfying the corresponding boundary conditions are given by

$$\mathcal{W}_u := \left\{ \vec{u} \in H^1(\mathcal{B}) \mid \vec{u} = \vec{u}_0 \text{ on } \partial\mathcal{B}_u \right\} \qquad \text{and} \qquad \mathcal{W}_\varphi := \left\{ \varphi \in H^1(\mathcal{B}) \mid \varphi = \varphi_0 \text{ on } \partial\mathcal{B}_\varphi \right\}, \tag{56}$$

where $H^1$ denotes the Sobolev functional space of square-integrable functions whose square-integrable derivatives exist. Note that despite the formulation in terms of Helmholtz free energy by using a partial Legendre transformation, the variational principle in (55) preserves a saddle-point structure due to its foundation on the electric Gibbs energy. But in addition to the beneficial convex properties of a positive definite material tangent, the electric scalar potential is included as a degree of freedom in this functional.

This gives the possibility to define suitable electric boundary conditions for real-world problems in engineering applications, e.g. poling processes of piezoceramic devices with complex electrode layouts. Taking these aspects into account, from the authors' point of view, a finite element formulation based on variational potential (54) represents a good compromise between computational stability and applicability to practical problems.

In order to evaluate the stationarity conditions of the five-field principle in (55), the first variation of the potential (54) is determined as

$$\delta\Pi = \int_{\mathcal{B}} \left( (\partial_{\boldsymbol{\varepsilon}} W - \boldsymbol{\sigma}) : \delta\boldsymbol{\varepsilon} + (\partial_{\vec{D}} W + \nabla\varphi) \cdot \delta\vec{D} + (\nabla^s \vec{u} - \boldsymbol{\varepsilon}) : \delta\boldsymbol{\sigma} + \boldsymbol{\sigma} : \nabla^s \delta\vec{u} + \vec{D} \cdot \nabla\delta\varphi \right) dV + \delta\Pi^{ext} = 0$$
$$\text{with} \qquad \delta\Pi^{ext} = -\int_{\mathcal{B}} \vec{b}_0 \cdot \delta\vec{u}\, dV - \int_{\partial\mathcal{B}_t} \vec{t}_0 \cdot \delta\vec{u}\, dA + \int_{\partial\mathcal{B}_\omega} \omega_0 \delta\varphi\, dA. \tag{57}$$

From Eq. (57), by making use of Gauss' divergence theorem the following Euler equations of the variational principle (55) can be identified:

| | | | |
|---|---|---|---|
| *Constitutive relation* | $\partial_{\boldsymbol{\varepsilon}} W - \boldsymbol{\sigma} = \mathbf{0}$ | in $\mathcal{B}$ | (58a) |
| *Faraday's law* | $\partial_{\vec{D}} W + \nabla\varphi = \vec{0}$ | in $\mathcal{B}$ | (58b) |
| *Kinematic relation* | $\nabla^s \vec{u} - \boldsymbol{\varepsilon} = \mathbf{0}$ | in $\mathcal{B}$ | (58c) |
| *Balance of linear momentum* | $\nabla \cdot \boldsymbol{\sigma} + \vec{b}_0 = \vec{0}$ | in $\mathcal{B}$ | (58d) |
| *Gauss' law* | $\nabla \cdot \vec{D} = 0$ | in $\mathcal{B}$ | (58e) |
| *Stress traction* | $\boldsymbol{\sigma} \cdot \vec{n} - \vec{t}_0 = \vec{0}$ | on $\partial\mathcal{B}_t$ | (58f) |
| *Surface charges* | $\vec{D} \cdot \vec{n} + \omega_0 = 0$ | on $\partial\mathcal{B}_\omega$. | (58g) |

It can be stated that a solution of the variational principle (55) fulfills all the equations describing an electro-mechanical boundary value problem (see Section 5.1) and additionally the initially derived constitutive relation of the stress in $(10)_1$ in a weak (variational) sense. This is why the variation of the system potential in (57) is commonly called the weak form of the problem.

Due to the assumed non-linearity of the optimization problem in (55), a solution has to be performed iteratively, e.g. with Newton's method. Therefore a linearization of the stationarity condition (57) is necessary. Such a linearization can be written by the Taylor series expansion in general: $\mathrm{Lin}\,[\delta\Pi(x)] = \delta\Pi(x) + D_x[\delta\Pi(x)] \cdot \Delta x = \delta\Pi + \Delta\delta\Pi$, see e.g. Wriggers (2008). The tangent part of the linearization under the assumption of conservative external loadings is derived as

$$\Delta\delta\Pi = \int_{\mathcal{B}} \Big( \delta\boldsymbol{\varepsilon} : \left(\partial^2_{\boldsymbol{\varepsilon}\boldsymbol{\varepsilon}} W : \Delta\boldsymbol{\varepsilon} + \partial^2_{\boldsymbol{\varepsilon}\vec{D}} W \cdot \Delta\vec{D} - \Delta\boldsymbol{\sigma}\right) + \delta\vec{D} \cdot \left(\partial^2_{\vec{D}\boldsymbol{\varepsilon}} W : \Delta\boldsymbol{\varepsilon} + \partial^2_{\vec{D}\vec{D}} W \cdot \Delta\vec{D} + \nabla\Delta\varphi\right)$$
$$+ \delta\boldsymbol{\sigma} : \left(\nabla^s \Delta\vec{u} - \Delta\boldsymbol{\varepsilon}\right) + \nabla^s \delta\vec{u} : \Delta\boldsymbol{\sigma} + \nabla\delta\varphi \cdot \Delta\vec{D} \Big)\, dV, \tag{59}$$

with the occurrence of the material tangent components as introduced in (11).

Having (57) and (59) at hand, a finite element discretization of the problem in (55) can be performed.

### 5.3. Five-field mixed finite element formulation for electro-mechanical problems

Based on the variational principle in (55) a mixed finite element formulation is presented for solving the global electro-mechanical boundary value problem outlined in Section 5.1. For this purpose, the continuous body under consideration is subdivided into a finite number $n_{elem}$ of elements: $\mathcal{B} \approx \bigcup_{e=1}^{n_{elem}} \Omega_e$. Fundamental informations about the finite element method can be found in e.g. Zienkiewicz et al. (2005) and Wriggers (2008). The proposed formulation in this paper is limited to geometrically linear applications, however, a material non-linearity is included. As the point of departure, we take the variation of the five-field potential (57) and its linearization (59). The insertion of suitable shape functions $N_I^{\square}$ and their derivatives $B_I^{\square}$ for the interpolation of the several quantities delivers the discretized version of the weak form in (57) formulated for each element $e$ of the domain as

$$\delta_{\boldsymbol{\varepsilon}}\Pi_e^h = \delta\boldsymbol{\varepsilon}_e^T \boldsymbol{F}_e^{\varepsilon} \qquad \text{with} \qquad \boldsymbol{F}_e^{\varepsilon} = \sum_{I=1}^{n_{el}^{\varepsilon}} \left\{ \int_{\Omega_e} \boldsymbol{N}_I^{\varepsilon T} (\partial_{\boldsymbol{\varepsilon}} W - \tilde{\boldsymbol{\sigma}})\, dV \right\}, \tag{60}$$

$$\delta_{\boldsymbol{D}}\Pi_e^h = \delta\boldsymbol{D}_e^T \boldsymbol{F}_e^{D} \qquad \text{with} \qquad \boldsymbol{F}_e^{D} = \sum_{I=1}^{n_{el}^{D}} \left\{ \int_{\Omega_e} \boldsymbol{N}_I^{DT} (\partial_{\boldsymbol{D}} W + \nabla\varphi)\, dV \right\}, \tag{61}$$

$$\delta_{\tilde{\boldsymbol{\sigma}}}\Pi_e^h = \delta\tilde{\boldsymbol{\sigma}}_e^T \boldsymbol{F}_e^{\tilde{\sigma}} \qquad \text{with} \qquad \boldsymbol{F}_e^{\tilde{\sigma}} = \sum_{I=1}^{n_{el}^{\tilde{\sigma}}} \left\{ \int_{\Omega_e} \boldsymbol{N}_I^{\tilde{\sigma} T} (\nabla^s \boldsymbol{u} - \boldsymbol{\varepsilon})\, dV \right\}, \tag{62}$$

$$\delta_{\boldsymbol{u}}\Pi_e^h = \delta\boldsymbol{u}_e^T (\boldsymbol{F}_e^{u} - \boldsymbol{P}_e^{u}) \qquad \text{with} \qquad \boldsymbol{F}_e^{u} = \sum_{I=1}^{n_{el}^{u}} \left\{ \int_{\Omega_e} \boldsymbol{B}_I^{uT} \tilde{\boldsymbol{\sigma}}\, dV \right\} \quad \text{and} \quad \boldsymbol{P}_e^{u} = \sum_{I=1}^{n_{el}^{u}} \left\{ \int_{\partial\Omega_e} \boldsymbol{N}_I^{uT} \boldsymbol{t}_0\, dA \right\}, \tag{63}$$

$$\delta_{\varphi}\Pi_e^h = \delta\boldsymbol{\varphi}_e (\boldsymbol{F}_e^{\varphi} + \boldsymbol{P}_e^{\varphi}) \qquad \text{with} \qquad \boldsymbol{F}_e^{\varphi} = \sum_{I=1}^{n_{el}^{\varphi}} \left\{ \int_{\Omega_e} \boldsymbol{B}_I^{\varphi T} \boldsymbol{D}\, dV \right\} \quad \text{and} \quad \boldsymbol{P}_e^{\varphi} = \sum_{I=1}^{n_{el}^{\varphi}} \left\{ \int_{\partial\Omega_e} N_I^{\varphi} \omega_0\, dA \right\}, \tag{64}$$

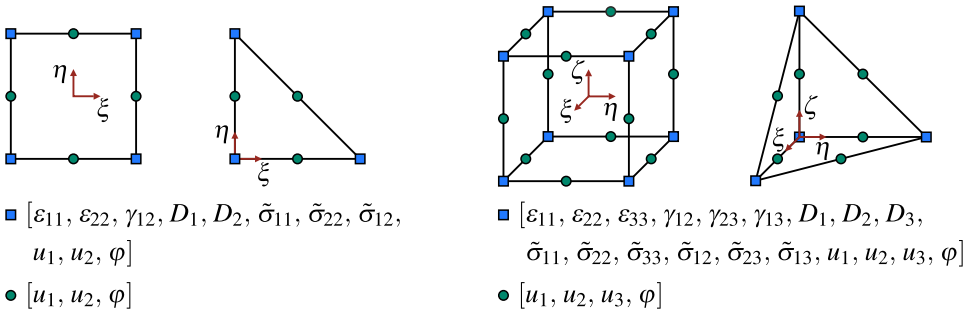


**Fig. 4.** Nodal degrees of freedom of 2D (left) and 3D (right) isoparametric finite elements based on the five-field variational principle (55) ($\gamma_{ij} = 2\varepsilon_{ij}$).

wherein the element vectors of the internal forces $\boldsymbol{F}_e^{\square}$ and the external forces $\boldsymbol{P}_e^{\square}$ can be identified. To be close to computer implementation, in this section, all quantities occurring in (60)–(64) are represented in matrix notation. The components $\partial_{\boldsymbol{\varepsilon}} W$ and $\partial_{\boldsymbol{D}} W$ in (60)–(64) must be determined by a material model at each Gauss point during the numerical evaluation of the respective integral. It should be noted that the nodal stresses $\tilde{\boldsymbol{\sigma}}$ are initially independent variables, which have to be brought into equality at each Gauss point with the material stresses $\boldsymbol{\sigma} = \partial_{\boldsymbol{\varepsilon}} W$ derived via $(10)_1$.

By paying attention to the functional spaces of the different variables in (55), it can be stated that only for the displacement field $\boldsymbol{u}$ and the electric scalar potential $\varphi$ a $C^0$-continuous ansatz is necessary. For the remaining nodal field quantities, namely the strain $\boldsymbol{\varepsilon}$, the electric displacement $\boldsymbol{D}$ and the stress $\tilde{\boldsymbol{\sigma}}$, a piecewise $C^{-1}$-continuous ansatz is required. Therefore, the displacement field and the electric scalar potential are interpolated by quadratic serendipity Lagrange polynomials with continuity across the element boundaries, while for the strain, the electric displacement and the stress discontinuous linear Lagrange polynomials are chosen. The resulting degrees of freedom per node $n_{el}$ of different 2D and 3D isoparametric elements can be seen in Fig. 4. More information on the construction of the used shape functions is given e.g. in Zienkiewicz et al. (2005) and Wriggers (2008). For more sophisticated approximation techniques of the occurring field quantities in electro-mechanical finite element formulations, see Sze and Pan (1999), Klinkel and Wagner (2006, 2008) and Linnemann (2008).

A discretized version of the linearized variation of the five-field potential in (59) is then given by

$$\Delta\delta_{\boldsymbol{\varepsilon}} \Pi_e^h = \delta\boldsymbol{\varepsilon}_e^T (\boldsymbol{H}_e^{\varepsilon\varepsilon} \Delta\boldsymbol{\varepsilon}_e + \boldsymbol{H}_e^{\varepsilon D} \Delta\boldsymbol{D}_e - \boldsymbol{L}_e^{\varepsilon\tilde{\sigma}} \Delta\tilde{\boldsymbol{\sigma}}_e) \quad \text{with} \quad \boldsymbol{H}_e^{\varepsilon\varepsilon} = \sum_{I=1}^{n_{el}^{\varepsilon}} \sum_{K=1}^{n_{el}^{\varepsilon}} \left\{ \int_{\Omega_e} \boldsymbol{N}_I^{\varepsilon T} \boldsymbol{C}_T^{\varepsilon\varepsilon} \boldsymbol{N}_K^{\varepsilon} \, dV \right\},$$
$$\boldsymbol{H}_e^{\varepsilon D} = \sum_{I=1}^{n_{el}^{\varepsilon}} \sum_{I=1}^{n_{el}^{D}} \left\{ \int_{\Omega_e} \boldsymbol{N}_I^{\varepsilon T} \boldsymbol{C}_T^{\varepsilon D} \boldsymbol{N}_K^{D} \, dV \right\} \quad \text{and} \quad \boldsymbol{L}_e^{\varepsilon\tilde{\sigma}} = \sum_{I=1}^{n_{el}^{\varepsilon}} \sum_{I=1}^{n_{el}^{\tilde{\sigma}}} \left\{ \int_{\Omega_e} \boldsymbol{N}_I^{\varepsilon T} \boldsymbol{N}_K^{\tilde{\sigma}} \, dV \right\}, \tag{65}$$

$$\Delta\delta_{\boldsymbol{D}} \Pi_e^h = \delta\boldsymbol{D}_e^T (\boldsymbol{H}_e^{D\varepsilon} \Delta\boldsymbol{\varepsilon}_e + \boldsymbol{H}_e^{DD} \Delta\boldsymbol{D}_e + \boldsymbol{A}_e^{D\varphi} \Delta\boldsymbol{\varphi}_e) \quad \text{with} \quad \boldsymbol{H}_e^{D\varepsilon} = \sum_{I=1}^{n_{el}^{D}} \sum_{K=1}^{n_{el}^{\varepsilon}} \left\{ \int_{\Omega_e} \boldsymbol{N}_I^{DT} \boldsymbol{C}_T^{D\varepsilon} \boldsymbol{N}_K^{\varepsilon} \, dV \right\},$$
$$\boldsymbol{H}_e^{DD} = \sum_{I=1}^{n_{el}^{D}} \sum_{K=1}^{n_{el}^{D}} \left\{ \int_{\Omega_e} \boldsymbol{N}_I^{DT} \boldsymbol{C}_T^{DD} \boldsymbol{N}_K^{D} \, dV \right\} \quad \text{and} \quad \boldsymbol{A}_e^{D\varphi} = \sum_{I=1}^{n_{el}^{D}} \sum_{K=1}^{n_{el}^{\varphi}} \left\{ \int_{\Omega_e} \boldsymbol{N}_I^{DT} \boldsymbol{B}_K^{\varphi} \, dV \right\}, \tag{66}$$

$$\Delta\delta_{\tilde{\boldsymbol{\sigma}}} \Pi_e^h = \delta\tilde{\boldsymbol{\sigma}}_e^T (-\boldsymbol{L}_e^{\tilde{\sigma}\varepsilon} \Delta\boldsymbol{\varepsilon}_e + \boldsymbol{G}_e^{\tilde{\sigma}u} \Delta\boldsymbol{u}_e) \quad \text{with} \quad \boldsymbol{L}_e^{\tilde{\sigma}\varepsilon} = \sum_{I=1}^{n_{el}^{\tilde{\sigma}}} \sum_{K=1}^{n_{el}^{\varepsilon}} \left\{ \int_{\Omega_e} \boldsymbol{N}_I^{\tilde{\sigma}T} \boldsymbol{N}_K^{\varepsilon} \, dV \right\}$$
$$\text{and} \quad \boldsymbol{G}_e^{\tilde{\sigma}u} = \sum_{I=1}^{n_{el}^{\tilde{\sigma}}} \sum_{K=1}^{n_{el}^{u}} \left\{ \int_{\Omega_e} \boldsymbol{N}_I^{\tilde{\sigma}T} \boldsymbol{B}_K^{u} \, dV \right\}, \tag{67}$$

$$\Delta\delta_{\boldsymbol{u}} \Pi_e^h = \delta\boldsymbol{u}_e^T \boldsymbol{G}_e^{u\tilde{\sigma}} \Delta\tilde{\boldsymbol{\sigma}}_e \quad \text{with} \quad \boldsymbol{G}_e^{u\tilde{\sigma}} = \sum_{I=1}^{n_{el}^{u}} \sum_{K=1}^{n_{el}^{\tilde{\sigma}}} \left\{ \int_{\Omega_e} \boldsymbol{B}_I^{uT} \boldsymbol{N}_K^{\tilde{\sigma}} \, dV \right\}, \tag{68}$$

$$\Delta\delta_{\varphi} \Pi_e^h = \delta\boldsymbol{\varphi}_e^T \boldsymbol{A}_e^{\varphi D} \Delta\boldsymbol{D}_e \quad \text{with} \quad \boldsymbol{A}_e^{\varphi D} = \sum_{I=1}^{n_{el}^{\varphi}} \sum_{K=1}^{n_{el}^{D}} \left\{ \int_{\Omega_e} \boldsymbol{B}_I^{\varphi T} \boldsymbol{N}_K^{D} \, dV \right\} \tag{69}$$

for each element in the domain, where several matrices can be identified. In integrals of components $\boldsymbol{H}_e^{\square}$ the material tangent contributions $\boldsymbol{C}_T^{\square} = \partial_{\square}^2 W$ initially derived in (11) and finally determined in (48) can be identified. Assuming a non-linear material behavior, this information must also be provided by a suitable material model. For an iterative solution of the initially derived weak form of the problem (57) by Newton's method, with (60)–(64) and (65)–(69) at hand, an equation determining an incremental update

of the degrees of freedom is given by

$$\delta \Pi_e^h + \Delta\delta \Pi_e^h \overset{!}{=} 0 \quad \Longrightarrow \quad \begin{bmatrix} \boldsymbol{H}_e^{\varepsilon\varepsilon} & \boldsymbol{H}_e^{\varepsilon D} & -\boldsymbol{L}_e^{\varepsilon\tilde{\sigma}} & \boldsymbol{0} & \boldsymbol{0} \\ \boldsymbol{H}_e^{D\varepsilon} & \boldsymbol{H}_e^{DD} & \boldsymbol{0} & \boldsymbol{0} & \boldsymbol{A}_e^{D\varphi} \\ -\boldsymbol{L}_e^{\tilde{\sigma}\varepsilon} & \boldsymbol{0} & \boldsymbol{0} & \boldsymbol{G}_e^{\sigma u} & \boldsymbol{0} \\ \boldsymbol{0} & \boldsymbol{0} & \boldsymbol{G}_e^{u\tilde{\sigma}} & \boldsymbol{0} & \boldsymbol{0} \\ \boldsymbol{0} & \boldsymbol{A}_e^{\varphi D} & \boldsymbol{0} & \boldsymbol{0} & \boldsymbol{0} \end{bmatrix} \begin{bmatrix} \Delta\boldsymbol{\varepsilon}_e \\ \Delta\boldsymbol{D}_e \\ \Delta\tilde{\boldsymbol{\sigma}}_e \\ \Delta\boldsymbol{u}_e \\ \Delta\boldsymbol{\varphi}_e \end{bmatrix} = - \begin{bmatrix} \boldsymbol{F}_e^{\varepsilon} \\ \boldsymbol{F}_e^{D} \\ \boldsymbol{F}_e^{\tilde{\sigma}} \\ \boldsymbol{F}_e^{u} \\ \boldsymbol{F}_e^{\varphi} \end{bmatrix} + \begin{bmatrix} \boldsymbol{0} \\ \boldsymbol{0} \\ \boldsymbol{0} \\ \boldsymbol{P}_e^{u} \\ -\boldsymbol{P}_e^{\varphi} \end{bmatrix} \tag{70}$$

assuming arbitrary and non-vanishing variations $\delta\square$. By introducing $\Delta\boldsymbol{\alpha}_e := [\Delta\boldsymbol{\varepsilon}_e^T \ \Delta\boldsymbol{D}_e^T]^T$ and $\Delta\boldsymbol{v}_e := [\Delta\boldsymbol{u}_e^T \ \Delta\boldsymbol{\varphi}_e^T]^T$, the linear system of equations in (70) can be simplified to

$$\begin{bmatrix} \boldsymbol{H}_e & -\boldsymbol{L}_e & \boldsymbol{A}_e \\ -\boldsymbol{L}_e^T & \boldsymbol{0} & \boldsymbol{G}_e \\ \boldsymbol{A}_e^T & \boldsymbol{G}_e^T & \boldsymbol{0} \end{bmatrix} \begin{bmatrix} \Delta\boldsymbol{\alpha}_e \\ \Delta\tilde{\boldsymbol{\sigma}}_e \\ \Delta\boldsymbol{v}_e \end{bmatrix} = - \begin{bmatrix} \boldsymbol{F}_e^{\alpha} \\ \boldsymbol{F}_e^{\tilde{\sigma}} \\ \boldsymbol{F}_e^{v} \end{bmatrix} + \begin{bmatrix} \boldsymbol{0} \\ \boldsymbol{0} \\ \boldsymbol{P}_e^{v} \end{bmatrix}. \tag{71}$$

Taking into account that the interpolations for the fields $\boldsymbol{\varepsilon}$, $\boldsymbol{D}$ and $\tilde{\boldsymbol{\sigma}}$ do not require continuity across the element boundaries, a static condensation of the corresponding degrees of freedom on the element level is possible. Considering the first two equations in (71), one obtains the incremental changes

$$\Delta\boldsymbol{\alpha}_e = \boldsymbol{H}_e^{-1} \left( \boldsymbol{L}_e \Delta\tilde{\boldsymbol{\sigma}}_e - \boldsymbol{A}_e \Delta\boldsymbol{v}_e - \boldsymbol{F}_e^{\alpha} \right) \qquad \text{and} \tag{72}$$

$$\Delta\tilde{\boldsymbol{\sigma}}_e = (\boldsymbol{L}_e^T \boldsymbol{H}_e^{-1} \boldsymbol{L}_e)^{-1} \left( (\boldsymbol{G}_e + \boldsymbol{L}_e^T \boldsymbol{H}_e^{-1} \boldsymbol{A}_e) \Delta\boldsymbol{v}_e + \boldsymbol{F}_e^{\tilde{\sigma}} + \boldsymbol{L}_e^T \boldsymbol{H}_e^{-1} \boldsymbol{F}_e^{\alpha} \right). \tag{73}$$

Insertion of (72) and (73) into the third equation of (71) delivers the effective element stiffness matrix

$$\begin{aligned} \boldsymbol{K}_{Te}^{eff} = {} & \boldsymbol{G}_e^T (\boldsymbol{L}_e^T \boldsymbol{H}_e^{-1} \boldsymbol{L}_e)^{-1} \boldsymbol{G}_e + \boldsymbol{G}_e^T (\boldsymbol{L}_e^T \boldsymbol{H}_e^{-1} \boldsymbol{L}_e)^{-1} \boldsymbol{L}_e^T \boldsymbol{H}_e^{-1} \boldsymbol{A}_e + \boldsymbol{A}_e^T \boldsymbol{H}_e^{-1} \boldsymbol{L}_e (\boldsymbol{L}_e^T \boldsymbol{H}_e^{-1} \boldsymbol{L}_e)^{-1} \boldsymbol{G}_e \\ & + \boldsymbol{A}_e^T \boldsymbol{H}_e^{-1} \boldsymbol{L}_e (\boldsymbol{L}_e^T \boldsymbol{H}_e^{-1} \boldsymbol{L}_e)^{-1} \boldsymbol{L}_e^T \boldsymbol{H}_e^{-1} \boldsymbol{A}_e - \boldsymbol{A}_e^T \boldsymbol{H}_e^{-1} \boldsymbol{A}_e \end{aligned} \tag{74}$$

and the effective element vector of the internal forces

$$\begin{aligned} \boldsymbol{F}_e^{eff} = {} & \boldsymbol{F}_e^{v} + \left( \boldsymbol{G}_e^T (\boldsymbol{L}_e^T \boldsymbol{H}_e^{-1} \boldsymbol{L}_e)^{-1} + \boldsymbol{A}_e^T \boldsymbol{H}_e^{-1} \boldsymbol{L}_e (\boldsymbol{L}_e^T \boldsymbol{H}_e^{-1} \boldsymbol{L}_e)^{-1} \right) \boldsymbol{F}_e^{\tilde{\sigma}} \\ & + \left( \boldsymbol{A}_e^T \boldsymbol{H}_e^{-1} \boldsymbol{L}_e (\boldsymbol{L}_e^T \boldsymbol{H}_e^{-1} \boldsymbol{L}_e)^{-1} \boldsymbol{L}_e^T \boldsymbol{H}_e^{-1} + \boldsymbol{G}_e^T (\boldsymbol{L}_e^T \boldsymbol{H}_e^{-1} \boldsymbol{L}_e)^{-1} \boldsymbol{L}_e^T \boldsymbol{H}_e^{-1} - \boldsymbol{A}_e^T \boldsymbol{H}_e^{-1} \right) \boldsymbol{F}_e^{\alpha}. \end{aligned} \tag{75}$$

By assembling (74), (75) and the element vectors of the external forces in (71) over all elements of the domain under consideration, one obtains the linear system of equations

$$\bigcup_{e=1}^{n_{elem}} \left( \boldsymbol{K}_{Te}^{eff} \Delta\boldsymbol{v}_e = -(\boldsymbol{F}_e^{eff} - \boldsymbol{P}_e^{v}) \right) \quad \Longrightarrow \quad \boldsymbol{K}_T^{eff} \Delta\boldsymbol{v} = -\boldsymbol{R}^{eff} \tag{76}$$

determining an incremental update of the nodal displacements and the nodal values of the electric potential on the global system level. The iteration with Eq. (76) can be terminated if the effective global residual vector vanishes in a numerical sense: $\|\boldsymbol{R}^{eff}\| < \text{tol}$. An update of the condensed nodal degrees of freedom is performed in each iteration step on element level over (72) and (73). For this recalculation, the element matrices contained in (72) and (73) of the previous iteration step have to be stored in the memory. In this context it should be mentioned that the matrices $\boldsymbol{L}_e$, $\boldsymbol{A}_e$ and $\boldsymbol{G}_e$ do not change during the global equilibrium iteration.

## 6. Numerical examples

In the following section, some numerical examples are presented and the corresponding results are discussed in order to demonstrate the capability of the presented theory and its numerical treatment. For this purpose, the finite element formulation presented in Section 5.3 and the local solution process of the material model in Section 4 is implemented in an in-house FE-Code developed in MATLAB (MATLAB, 2022). A special focus will be on a comparison of the results calculated with the model with experiments reported in the literature.

### 6.1. PZT cube under uniaxial cyclic isolated and combined electro-mechanical loading

In a first example, the behavior described by the microscopically motivated material model introduced in Section 3 is compared to that observed experimentally on the macroscopical scale for ferroelectric polycrystals. Therefore the characteristic hysteresis curves of ferroelectric materials should be reproduced by the model. A unit cube with an edge length chosen in accordance with the used unit system as 1 mm consisting of the soft PZT material PIC 151 fabricated by PI Ceramic GmbH, Lederhose (Germany) is selected as the system under consideration in this example. The adjusted material parameters corresponding to the material model introduced in Section 3 are listed in Table 1. To avoid an ill-conditioned problem, the calculations are performed in a special system of units also used in Laskewitz and Kamlah (2010) and Schwaab et al. (2012). In the beginning of each numerical experiment in this example, it is assumed that the material is in a thermally depolarized state ($\boldsymbol{A} = \boldsymbol{A}_0$, $\vec{\rho} = [0\,0\,0]^T$, cf. Section 3.2). Such a 'virgin' state is commonly assumed for PZT after sintering during the fabrication process. For the finite element calculations, the cube is discretized by a mesh identical to a well-known patch test (MacNeal and Harder, 1985). In this example, hexahedral quadratic serendipity finite elements (cf. Section 5.3) are used. With a fixed normal displacement at three surfaces of the cube, the mechanical boundary

**Table 1**
Material parameters chosen for the soft PZT PIC 151.

| Parameter | Symbol | Value | Unit | | Calc. Value | Calc. Unit |
|---|---|---|---|---|---|---|
| Young's modulus | $Y$ | 45000 | MPa | | 45 | kN/mm$^2$ |
| Poisson's ratio | $\nu$ | 0.31 | – | | 0.31 | – |
| Piezoelectric constants[a] | $d_{33}$ | $0.7 \cdot 10^{-9}$ | m/V | | 0.70 | mm/MV |
| | $d_{31}$ | $-0.29 \cdot 10^{-9}$ | m/V | | −0.29 | mm/MV |
| | $d_{15}$[b] | $0.99 \cdot 10^{-9}$ | m/V | | 0.99 | mm/MV |
| Vacuum permittivity* | $\epsilon_0$ | $8.854 \cdot 10^{-12}$ | C/(Vm) | | $8.854 \cdot 10^{-3}$ | kN/MV$^2$ |
| Dielectric susceptibility | $\kappa^\sigma$ | $30 \cdot 10^{-9}$ | C/(Vm) | | 30 | kN/MV$^2$ |
| Coercive field strength | $E^c$ | $0.95 \cdot 10^6$ | V/m | | $0.95 \cdot 10^{-3}$ | MV/mm |
| Coercive stress | $\sigma^c$ | 25 | MPa | $\triangleq$ | $25 \cdot 10^{-3}$ | kN/mm$^2$ |
| Saturation polarization | $P^{sat}$ | 0.38 | C/m$^2$ | | 0.38 | kN/(MVmm) |
| Saturation strain | $\epsilon^{sat}$ | 0.0026 | – | | 0.0026 | – |
| Hardening parameters | $c_A$ | 0.1 | MPa | | $1 \cdot 10^{-4}$ | kN/mm$^2$ |
| | $c_\rho$ | 0.025 | MPa | | $2.5 \cdot 10^{-5}$ | kN/mm$^2$ |
| Energy barrier parameters | $a_A$ | $1 \cdot 10^{-4}$ | MPa | | $1 \cdot 10^{-7}$ | kN/mm$^2$ |
| | $m_A$ | 0.5 | – | | 0.5 | – |
| | $a_\rho$ | 0.01 | MPa | | $1 \cdot 10^{-5}$ | kN/mm$^2$ |
| | $m_\rho$ | 1.0 | – | | 1.0 | – |
| Distance variable parameter | $\xi$ | 0.15 | – | | 0.15 | – |

*Natural constant.

[a]The parameters chosen here vary from those given by PI Ceramic (PI Ceramic GmbH, 2016). Our choice is motivated by the attempt to represent the non-linear large-signal behavior (which can be observed in poling processes) as precisely as possible. The specified parameters of PI Ceramic correspond to the linear piezoelectric behavior under the action of low electric fields, which is more relevant for technical applications.

[b]Since the $d_{15}$-parameter is very difficult to determine experimentally, the common estimate $d_{15} = d_{33} - d_{31}$ is made here, see Berlincourt and Jaffe (1958).

conditions are chosen in a way that a stress-free deformation caused by electrical induced switching processes of the structure can be expected, cf. Fig. 5 e). The electric potential at the bottom surface is fixed to zero for all cases under consideration in this example in order to represent a grounded electrode. Depending on the situation to be considered, on the top surface, an electric potential or/and a mechanical traction in global $x_3$-direction with a time-varying amplitude is prescribed. To be close to the experiments in this numerical example, the changes in the observed quantities are evaluated in a special way from the calculated nodal results. The strains are calculated by the differences in the nodal displacements of the respective two opposite faces divided by the unit dimension of the cube. The electric displacement is evaluated by an integrated value of the equivalent surface charges at the top surface. Furthermore, the values given in the results for the mechanical stress and the electric field are the acting external loadings prescribed by the introduced boundary conditions.

**Remark.** Note, the material parameters defining the linear electro-mechanically coupled behavior listed among others in Table 1 cannot be chosen completely independently of each other in order to obtain a positive definite linear material matrix. In Stark et al. (2016) conditions are specified which must be fulfilled in order to ensure a positive definiteness of the linear material moduli. The authors can report from their own experience that ignoring these conditions often leads to convergence problems during the global Newton iteration in poling simulations.

*6.1.1. Characteristic hystereses of ferroelectric materials*

In the first case, the material response under the action of an external electric field without any mechanical stresses is considered. Therefore the prescribed electric potential at the top surface of the cube is cycled with an amplitude of $\varphi_0^{max} = \pm 2$ kV. The resulting maximum vertical electric field $E_3$ acting on the cube corresponds to then approximately twice the coercive field strength $E^c$ (cf. Table 1). In Fig. 5 a) the dielectric hysteresis calculated numerically with the model presented is compared to the experimental measurement by Zhou (2003). It is obvious that the model can capture the domain switching processes as well as the saturation behavior in the material in a quite proper way in order to reproduce their influence on the macroscopical polarization state. Furthermore, the comparison of the longitudinal and transversal butterfly hystereses is shown in Fig. 5 b) and c) demonstrating the prediction of the change in the deformations state caused by switching processes is also in good agreement with the results in Zhou (2003).

To demonstrate the numerical stability and efficiency, the convergence rates of the proposed algorithms should be discussed for a relatively large load step by analyzing the local and global residua introduced in (38) and (76). We focus on the loading scenario in between two material states marked by the two crosses in Fig. 5 a)–c), where the applied electric potential is increased from $\varphi_0 = 0.7$ kV to $\varphi_0 = 1.05$ kV. Note that within this step the transition from reversible to irreversible material behavior is passed. Table 2 shows the corresponding convergence rates. It can be clearly seen that a quadratic convergence behavior exists for the local iteration at the Gauss point as well as for the global finite element iteration. It also becomes clear that the solution process turns out to be a pure descent procedure.

In the next situation under consideration, the material response under the action of a purely mechanical loading is in focus. Starting again from a totally unpolar state, the prescribed mechanical compressive traction is increased up to $\sigma_0^{p,max} = -400$ MPa. After unloading a tensile traction is applied up to $\sigma_0^{t,max} = 200$ MPa. By repeating the compressive loading with an amplitude of

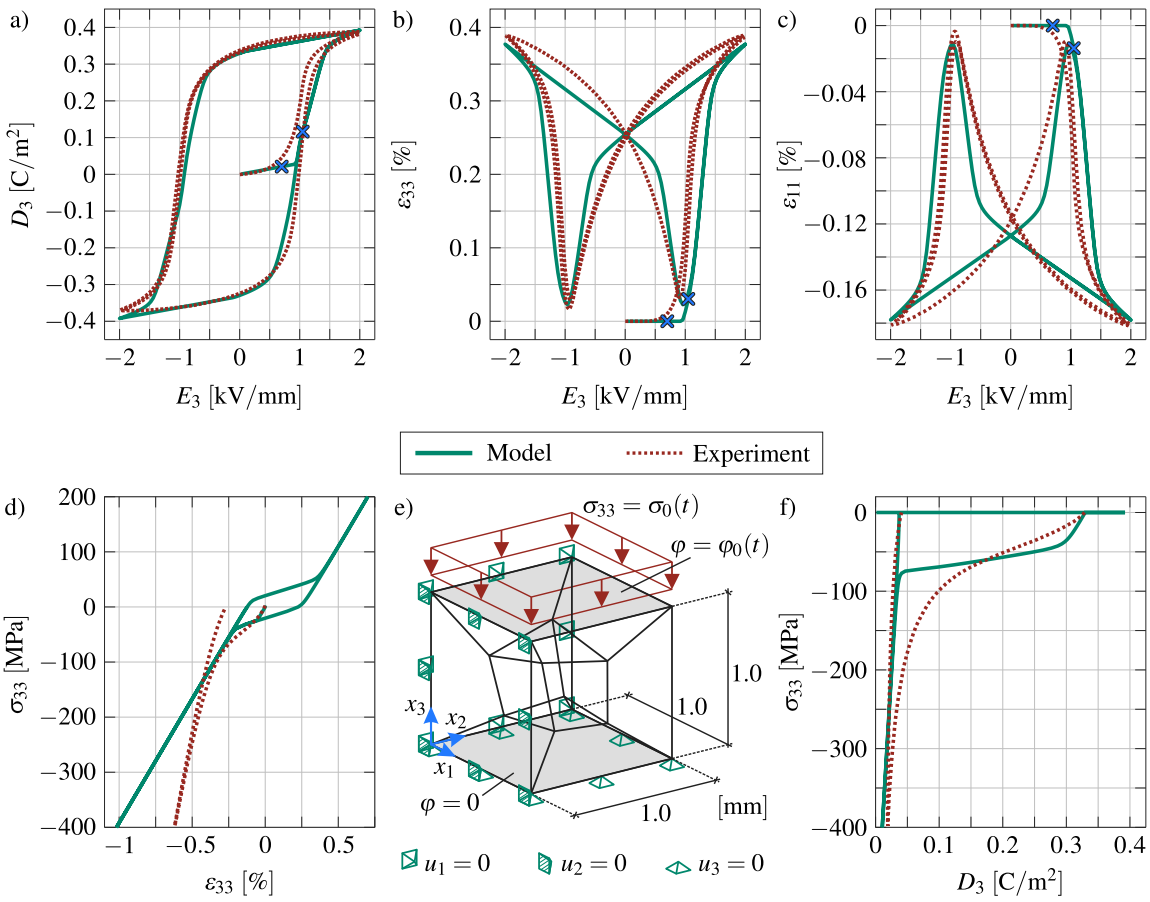


**Fig. 5.** Comparison of the macroscopic model response with experimental hysteresis measured by Zhou (2003) for different cyclic electrical or/and mechanical loading processes: a) dielectric hysteresis, b) longitudinal butterfly hysteresis, c) transversal butterfly hysteresis, d) ferroelastic hysteresis, e) finite element model under consideration with prescribed boundary conditions, f) mechanical depolarization after initial poling process.

**Table 2**
Convergence behavior of the global finite element Newton iteration and the local iterations performed at a Gauss point.

| No. glob. iter. | 1 | 2 | 3 | 4 | 5 | 6 | 7 |
|---|---|---|---|---|---|---|---|
| $\|\boldsymbol{R}^{eff}\|$ cf. (76) | $9.7 \cdot 10^{-02}$ | $2.3 \cdot 10^{-02}$ | $9.0 \cdot 10^{-03}$ | $1.1 \cdot 10^{-03}$ | $1.4 \cdot 10^{-05}$ | $2.1 \cdot 10^{-09}$ | $1.5 \cdot 10^{-16}$ |
| No. loc. iter. | $\|\boldsymbol{R}\|$ cf. (38) | | | | | | |
| 1 | $2.2 \cdot 10^{-01}$ | $2.4 \cdot 10^{+01}$ | $2.1 \cdot 10^{+01}$ | $1.8 \cdot 10^{+01}$ | $1.7 \cdot 10^{+01}$ | $1.7 \cdot 10^{+01}$ | $1.7 \cdot 10^{+01}$ |
| 2 | $1.0 \cdot 10^{-02}$ | $7.1 \cdot 10^{+00}$ | $6.1 \cdot 10^{+00}$ | $5.1 \cdot 10^{+00}$ | $5.0 \cdot 10^{+00}$ | $5.0 \cdot 10^{+00}$ | $5.0 \cdot 10^{+00}$ |
| 3 | $3.6 \cdot 10^{-05}$ | $3.8 \cdot 10^{+00}$ | $3.0 \cdot 10^{+00}$ | $2.3 \cdot 10^{+00}$ | $2.3 \cdot 10^{+00}$ | $2.3 \cdot 10^{+00}$ | $2.3 \cdot 10^{+00}$ |
| 4 | $7.1 \cdot 10^{-09}$ | $1.9 \cdot 10^{+00}$ | $1.4 \cdot 10^{+00}$ | $1.1 \cdot 10^{+00}$ | $1.0 \cdot 10^{+00}$ | $1.0 \cdot 10^{+00}$ | $1.0 \cdot 10^{+00}$ |
| 5 | $4.8 \cdot 10^{-17}$ | $5.9 \cdot 10^{-01}$ | $3.9 \cdot 10^{-01}$ | $2.6 \cdot 10^{-01}$ | $2.5 \cdot 10^{-01}$ | $2.5 \cdot 10^{-01}$ | $2.5 \cdot 10^{-01}$ |
| 6 | | $1.0 \cdot 10^{-01}$ | $5.5 \cdot 10^{-02}$ | $3.0 \cdot 10^{-02}$ | $2.8 \cdot 10^{-02}$ | $2.8 \cdot 10^{-02}$ | $2.8 \cdot 10^{-02}$ |
| 7 | | $6.7 \cdot 10^{-03}$ | $2.1 \cdot 10^{-03}$ | $6.7 \cdot 10^{-04}$ | $5.7 \cdot 10^{-04}$ | $5.7 \cdot 10^{-04}$ | $5.7 \cdot 10^{-04}$ |
| 8 | | $3.4 \cdot 10^{-05}$ | $3.6 \cdot 10^{-06}$ | $3.9 \cdot 10^{-07}$ | $2.9 \cdot 10^{-07}$ | $2.9 \cdot 10^{-07}$ | $2.9 \cdot 10^{-07}$ |
| 9 | | $7.9 \cdot 10^{-10}$ | $9.0 \cdot 10^{-12}$ | $1.1 \cdot 10^{-13}$ | $6.1 \cdot 10^{-14}$ | $6.0 \cdot 10^{-14}$ | $6.0 \cdot 10^{-14}$ |
| 10 | | $6.2 \cdot 10^{-17}$ | $6.5 \cdot 10^{-17}$ | $2.3 \cdot 10^{-16}$ | | | |

$\sigma_0^{p,max} = -400$ MPa the cycle is closed and the resulting stress–strain relation becomes the commonly called ferroelastic hysteresis, cf. Fig. 5 d). A comparison with the experimental results of Zhou (2003) shows a good match in the first loading path until a compression level of around $\sigma_0^p = -100$ MPa. For higher loadings, the agreement of the results gets poorer. The adapted Young's modulus to the first loading path and the experimentally observed continuously changing stiffness of PZT with increasing compressive stresses (see e.g. Fett et al., 2002) is the reason for this discrepancy. Furthermore, the mismatch in the remanent strain states after unloading has its roots in the assumed initial state of the texture tensor ($\alpha_i = 1/3$), which leads to a ratio between the remanent tensile and

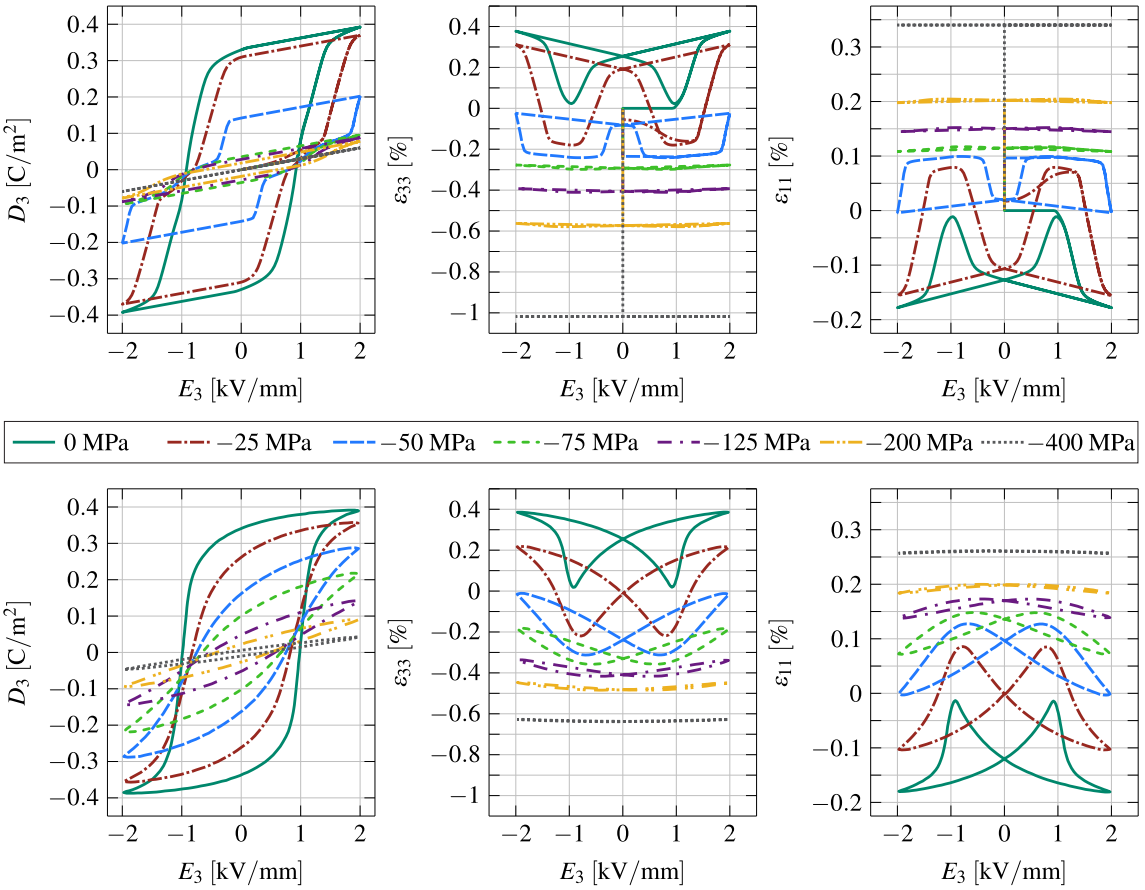


**Fig. 6.** Comparison of macroscopic dielectric hystereses (left), longitudinal butterfly hystereses (middle) and transversal butterfly hystereses for different magnitudes of compressive prestress calculated by the model (top) with experimentally measured by Zhou et al. (2005b) (bottom).

compressive strain of 2:1[8]. This ratio, valid for a tetragonal single crystal, is obviously too high in order to match the remanent strain state after compression of a polycrystal. A comparison in the tensile regime is not possible due to the brittleness of the material and the resulting lack of experimental data.

In order to complete the demonstration of the characteristic hysteretic behavior of ferroelectric materials, a mechanical depolarization process is simulated. For this purpose, an initial poling process is performed by increasing the electric potential at the top surface up to $\varphi_0 = -2$ kV. After unloading a remanent polarization state around $P_3^i = 0.33$ C/m$^2$ remains in the cube. Following successive increasing of the mechanical compressive stress up to $\sigma_0^{p,max} = -400$ MPa in poling direction leads to a decrease of the polarization state in the material. The depolarization path as well as the remaining residual polarization in the material matches the experimental observations in Zhou (2003) in a satisfying manner.

### *6.1.2. Ferroelectric behavior with uniaxial prestress*

In the next step, scenarios with simultaneous electrical and mechanical loading are taken into account. First, the influence of mechanical compressive stress on the dielectric hysteresis and the butterfly hystereses is under consideration. To do this, a mechanical compressive stress in the global $x_3$-direction is first applied to the sample. In total, seven simulations are performed with varying compression levels from 0 MPa to a maximum of −400 MPa. After this prestressing process, the electric potential at the top surface is cycled with the same amplitude as in Section 6.1.1, while the stress level is held constant. In Fig. 6 (top) the resulting hystereses from the numerical simulations are shown for the different levels of prestress. Also for these special load scenarios, a comparison to experimental results (Fig. 6, bottom) is done. Focusing on how the mechanical prestress influences dielectric hysteresis, it can be stated that the decrease of the maximum reachable polarization with increasing compressive stress can be reproduced by the model in a proper way as well as the possibility of complete vanishing of any hysteresis for very high stress levels. But obviously, the model overestimates this compression of the hysteresis for certain stress levels.

[8] A realistic ratio can be determined with micromechanical simulations on a polycrystal. Lu et al. (1999), Fröhlich (2001) and Landis et al. (2004) calculated it to be around 1.37:1.

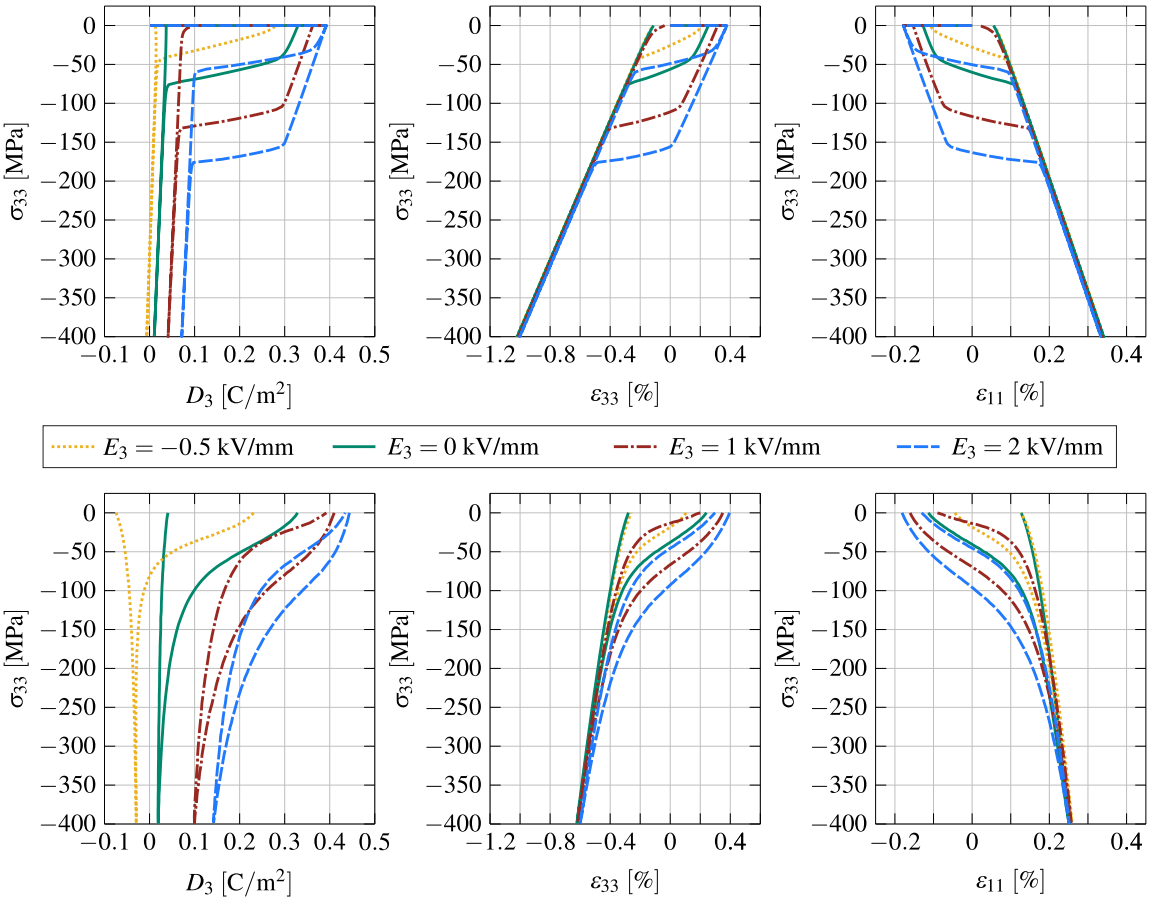


**Fig. 7.** Comparison of macroscopic depolarization behavior (left), longitudinal ferroelastic hystereses (middle) and transversal ferroelastic hystereses under the action of different bias electric field intensities calculated by the model (top) with experimentally measured by Zhou et al. (2005a) (bottom).

By comparing the longitudinal and transversal butterfly hystereses, it can be stated that the translation into the negative strain regime and the initial vertical stretching of the hysteresis for moderate stress levels is captured. Similar to the observations for the polarization state also a complete vanishing of the hystereses for high compressive stress is shown by the model in agreement with the experiments. The larger negative strain levels in the results of the model can be explained by the chosen comparably low Young's modulus (cf. Section 6.1.1).

### 6.1.3. *Mechanical depolarization behavior with bias electric field*

Furthermore, the influence of a superimposed electric bias field on the mechanical depolarization behavior is the subject of discussion. In this example, an initial poling process is performed by first successive increasing the electric potential at the top surface of the cube up to $\varphi_0^{max} = -2$ kV. After this step, the electric potential is adjusted to a certain value corresponding to the case under consideration. Four different bias electric field intensities are considered in the range from $E_3 = -0.5$ kV/mm up to $E_3 = 2$ kV/mm. The resulting electric potentials to be applied vary accordingly from $\varphi_0 = 0.5$ kV to $\varphi_0 = -2$ kV. As soon as this state is reached, the electric potential is kept constant and a steadily increasing uniaxial mechanical compressive stress is applied in order to initiate the depolarization process. Therefore, the stress is increased up to $\sigma_0 = -400$ MPa.

In Fig. 7 (top, left) the model response regarding the mechanical depolarization behavior is shown. In agreement with the experimentally observed behavior in Zhou et al. (2005a) (Fig. 7 bottom, left), an acting electric bias field in the initial poling direction hinders the depolarization process and increases the remaining polarization state when reaching the maximum compression state. Furthermore, the ability to recover the polarization state during unloading is also included in the model. In contrast to that, a destabilizing electric field of $E_3 = -0.5$ kV/mm favors the depolarization process while the slight build-up of an oppositely oriented polarization is not represented by the model as no evolution of the internal variables at all is induced for loadings lower than the switching criterion.

Next, we want to focus on the stress–strain responses during the depolarization processes for different electric bias fields. Therefore, the longitudinal and transversal strain response computed by the model (Fig. 7 top, middle/right) is also compared to the experimental results in Zhou et al. (2005a) (Fig. 7 bottom, middle/right). Similar to the hystereses observed in the depolarization

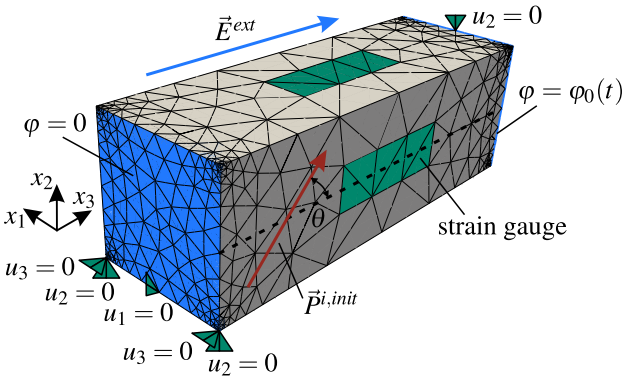


**Fig. 8.** Finite element model of the cut PZT specimen (15 mm × 5 mm × 5 mm) of the polarization rotation test in Zhou et al. (2006b) with the prescribed electrical and mechanical boundary conditions. The initial poling angle $\theta$ varies from 0° to 180°.

behavior the results are in good agreement in order to reproduce the changes in the deformation state caused by the switching processes induced by the acting stress. The obvious discrepancies of mechanical stiffnesses in the saturated regime have the same reasons already discussed in Section 6.1.1 for the purely ferroelastic behavior.

### 6.2. Polarization rotation test

In the next numerical example, an experiment carried out by Huber and Fleck (2001) and Zhou et al. (2006b) examining the multi-axial polarization rotation behavior of PZT is to be reproduced with the model presented. In the experiment of Zhou et al. (2006b), specimens of the size 15 mm × 5 mm × 5 mm consisting of PIC 151 (cf. Section 6.1) were cut out of a large pre-poled ($E^{max} = 2.5$ kV/mm) plate with varying cutting angles $\theta$ (0° to 180°) with respect to the initial poling direction. After this process, electrodes were applied to the top and bottom surfaces of the specimens. For more details on the specimen preparation, we refer to Zhou et al. (2006b). During steadily increasing electric field in the axial specimen direction up to 2 kV/mm, the changes in the polarization and strain states are monitored. In order to reproduce the experiment virtually, a finite element simulation of this polarization rotation process is performed. The corresponding finite element model consisting of quadratic tetrahedral elements (cf. Section 5.3) is shown in Fig. 8 where the prescribed boundary conditions are also given. The mechanical boundary conditions are chosen to a necessary minimum so that no mechanical constraint on the structure is expected. The electric potential at one of the small side faces is stepwise increased up to $\varphi_0^{max} = -2$ kV in 40 equidistant load steps causing an acting external electric field $E_3^{ext}$ in the global $x_3$-direction. The initial irreversible polarization state $\vec{P}^{i,init}$ is placed in the $x_2 - x_3$-plane for all cutting angles $\theta$. In this example, the same material parameters are chosen as for the examples in Section 6.1 (cf. Table 1).

It should be mentioned that the consideration of an initial polarization state $\vec{P}^{i}(t = 0) = \vec{P}^{i,init}$ and the associated initial strain state $\boldsymbol{\varepsilon}^{i}(t = 0) = \boldsymbol{\varepsilon}^{i,init}$ is not trivial in a finite element calculation for this example. In order to prevent the occurrence of internal bias stress states and electric fields at the beginning of the calculation, additionally an imprinted polarization $\vec{P}^{impr} = \vec{P}^{i,init}$ and an imprinted strain state $\boldsymbol{\varepsilon}^{impr} = \boldsymbol{\varepsilon}^{i,init}$ is taken into account in the constitutive equations

$$\boldsymbol{\sigma} = \mathbb{C}^{D} : (\boldsymbol{\varepsilon} + \boldsymbol{\varepsilon}^{impr} - \boldsymbol{\varepsilon}^{i}) - \mathbb{h} \cdot (\vec{D} + \vec{P}^{impr} - \vec{P}^{i}) \qquad \text{and} \qquad \vec{E} = -\mathbb{h} : (\boldsymbol{\varepsilon} + \boldsymbol{\varepsilon}^{impr} - \boldsymbol{\varepsilon}^{i}) + \boldsymbol{\beta}^{\varepsilon} \cdot (\vec{D} + \vec{P}^{impr} - \vec{P}^{i}) \tag{77}$$

of the material model introduced in Section 3. These imprinted components are then kept constant over the entire calculation while the physically correct states of the electric displacement and the strain can be computed by

$$\vec{D}^{phy} = \vec{P}^{impr} + \Delta\vec{D} \qquad \text{and} \qquad \boldsymbol{\varepsilon}^{phy} = \boldsymbol{\varepsilon}^{impr} + \Delta\boldsymbol{\varepsilon} \tag{78}$$

while the physically reasonable changes compared to the initial states are directly recorded here by the absolute calculated values, i.e. $\Delta\vec{D} = \vec{D}$ and $\Delta\boldsymbol{\varepsilon} = \boldsymbol{\varepsilon}$. The initial states $\vec{P}^{i,init}$ and $\boldsymbol{\varepsilon}^{i,init}$ are determined by separate calculations by the material model with a predefined external electric field vector with $\|\vec{E}\| = 2.5$ kV/mm corresponding to the cutting angle $\theta$.

In this example, special attention must be paid to the electrical boundary conditions on the top and bottom surfaces, especially in cases with occurring initial polarization components in the $x_2$-direction. Same as in Stark et al. (2016b) we assume bounded surface charges at the top and bottom surface implicitly realized by the non-vanishing imprinted polarization component $P_2^{impr}$. Due to this special methodology, these surfaces can be assumed to be charge-free in the finite element model, i.e. $\vec{D} \cdot \vec{n} = 0$. During a reduction of the irreversible polarization component $P_2^{i}$ the imprinted and bounded surface charges lead to an electric field component $E_2$ perpendicular to the actual loading direction which hinders the further rotation process of the polarization state. A more sophisticated discussion about the electrical boundary conditions in the transversal $x_2$-direction for the most critical case $\theta = 90°$ can be found in Stark et al. (2016b).

To be close to the experiment in Zhou et al. (2006b), the strain state of the specimens is evaluated by the displacement differences over the domain of the strain gauges glued at the surfaces in the experiments, cf. Fig. 8. The electric displacements are evaluated

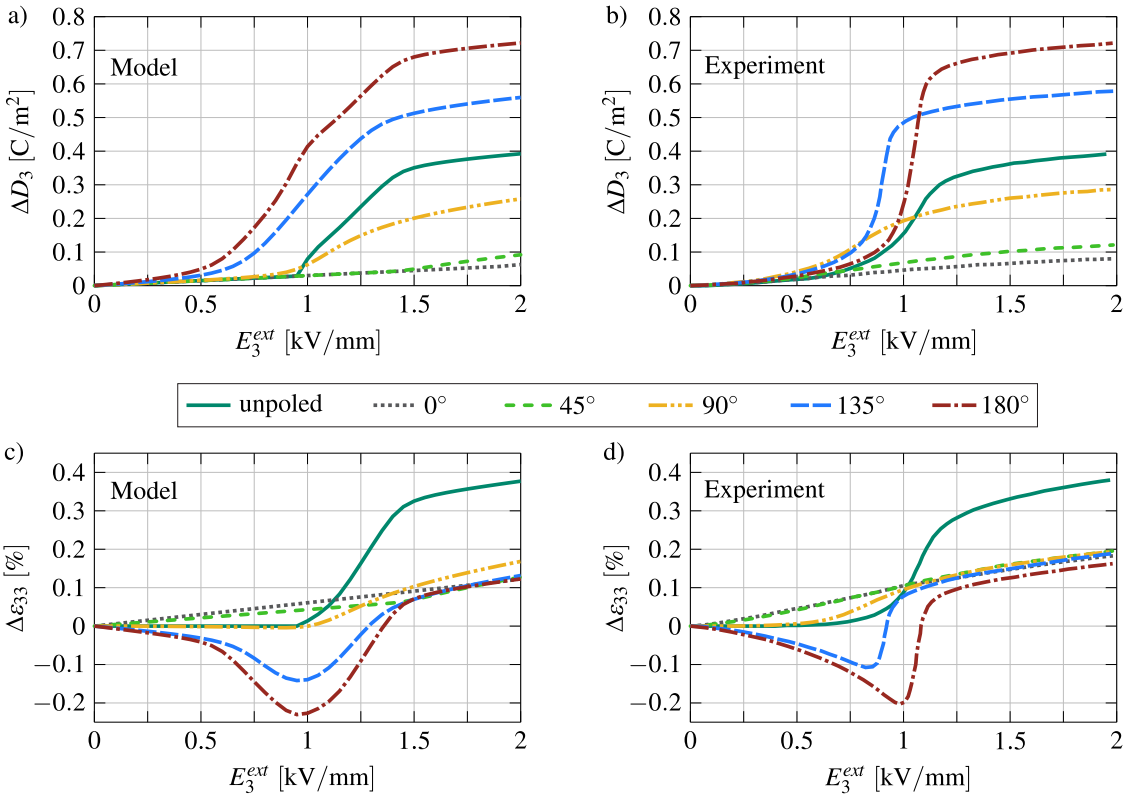


**Fig. 9.** Comparison of the numerical results (left) with the experimentally determined results of Zhou et al. (2006b) (right) for the polarization rotation test. a), b): Changes in the electric displacement component $\Delta D_3$ in the acting electric field $x_3$-direction. c), d): Changes in the strain component $\Delta\varepsilon_{33}$ in acting electric field $x_3$-direction.

by integration of the equivalent surface charges at the contacted electrode while the electric field is directly given by the prescribed potential difference. These special evaluations are necessary due to the occurring inhomogeneities in the strain and polarization distributions especially for the case $\theta = 90°$, see Stark et al. (2016b).

In the following, the results for the initial poling angles $\theta \in \{0°, 45°, 90°, 135°, 180°\}$ are under consideration. They also should be compared to the behavior observed for an initially unpoled specimen. In Fig. 9, the results of the numerical polarization rotation tests (left) are compared to the experimental results (right) obtained by Zhou et al. (2006b). Focusing on the comparison of the changes in the electric displacement in axial $x_3$-direction (top, a) and b)), it can be determined that the final states at $E_3^{ext} = 2$ kV/mm calculated by the model are in a very good agreement with the experimental values. But also some discrepancies need to be discussed. Especially for the larger initial polarization angles, the switching processes are initiated at a lower electric field for the model compared to the experimental results. Obviously, the kinematic hardening effect taken into account in the model is more pronounced than in the real material behavior observed in this special case under consideration. Furthermore, it can be stated that the model underestimates the resistance against 180° switching processes (cf. Section 3.1) while it rather overestimates the resistance against 90° switching processes (see results for $\theta = 90°$).

The comparison of the changes in the axial strain $\Delta\varepsilon_{33}$ (Fig. 9, c) and d)) during the rotation process shows a good match while the strain states at the final configuration slightly deviate. For the larger initial poling angles $\theta = 135°$ and $\theta = 180°$ the maximum negative strains in the interim state where the domains are aligned in vertical $x_2$-direction are a bit overestimated by the model. In accord with the observations in the changes in the electric displacement, for the case $\theta = 90°$ the elongation in $x_3$-direction takes place earlier in the experiment.

Focusing on the variation of the second strain component in the rotation plane $\Delta\varepsilon_{22}$ (Fig. 10, a) and b)), it can be mentioned that the contraction in the final state ($E_3^{ext} = 2$ kV/mm) is underestimated by the model for all cases. For the initial poling angle $\theta = 90°$ the highest contraction is observed in agreement with the experimental observation. In the same curve, a minor intermediate extension in the $x_2$-direction is shown in the simulated results. This effect cannot be seen at all in the real material behavior.

The results of the strain component perpendicular to the rotation plane $\Delta\varepsilon_{11}$ are shown in Fig. 10, c) and d). For most cases, the experimentally measured results are quite well matched by the model. Noticeable are the discrepancies for the angle $\theta = 135°$. The initial slope of the strain changes for comparably low electric field intensities deviates in the comparison as well as the maximum values of the interim extension. Similar to the strain components $\Delta\varepsilon_{22}$ there are small deviations in the final strain states at the maximum electric field.

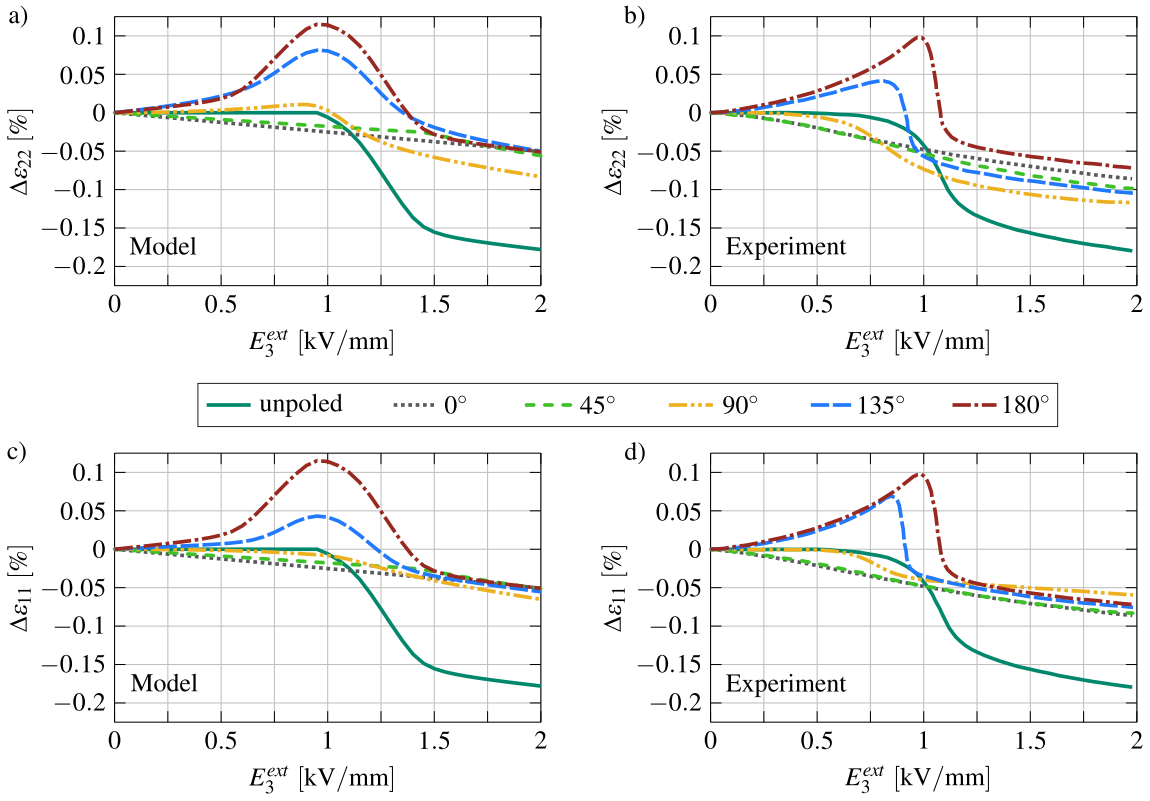


**Fig. 10.** Comparison of the numerical results (left) with the experimentally determined results of Zhou et al. (2006b) (right) for the polarization rotation test. a), b): Changes in the strain component $\Delta\varepsilon_{22}$ transversal to the acting electric field $x_3$-direction (in rotation plane). c), d): Changes in the strain component $\Delta\varepsilon_{11}$ transversal to the acting electric field $x_3$-direction (perpendicular to rotation plane).

Next, we want to take a look at the changes in the local distributions of the polarization and the caused deformation of the specimens. In Fig. 11 specimen configurations for the initial state ($\vec{P}^i = \vec{P}^{i,init}$ and $E_3^{ext} = 0$ kV/mm) and for the final state at $E_3^{ext} = 2$ kV/mm are illustrated. In this figure, the deformation of the specimens is shown with a scaling factor of 75. Furthermore, the contours indicate the intensity of the irreversible polarization component in the global $x_3$-direction while the black arrows represent the direction of the irreversible polarization vector at the corresponding point in the specimen. In the following the basic characteristics of the rotation process for the different initial poling angles are summarized briefly:

**unpoled**: Starting from a thermally depolarized state the polarization increases homogenously over the whole specimen in the direction of the acting electric field and reaches a saturated state. As a result of this, a homogeneous elongation in the $x_3$-direction along with a contraction in the transversal directions evolves. No polarization rotation takes place.

**$\theta = 0°$**: Due to the uniaxial alignment of the domains with the external electric field, the polarization increases only by the linear dielectric contribution. Also, the strain slightly increases due to the converse piezoelectric effect. No polarization rotation takes place.

**$\theta = 45°$**: A moderate rotation of the polarization vectors is observable, but obviously, the electric field strength is not high enough to cause a complete alignment in the electric field direction. The deformation of the sample is not greatly affected in this case. Noteworthy is the stronger rotation of the polarization at the top front edge and bottom back edge compared to the other two edges perpendicular to the $x_3 - x_2$-rotation-plane. This is a result of the highly inhomogeneous electric field distribution in the sample caused by the tilted polarization orientation.

**$\theta = 90°$**: The polarization distribution in the specimen becomes highly inhomogeneous when the maximum external electric field $E_3^{ext}$ is reached. Again the most strongly rotated vectors are located at the top front edge and the bottom back edge, while the domains at the other two edges experience no rotation at all. Consistently with this observation a strong deformation of the specimen is caused by the inhomogeneity of the domain orientation.

**$\theta = 135°$**: Quite similar observations as for the case $\theta = 90°$, but a larger rotation in the direction of the external electric field can be noticed. Also, over a larger volume, a homogeneous polarization state occurs. The deformation is even larger than for the initial poling angle $\theta = 90°$. Due to the preferable diagonal orientation from the bottom front edge to the top back edge an elongation in this direction leads to the parallelogram-like deformation pattern.

**$\theta = 180°$**: Starting from a total reversely poled state passing a completely depolarized intermediate state the polarization reaches a homogeneous and fully oriented state at maximum load level. The deformation state produced for this case is the same as for $\theta = 0°$, cf. the model response in Section 6.1.1.

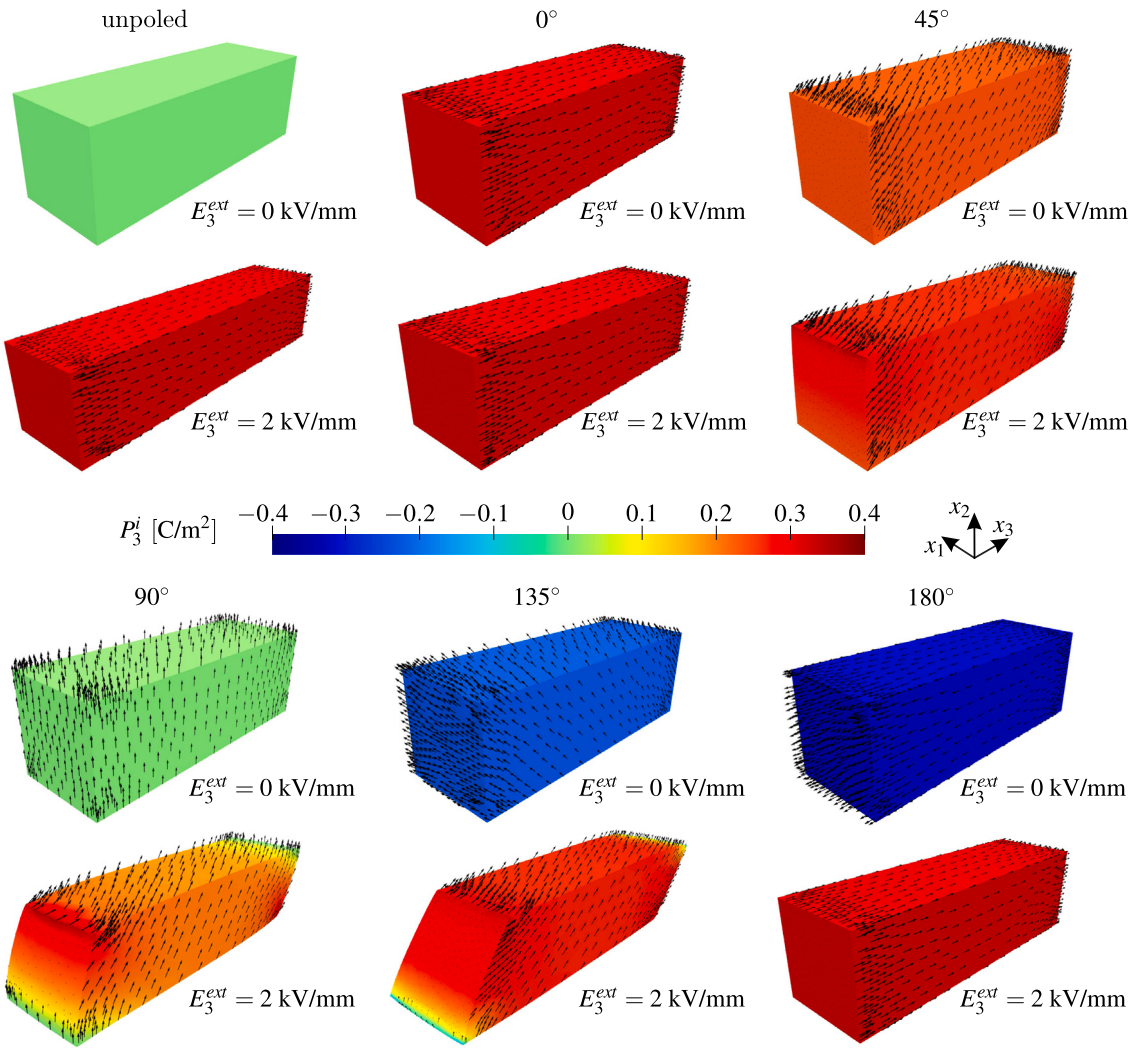


**Fig. 11.** Illustration of the changes in the polarization distribution and the caused deformation of the specimen during the rotation test for the different cutting angles under consideration. The contours indicate the irreversible polarization intensity of the component in the applied electric field direction while the black arrows show the direction of the local irreversible polarization vector. In this figure, the deformation is scaled by a factor of 75.

### 6.3. Parallel electrode wafer

After demonstrating the capability of the model to predict the basic material behavior of ferroelectrics (cf. Sections 6.1 and 6.2), a more practical example that is also relevant for technical applications is under consideration. In Seyfert et al. (2022), PZT wafers consisting of PIC 151 with different single-side electrode layouts are investigated. For instance, such interdigitated transducer (IDT) structures are used in micropumps and -valves (Zähringer et al., 2010). In this example, we want to focus on a parallel electrode arrangement, cf. Fig. 12. In such a design under consideration, a very strong inhomogeneous electric field distribution with high field intensities particularly at the electrode edges occurs (Zähringer et al., 2014). These conditions also highly affect the domain switching processes and lead to inhomogeneous polarization and strain distributions in the PZT wafer.

In the following, a simplified 2D cross-section model of such a single-side electrode wafer is investigated numerically. Here, the focus is on the deformation behavior on the one hand and on the switching processes on the other hand under the effect of a cyclic external electric field. A 2D finite element model consisting of plain strain quadratic serendipity elements (cf. Section 5.3) is chosen where the symmetry of the parallel electrode arrangement is exploited, see Fig. 12. The wafer thickness is given by 250 μm (L. Seyfert, N. Schwesinger, TU Munich, personal communication, October 12, 2021) and the width is assumed as 650 μm. The distance in between the two parallel electrodes $\delta$ is considered as a design parameter since it will have a major impact on the behavior of the wafer, as will be seen later. The structure of the mesh is chosen in such a way that the area in which the strongest electric field gradients are expected is discretized most finely. In order to take the surrounding material into account, in the symmetry plane as well as at the right end of the model the normal displacements in $x_1$-direction are fixed. Furthermore, at the right bottom node, the

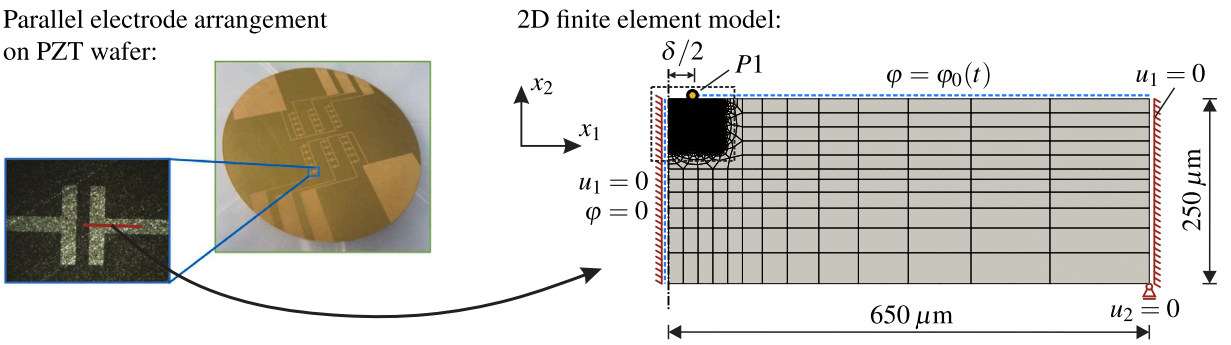


**Fig. 12.** Left: Real PZT wafer investigated in Seyfert et al. (2022) with a detailed view of the parallel electrode arrangement. Right: Simplified 2D finite element model of a symmetrized cross-section of the wafer with the prescribed boundary conditions. The electrode distance $\delta$ is initially assumed to be variable. The point $P1$ as well as the area in the dashed box should be examined in more detail.

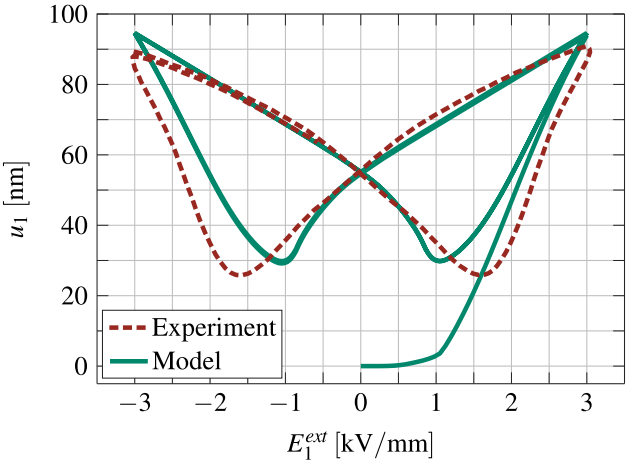


**Fig. 13.** Comparison of the butterfly hysteresis for $\delta = 65$ µm of the in-plane deformation in the global $x_1$-direction experimentally measured by Seyfert et al. (2022) with the one recorded at the point $P1$ (cf. Fig. 12) by the finite element model. For equivalent origins at the unloaded state of both curves, the experimental hysteresis is shifted.

vertical displacement is suppressed. By assuming a symmetric distribution of the electric potential, it is set to zero for every case under consideration in the symmetry plane. Excluding the gap of width $\delta$ between the electrodes a time-variant electric potential is prescribed at the top edge. The stiffness of the electrodes is neglected in this simulation. For the numerical simulations, the same material parameters were used as in Sections 6.1 and 6.2.

In the first investigation, a layout with an electrode distance of $\delta = 65$ µm is under consideration. In the experiments in Seyfert et al. (2022), a cyclic loading with an maximum nominal external electric field in between electrodes of $E_1^{ext} = 3$ kV/mm is applied. For the simulation, in the half-model, the corresponding triangular loading path of the electric potential at the top electrode is then set to $\varphi_0(t) = \{0, -97.5, 0, 97.5, 0, -97.5, 0, 97.5, 0, -97.5\}$ V subdivided into in summary 360 loading and 40 unloading equidistant steps. Seyfert et al. (2022) observed the in-plane deformation in the global $x_1$-direction at the edges of the electrodes during the whole cyclic electric loading process by using a stroboscopic motion measurement system (Voss et al., 2021, 2022). In Fig. 13 the experimentally measured butterfly hysteresis for the horizontal displacement $u_1$ is compared to the hysteresis obtained at the point $P1$ (cf. Fig. 12) in the finite element calculation. Note here, that for better comparability the experimental hysteresis, of which the initial poling curve is not reported, is shifted to the origin of the numerical hysteresis. As can be seen, the two curves are in acceptable agreement, while the minimum and maximum displacements of the stationary hystereses slightly deviate. Especially in the linear regime at low electric field intensities, which is particularly relevant for technical applications, the match is very well. A somewhat broader hysteresis in the experimental curve can be recognized.

Furthermore, we want to focus on the domain switching processes during the cyclic electric loading. To do this, a successive observation of the changes of the irreversible polarization states in the area around the electrode edge (dashed box, Fig. 12) during a reversal electric loading process for the arrangement with $\delta = 65$ mm is done. In Fig. 14 starting from a state that experienced an initial poling ($\varphi_0 = -97.5$ V, $E_1^{ext} = 3$ kV/mm) and a subsequent unloading process, the ongoing interim processes during reversal loading up to a electric potential at the top electrode of $\varphi_0 = 97.5$ V are illustrated. Here, the contours indicate the norm of the associated local irreversible polarization vector and therefore the intensity of the acting polarization in the material. The black

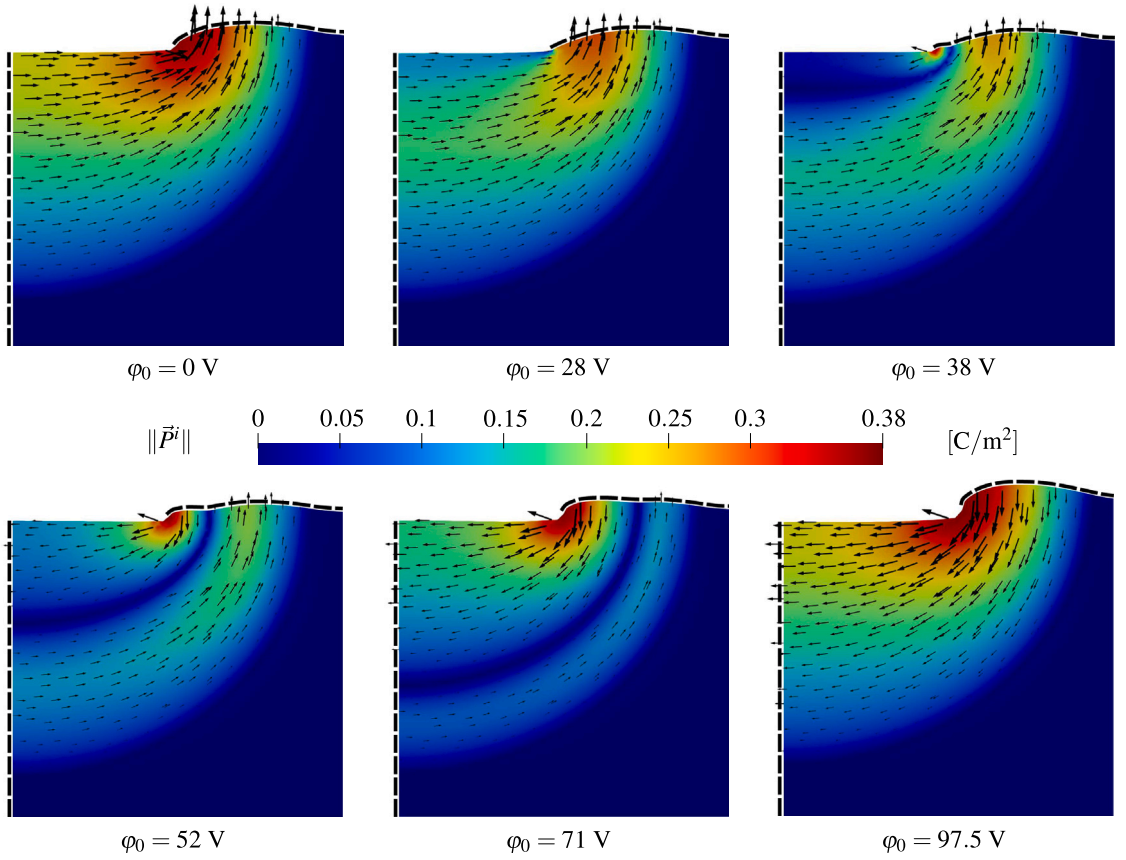


**Fig. 14.** Illustration of the irreversible polarization intensities during a reversal poling process for the wafer with an electrode distance $\delta = 65$ µm focusing on the region in the dashed box in Fig. 12. The black arrows indicate the polarization direction and the dashed lines mark the areas where the electrodes are applied. The deformation is scaled by a factor of 100.

arrows show the orientations of the irreversible polarization vectors. In this figure, the deformation patterns are scaled by a factor of 100. In the following, the processes to be observed are summarized:

**$\varphi_0 = 0$ V** ($E_1^{ext} = 0$ kV/mm): After the previous poling process, due to the acting high electric field intensities around the electrode edge, the poling process has progressed the furthest into a saturated state in this area. The preferred orientation of the polarization arises along the field lines between the two electrodes. This leads to the domains being aligned in the horizontal direction along the left boundary, while below the top contacted electrode they are aligned in the vertical direction. Due to this configuration in the left area, the material undergoes an elongation in the horizontal direction and a contraction in the vertical direction. In contrast to that, in the area below the top electrode, the material expands in the vertical direction with an accompanying contraction in the horizontal direction.

**$\varphi_0 = 28$ V** ($E_1^{ext} = -0.86$ kV/mm): By increasing a positive electric potential at the top electrode, an arising external electric field is acting in the reverse direction of the initial polarization alignment. This leads in general to a reduction of the polarization, most strongly to the left of the electrode edge which results also in a reduction in the deformation of the structure. Regions in the material that are far away from the edge of the electrode are initially not affected.

**$\varphi_0 = 38$ V** ($E_1^{ext} = -1.17$ kV/mm): With the further increased electric potential, the area to the left of the electrode edge becomes mostly polar neutralized, while directly at the edge, even an oppositely aligned polarization begins to evolve. Below the top electrode, the polarization state further decreases. The other areas continue to appear to be only slightly affected. Noteworthy to mention is that in this state the elongation in the horizontal direction in this region under consideration is nearly minimized.

**$\varphi_0 = 52$ V** ($E_1^{ext} = -1.6$ kV/mm): Starting from the edge of the electrode, the polarity of the area on the left is reversed first. In a large area, starting from the lower area of the left-hand boundary and extending in a curve-like manner to the area on the right-hand side of the edge of the upper electrode, the domains remain in their initial alignment. In between, a depolarized interface forms, which migrates from the upper edge of the structure into the material. Its influence on the deformation of the top surface is also clearly visible.

**$\varphi_0 = 71$ V** ($E_1^{ext} = -2.18$ kV/mm): The depolarized interface further propagates wave-like through the polarized area in the wafer. In the region at the top left, the polarity reversal process is already gradually coming to an end but the regions far away from this spot still have not experienced any change in the polarization state.

$\boldsymbol{\varphi_0 = 97.5\,V}$ ($E_1^{ext} = -3\,\mathrm{kV/mm}$): Reaching the maximum applied electric potential the depolarized interface went through the whole polar region in the structure and the complete initial polarization state is reversed. In this maximum loaded state, the deformations of the structure are maximized, while they are, with the exception of piezoelectric contributions, equivalent to the state shown for $\varphi_0 = 0$ V.

## 7. Conclusion

In this paper, we presented a macroscopic continuum model for ferroelectric ceramics which is thermodynamically consistently formulated as a minimum-type variational problem and at the same time able to represent all important characteristic phenomena of the material behavior in such a compact way that it can be integrated very efficiently into a finite element environment. To the best of the authors' knowledge, no model previously existed that meets all these requirements. In order to achieve this, we outlined a thermodynamically consistent theory for the material response of dissipative electro-mechanical solids. By utilizing the framework of generalized standard materials, a variational structure of the underlying problem was realized. Here, a formulation in terms of Helmholtz free energy provides a minimization problem and therefore stable material behavior. A modified version of a ferroelectric material model with microscopically motivated internal variables was introduced fitting into the variational structure of the local problem introduced before. The resulting symmetrical material tangent leads to an extremely stable and efficient solution process for the local material response.

Based on a five-field variational principle, a suitable finite element formulation was derived perfectly fitting to the introduced solution process of the Helmholtz free energy based material model. The detailed information given about the methods presented enables an easy-to-realize implementation into existing finite element codes.

In numerical examples, we demonstrated the capability of the methods presented to properly reproduce the real ferroelectric material behavior. For this purpose, the characteristic electro-mechanically coupled hystereses of PZT ceramics calculated with the outlined material model were compared to experimentally determined ones. A look at the convergence rates showed the advantages obtained by the Helmholtz free energy based variational formulation of the model, namely both quadratic convergence and pure descent in the local and global Newton iteration. A very good agreement could be achieved for a simulated polarization rotation test in comparison to experimental results from the literature. In addition, the polarization and deformation states of the specimens of the rotation test were investigated for different initial polarization angles. As a technically relevant example, the response of a PZT wafer with a single-sided parallel electrode design has been simulated under cyclic electrical loading. The in-plane deformation behavior of this system under consideration fits very well with what has been measured experimentally in the literature. A special focus is also placed on the locally resolved switching behavior in the material during a reversal poling process. The knowledge gained from such investigations can contribute significantly to an optimization process of future electrode layouts of interdigitated transducer structures.

## Declaration of competing interest

The authors declare that they have no known competing financial interests or personal relationships that could have appeared to influence the work reported in this paper.

## Data availability

Data will be made available on request.

## Acknowledgments

The financial support by the Deutsche Forschungsgemeinschaft (DFG), Germany within the project 'Converse Transduction in the Presence of Strong Electrical Field Gradients in Ferroelectrics' (project number: 391065131) is gratefully acknowledged. We also want to thank our project partners L. Seyfert and N. Schwesinger (TU Munich, Professorship of Micro-Mechatronical Systems) for the fruitful cooperation and their contribution to the work reported here.

## Appendix A. Derivatives of the free energy function

For the computational implementation of the material model introduced in Section 3 and the numerical solution process outlined in Section 4 some first- and second-order derivatives of the Helmholtz free energy are needed. To reduce the implementation work, the necessary derivations are summarized here. For a better understanding, mostly an index notation with Einstein summation convention is used. Then the Helmholtz free energy density is written as (cf. (21))

$$\begin{aligned}\psi\left(\boldsymbol{\varepsilon}, \vec{D}, \boldsymbol{A}, \vec{\rho}\right) &= \psi^r\left(\boldsymbol{\varepsilon}, \vec{D}, \boldsymbol{A}, \vec{\rho}\right) + \psi^i\left(\boldsymbol{A}, \vec{\rho}\right) \\ &= \frac{1}{2}\left(\varepsilon_{ij} - \varepsilon^i_{ij}\right) C^D_{ijkl}\left(\varepsilon_{kl} - \varepsilon^i_{kl}\right) - \left(D_k - P^i_k\right) h_{kij}\left(\varepsilon_{ij} - \varepsilon^i_{ij}\right) + \frac{1}{2}\left(D_k - P^i_k\right)\beta^\varepsilon_{kl}\left(D_l - P^i_l\right) + \psi^i\end{aligned} \tag{A.1}$$

with $C^D_{ijkl} = \mathbb{C}^D(\vec{\rho})$, $h_{kij} = \mathbb{h}(\vec{\rho})$, $\beta^\varepsilon_{kl} = \boldsymbol{\beta}^\varepsilon(\vec{\rho})$, $\varepsilon^i_{ij} = \boldsymbol{\varepsilon}^i(\boldsymbol{A}) = \frac{3}{2}\varepsilon^{sat} P^{Dev}_{ijkl} A_{kl}$ and $P^i_k = \vec{P}^i(\vec{\rho}) = P^{sat}\rho_k$, while $P^{Dev}_{ijmn} = \frac{1}{2}(\delta_{im}\delta_{jn} + \delta_{in}\delta_{jm}) - \frac{1}{3}\delta_{ij}\delta_{mn}$ ($\delta_{ij} = 1$ for $i = j$ and $\delta_{ij} = 0$ for $i \neq j$).

### A.1. First-order derivatives

$$\frac{\partial\psi}{\partial\varepsilon_{mn}} = C^D_{mnkl}\left(\varepsilon_{kl}-\varepsilon^i_{kl}\right) - h_{kmn}\left(D_k - P^i_k\right) \qquad \frac{\partial\psi}{\partial D_m} = -h_{mij}\left(\varepsilon_{ij}-\varepsilon^i_{ij}\right) + \beta^\varepsilon_{ml}\left(D_l - P^i_l\right) \tag{A.2}$$

$$\frac{\partial\psi}{\partial A_{mn}} = -\frac{3}{2}\varepsilon^{sat}\left(C^D_{ijkl}\left(\varepsilon_{kl}-\varepsilon^i_{kl}\right) - h_{kij}\left(D_k - P^i_k\right)\right)P^{Dev}_{ijmn} + \frac{\partial\psi^i}{\partial A_{mn}} \tag{A.3}$$

$$\begin{aligned}\frac{\partial\psi}{\partial\rho_m} = {}& \frac{1}{2}\left(\varepsilon_{ij}-\varepsilon^i_{ij}\right)\frac{\partial C^D_{ijkl}}{\partial\rho_m}\left(\varepsilon_{kl}-\varepsilon^i_{kl}\right) - \left(D_k - P^i_k\right)\frac{\partial h_{kij}}{\partial\rho_m}\left(\varepsilon_{ij}-\varepsilon^i_{ij}\right) + \frac{1}{2}\left(D_k - P^i_k\right)\frac{\partial\beta^\varepsilon_{kl}}{\partial\rho_m}\left(D_l - P^i_l\right)\\ & - P^{sat}\left(-h_{mij}\left(\varepsilon_{ij}-\varepsilon^i_{ij}\right) + \beta^\varepsilon_{ml}\left(D_l - P^i_l\right)\right) + \frac{\partial\psi^i}{\partial\rho_m}\end{aligned} \tag{A.4}$$

### A.2. Second-order derivatives

$$\frac{\partial^2\psi}{\partial\varepsilon_{mn}\partial\varepsilon_{op}} = C^D_{mnop} \qquad \frac{\partial^2\psi}{\partial\varepsilon_{mn}\partial D_o} = -h_{omn} \qquad \frac{\partial^2\psi}{\partial D_m\partial\varepsilon_{no}} = -h_{mno} \qquad \frac{\partial^2\psi}{\partial D_m\partial D_n} = \beta^\varepsilon_{mn} \tag{A.5}$$

$$\frac{\partial^2\psi}{\partial\varepsilon_{mn}\partial A_{op}} = -\frac{3}{2}\varepsilon^{sat}C^D_{mnkl}P^{Dev}_{klop} \qquad \frac{\partial^2\psi}{\partial\varepsilon_{mn}\partial\rho_o} = \frac{\partial C^D_{mnkl}}{\partial\rho_o}\left(\varepsilon_{kl}-\varepsilon^i_{kl}\right) - \frac{\partial h_{kmn}}{\partial\rho_o}\left(D_k - P^i_k\right) + P^{sat}h_{omn} \tag{A.6}$$

$$\frac{\partial^2\psi}{\partial D_m\partial A_{no}} = \frac{3}{2}\varepsilon^{sat}h_{mij}P^{Dev}_{ijno} \qquad \frac{\partial^2\psi}{\partial D_m\partial\rho_n} = -\frac{\partial h_{mij}}{\partial\rho_n}\left(\varepsilon_{ij}-\varepsilon^i_{ij}\right) + \frac{\partial\beta^\varepsilon_{ml}}{\partial\rho_n}\left(D_l - P^i_l\right) - P^{sat}\beta^\varepsilon_{mn} \tag{A.7}$$

$$\frac{\partial^2\psi}{\partial A_{mn}\partial A_{op}} = \frac{9}{4}(\varepsilon^{sat})^2P^{Dev}_{ijmn}C^D_{ijkl}P^{Dev}_{klop} + \frac{\partial^2\psi^i}{\partial A_{mn}\partial A_{op}} \tag{A.8}$$

$$\frac{\partial^2\psi}{\partial A_{mn}\partial\rho_o} = -\frac{3}{2}\varepsilon^{sat}\left(\frac{\partial C^D_{ijkl}}{\partial\rho_o}\left(\varepsilon_{kl}-\varepsilon^i_{kl}\right) - \frac{\partial h_{kij}}{\partial\rho_o}\left(D_k - P^i_k\right) + P^{sat}h_{oij}\right)P^{Dev}_{ijmn} + \frac{\partial^2\psi^i}{\partial A_{mn}\partial\rho_o} \tag{A.9}$$

$$\begin{aligned}\frac{\partial^2\psi}{\partial\rho_m\partial\rho_n} = {}& \frac{1}{2}\left(\varepsilon_{ij}-\varepsilon^i_{ij}\right)\frac{\partial^2C^D_{ijkl}}{\partial\rho_m\partial\rho_n}\left(\varepsilon_{kl}-\varepsilon^i_{kl}\right) - \left(D_k - P^i_k\right)\frac{\partial^2h_{kij}}{\partial\rho_m\partial\rho_n}\left(\varepsilon_{ij}-\varepsilon^i_{ij}\right) + \frac{1}{2}\left(D_k - P^i_k\right)\frac{\partial^2\beta^\varepsilon_{kl}}{\partial\rho_m\partial\rho_n}\left(D_l - P^i_l\right)\\ & - P^{sat}\left(-\frac{\partial h_{mij}}{\partial\rho_n}\left(\varepsilon_{ij}-\varepsilon^i_{ij}\right) - \frac{\partial h_{nij}}{\partial\rho_m}\left(\varepsilon_{ij}-\varepsilon^i_{ij}\right) + \frac{\partial\beta^\varepsilon_{ml}}{\partial\rho_n}\left(D_l - P^i_l\right) + \frac{\partial\beta^\varepsilon_{nl}}{\partial\rho_m}\left(D_l - P^i_l\right)\right) + (P^{sat})^2\beta^\varepsilon_{mn} + \frac{\partial^2\psi^i}{\partial\rho_m\partial\rho_n}\end{aligned} \tag{A.10}$$

### A.3. Derivatives of the irreversible part of free energy function

Some of the derivations listed here can also be found in Mehling (2007). The irreversible part of the Helmholtz free energy is given by (cf. (30))

$$\psi^i(\boldsymbol{A},\vec{\rho}) = \frac{1}{2}c_A\boldsymbol{A}^{Dev} : \boldsymbol{A}^{Dev} + \frac{1}{2}c_\rho\vec{\rho}\cdot\vec{\rho} + \psi^{iA,sat}(\boldsymbol{A}) + \psi^{i\rho,sat}(\boldsymbol{A},\vec{\rho}) \tag{A.11}$$

with the contributions which are responsible for the saturation behavior, namely

$$\psi^{iA,sat}(\boldsymbol{A}) = \frac{a_A}{m_A}\sum_{i=1}^{3}\alpha_i^{-m_A} = \frac{a_A}{m_A}\mathrm{tr}\left(\boldsymbol{A}^{-m_A}\right) \qquad \text{and} \qquad \psi^{i\rho,sat}(\boldsymbol{A},\vec{\rho}) = \frac{a_\rho}{m_\rho}(1-\eta)^{-m_\rho}. \tag{A.12}$$

First-order derivatives concerning the microscopically motivated internal state variables:

$$\frac{\partial\psi^i}{\partial\boldsymbol{A}} = c_A\mathbb{P}^{Dev} : \boldsymbol{A} - a_A\boldsymbol{A}^{-m_A-1} + a_\rho(1-\eta)^{-m_\rho-1}\frac{\partial\eta}{\partial\boldsymbol{A}} \qquad \frac{\partial\psi^i}{\partial\vec{\rho}} = c_\rho\vec{\rho} + a_\rho(1-\eta)^{-m_\rho-1}\frac{\partial\eta}{\partial\vec{\rho}} \tag{A.13}$$

Second-order derivatives concerning the microscopically motivated internal state variables:

$$\frac{\partial^2\psi^i}{\partial\boldsymbol{A}^2} = c_A\mathbb{P}^{Dev} + \frac{\partial^2\psi^{iA,sat}}{\partial\boldsymbol{A}^2} + a_\rho(m_\rho+1)(1-\eta)^{-m_\rho-2}\frac{\partial\eta}{\partial\boldsymbol{A}}\otimes\frac{\partial\eta}{\partial\boldsymbol{A}} + a_\rho(1-\eta)^{-m_\rho-1}\frac{\partial^2\eta}{\partial\boldsymbol{A}^2} \tag{A.14}$$

with

$$\frac{\partial^2\psi^{iA,sat}}{\partial\boldsymbol{A}^2} = \sum_{i=1}^{3}\sum_{j=1}^{3}\begin{cases} a_A(m_A+1)\,\alpha_i^{-m_A-2}\,\vec{e}_i^{\,A}\otimes\vec{e}_i^{\,A}\otimes\vec{e}_i^{\,A}\otimes\vec{e}_i^{\,A} & ,i=j \\ \dfrac{1}{2}\dfrac{-a_A\alpha_j^{-m_A-1}+a_A\alpha_i^{-m_A-1}}{\alpha_j-\alpha_i}\left(\vec{e}_i^{\,A}\otimes\vec{e}_j^{\,A}\otimes\vec{e}_i^{\,A}\otimes\vec{e}_j^{\,A}+\vec{e}_i^{\,A}\otimes\vec{e}_j^{\,A}\otimes\vec{e}_j^{\,A}\otimes\vec{e}_i^{\,A}\right) & ,i\neq j,\quad \alpha_i\neq\alpha_j \\ \dfrac{1}{2}a_A(m_A+1)\,\alpha_i^{-m_A-2}\left(\vec{e}_i^{\,A}\otimes\vec{e}_j^{\,A}\otimes\vec{e}_i^{\,A}\otimes\vec{e}_j^{\,A}+\vec{e}_i^{\,A}\otimes\vec{e}_j^{\,A}\otimes\vec{e}_j^{\,A}\otimes\vec{e}_i^{\,A}\right) & ,i\neq j,\quad \alpha_i=\alpha_j \end{cases} \tag{A.15}$$

while $\alpha_i$ and $\vec{e}_i^A$ are the eigenvalues and the eigenvectors of the texture tensor. Note that the subscripts in (A.15) correspond to the number of the eigenvalues of $\boldsymbol{A}$. The derivative can be found e.g. in Ogden (1997) p. 162.

$$\frac{\partial^2\psi^i}{\partial\boldsymbol{A}\partial\vec{\rho}} = a_\rho(m_\rho+1)(1-\eta)^{-m_\rho-2}\frac{\partial\eta}{\partial\boldsymbol{A}}\otimes\frac{\partial\eta}{\partial\vec{\rho}} + a_\rho(1-\eta)^{-m_\rho-1}\frac{\partial^2\eta}{\partial\boldsymbol{A}\partial\vec{\rho}} \tag{A.16}$$

$$\frac{\partial^2\psi^i}{\partial\vec{\rho}^2} = c_\rho\boldsymbol{I} + a_\rho(m_\rho+1)(1-\eta)^{-m_\rho-2}\frac{\partial\eta}{\partial\vec{\rho}}\otimes\frac{\partial\eta}{\partial\vec{\rho}} + a_\rho(1-\eta)^{-m_\rho-1}\frac{\partial^2\eta}{\partial\vec{\rho}^2} \tag{A.17}$$

### *A.4. Derivatives of the distance variable*

The distance variable is given by (cf. (32))

$$\eta = B_{ij}\rho_j B_{ik}\rho_k \qquad \text{with} \quad B_{ij} = \left(\xi\delta_{ij} + (1-\xi)A_{ij}\right)^{-1}. \tag{A.18}$$

The first-order derivatives of the distance variable are

$$\frac{\partial\eta}{\partial A_{ij}} = -(1-\xi)\left(\hat{b}_i b_j + \hat{b}_j b_i\right) \qquad \text{and} \qquad \frac{\partial\eta}{\partial\rho_i} = 2\hat{b}_i, \qquad \text{with} \qquad b_i = B_{ij}\rho_j \qquad \text{and} \qquad \hat{b}_i = B_{ij}b_j. \tag{A.19}$$

Second-order derivatives of the distance variable:

$$\begin{aligned}\frac{\partial^2\eta}{\partial A_{ij}\partial A_{kl}} = \frac{1}{2}(1-\xi)^2\,\big(&\hat{B}_{ik}b_j b_l + \hat{B}_{il}b_j b_k + b_i b_k\hat{B}_{jl} + b_i b_l\hat{B}_{jk} + \hat{b}_i b_k B_{jl} + \hat{b}_i b_l B_{jk} + b_i\hat{b}_k B_{jl} + b_i\hat{b}_l B_{jk}\\ &+ B_{ik}\hat{b}_j b_l + B_{il}\hat{b}_j b_k + B_{ik}b_j\hat{b}_l + B_{il}b_j\hat{b}_k\big) \qquad \text{with} \qquad \hat{B}_{ij} = B_{ki}B_{kj}\end{aligned} \tag{A.20}$$

$$\frac{\partial^2\eta}{\partial\rho_i\partial\rho_j} = 2\hat{B}_{ij} \qquad \frac{\partial^2\eta}{\partial A_{ij}\partial\rho_k} = -(1-\xi)\left(B_{ki}\hat{b}_j + B_{kj}\hat{b}_i + \hat{B}_{ki}b_j + \hat{B}_{kj}b_i\right) \tag{A.21}$$

## Appendix B. Derivatives of material tensors

The derivatives of the material tensors used in Appendix A are summarized here.
Piezoelectric d-tensor (cf. (25)):

$$d_{kij} = \left(d_{33}-d_{31}-d_{15}\right)\rho_k\rho_i\rho_j + d_{31}\rho_k\delta_{ij} + \frac{1}{2}d_{15}\left(\delta_{ki}\rho_j + \delta_{kj}\rho_i\right) \tag{B.1}$$

$$\frac{\partial d_{kij}}{\partial\rho_l} = \left(d_{33}-d_{31}-d_{15}\right)\left(\delta_{kl}\rho_i\rho_j + \rho_k\delta_{il}\rho_j + \rho_k\rho_i\delta_{jl}\right) + d_{31}\delta_{ij}\delta_{kl} + \frac{1}{2}d_{15}\left(\delta_{ki}\delta_{jl} + \delta_{kj}\delta_{il}\right) \tag{B.2}$$

$$\frac{\partial^2 d_{kij}}{\partial\rho_l\partial\rho_m} = \left(d_{33}-d_{31}-d_{15}\right)\left(\delta_{kl}\delta_{im}\rho_j + \delta_{kl}\rho_i\delta_{jm} + \delta_{km}\delta_{il}\rho_j + \rho_k\delta_{il}\delta_{jm} + \delta_{km}\rho_i\delta_{jl} + \rho_k\delta_{im}\delta_{jl}\right) \tag{B.3}$$

Impermitivity tensor at constant strain (cf. (24)):

$$\beta_{ij}^\varepsilon = \left(\epsilon_{ij}^\sigma - d_{ikl}C_{klmn}^E d_{jmn}\right)^{-1} = \left(\epsilon_{ij}^\varepsilon\right)^{-1} \tag{B.4}$$

$$\frac{\partial\beta_{ij}^\varepsilon}{\partial\rho_o} = -\beta_{ip}^\varepsilon\frac{\partial\epsilon_{pq}^\varepsilon}{\partial\rho_o}\beta_{qj}^\varepsilon \qquad \text{with} \qquad \frac{\partial\epsilon_{ij}^\varepsilon}{\partial\rho_o} = -\left(\frac{\partial d_{ikl}}{\partial\rho_o}d_{jmn} + d_{ikl}\frac{\partial d_{jmn}}{\partial\rho_o}\right)C_{klmn}^E \tag{B.5}$$

$$\begin{aligned}\frac{\partial^2\beta_{ij}^\varepsilon}{\partial\rho_o\partial\rho_r} &= -\frac{\partial\beta_{ip}^\varepsilon}{\partial\rho_r}\frac{\partial\epsilon_{pq}^\varepsilon}{\partial\rho_o}\beta_{qj}^\varepsilon - \beta_{ip}^\varepsilon\frac{\partial^2\epsilon_{pq}^\varepsilon}{\partial\rho_o\partial\rho_r}\beta_{qj}^\varepsilon - \beta_{ip}^\varepsilon\frac{\partial\epsilon_{pq}^\varepsilon}{\partial\rho_o}\frac{\partial\beta_{qj}^\varepsilon}{\partial\rho_r}\\ \text{with} \quad \frac{\partial^2\epsilon_{ij}^\varepsilon}{\partial\rho_o\partial\rho_p} &= -\left(\frac{\partial^2 d_{ikl}}{\partial\rho_o\partial\rho_p}d_{jmn} + \frac{\partial d_{ikl}}{\partial\rho_o}\frac{\partial d_{jmn}}{\partial\rho_p} + \frac{\partial d_{ikl}}{\partial\rho_p}\frac{\partial d_{jmn}}{\partial\rho_o} + d_{ikl}\frac{\partial^2 d_{jmn}}{\partial\rho_o\partial\rho_p}\right)C_{klmn}^E\end{aligned} \tag{B.6}$$

Piezoelectric h-tensor (cf. (23)):

$$h_{kij} = \beta_{kl}^\varepsilon d_{lmn}C_{mnij}^E \tag{B.7}$$

$$\frac{\partial h_{kij}}{\partial\rho_o} = \left(\frac{\partial\beta_{kl}^\varepsilon}{\partial\rho_o}d_{lmn} + \beta_{kl}^\varepsilon\frac{\partial d_{lmn}}{\partial\rho_o}\right)C_{mnij}^E \tag{B.8}$$

$$\frac{\partial^2 h_{kij}}{\partial\rho_o\partial\rho_p} = \left(\frac{\partial^2\beta_{kl}^\varepsilon}{\partial\rho_o\partial\rho_p}d_{lmn} + \frac{\partial\beta_{kl}^\varepsilon}{\partial\rho_o}\frac{\partial d_{lmn}}{\partial\rho_p} + \frac{\partial\beta_{kl}^\varepsilon}{\partial\rho_p}\frac{\partial d_{lmn}}{\partial\rho_o} + \beta_{kl}^\varepsilon\frac{\partial^2 d_{lmn}}{\partial\rho_o\partial\rho_p}\right)C_{mnij}^E \tag{B.9}$$

Elasticity tensor at constant electric displacement (cf. (22)):

$$C_{ijkl}^D = C_{ijkl}^E + d_{mno}C_{noij}^E h_{mkl} \tag{B.10}$$

$$\frac{\partial C_{ijkl}^D}{\partial\rho_p} = \left(\frac{\partial d_{mno}}{\partial\rho_p}h_{mkl} + d_{mno}\frac{\partial h_{mkl}}{\partial\rho_p}\right)C_{noij}^E \tag{B.11}$$

$$\frac{\partial^2 C_{ijkl}^D}{\partial\rho_p\partial\rho_q} = \left(\frac{\partial^2 d_{mno}}{\partial\rho_p\partial\rho_q}h_{mkl} + \frac{\partial d_{mno}}{\partial\rho_p}\frac{\partial h_{mkl}}{\partial\rho_q} + \frac{\partial d_{mno}}{\partial\rho_q}\frac{\partial h_{mkl}}{\partial\rho_p} + d_{mno}\frac{\partial^2 h_{mkl}}{\partial\rho_p\partial\rho_q}\right)C_{noij}^E \tag{B.12}$$

## Appendix C. Derivatives of switching function

For the numerical solution process of the material model described in Section 4 the derivatives of the switching functions are needed, cf. (38) and (41). The switching function is given by

$$f = \frac{(\mathbf{f}^A)^{Dev} : (\mathbf{f}^A)^{Dev}}{(\mathrm{f}_c^A)^2} + \frac{\vec{\mathrm{f}}^{\rho} \cdot \vec{\mathrm{f}}^{\rho}}{(\mathrm{f}_c^{\rho})^2} - 1. \tag{C.1}$$

First- and second-order derivatives of the switching function:

$$\frac{\partial f}{\partial \mathbf{f}^A} = \frac{2}{(\mathrm{f}_c^A)^2} \mathbb{P}^{Dev} : \mathbf{f}^A \qquad \frac{\partial f}{\partial \vec{\mathrm{f}}^{\rho}} = \frac{2}{(\mathrm{f}_c^{\rho})^2} \vec{\mathrm{f}}^{\rho} \qquad \frac{\partial^2 f}{\partial \mathbf{f}^{A\,2}} = \frac{2}{(\mathrm{f}_c^A)^2} \mathbb{P}^{Dev} \qquad \frac{\partial^2 f}{\partial \vec{\mathrm{f}}^{\rho\,2}} = \frac{2}{(\mathrm{f}_c^{\rho})^2} \boldsymbol{I} \tag{C.2}$$

## References


Allik, H., Hughes, T.J., 1970. Finite element method for piezoelectric vibration. Internat. J. Numer. Methods Engrg. 2 (2), 151–157.

Bassiouny, E., Ghaleb, A.F., Maugin, G.A., 1988. Thermodynamical formulation for coupled electromechanical hysteresis effects—I. Basic equations. Internat. J. Engrg. Sci. 26 (12), 1279–1295.

Bassiouny, E., Maugin, G.A., 1989. Thermodynamical formulation for coupled electromechanical hysteresis effects—IV. Combined electromechanical loading. Internat. J. Engrg. Sci. 27 (8), 989–1000.

Benjeddou, A., 2000. Advances in piezoelectric finite element modeling of adaptive structural elements: a survey. Comput. Struct. 76 (1–3), 347–363.

Berlincourt, D., Jaffe, H., 1958. Elastic and piezoelectric coefficients of single-crystal barium titanate. Phys. Rev. 111 (1), 143–148.

Biot, M.A., 1965. Mechanics of Incremental Deformations. Wiley, New York.

Cannarozzi, A.A., Ubertini, F., 2001. Some hybrid variational methods for linear electroelasticity problems. Int. J. Solids Struct. 38 (15), 2573–2596.

Cao, H., Evans, A.G., 1993. Nonlinear deformation of ferroelectric ceramics. J. Am. Ceram. Soc. 76 (4), 890–896.

Cocks, A.C., McMeeking, R.M., 1999. A phenomenological constitutive law for the behaviour of ferroelectric ceramics. Ferroelectrics 228 (1), 219–228.

Coleman, B.D., Gurtin, M.E., 1967. Thermodynamics with internal state variables. J. Chem. Phys. 47 (2), 597–613.

de Oliveira, O., 2014. The implicit and the inverse function theorems: easy proofs. Real Anal. Exch. 39 (1), 207–218.

Elhadrouz, M., Zineb, T.B., Patoor, E., 2005. Constitutive law for ferroelastic and ferroelectric piezoceramics. J. Intell. Mater. Syst. Struct. 16 (3), 221–236.

Elhadrouz, M., Zineb, T.B., Patoor, E., 2006. Finite element analysis of a multilayer piezoelectric actuator taking into account the ferroelectric and ferroelastic behaviors. Internat. J. Engrg. Sci. 44 (15–16), 996–1006.

Fassin, M., Eggersmann, R., Wulfinghoff, S., Reese, S., 2018. A numerically robust anisotropic damage model. Proc. Appl. Math. Mech. 18 (1).

Fett, T., Munz, D., Thun, G., 2002. Young's modulus of soft PZT from partial unloading tests. Ferroelectrics 274 (1), 67–81.

Franke, M., Ortigosa, R., Janz, A., Gil, A.J., Betsch, P., 2019. A mixed variational framework for the design of energy–momentum integration schemes based on convex multi-variable electro-elastodynamics. Comput. Methods Appl. Mech. Engrg. 351, 109–152.

Fröhlich, A., 2001. Mikromechanisches Modell zur Ermittlung effektiver Materialeigenschaften von piezoelektrischen Polykristallen. Scientific report FZKA 6828, Forschungszentrum Karlsruhe.

Ghandi, K., Hagood, N.W., 1997. Hybrid finite element model for phase transitions in nonlinear electromechanically coupled material. In: Proc. of SPIE. Vol. 3039, pp. 97–112.

Gil, A.J., Ortigosa, R., 2016. A new framework for large strain electromechanics based on convex multi-variable strain energies: Variational formulation and material characterisation. Comput. Methods Appl. Mech. Engrg. 302, 293–328.

Gruttmann, F., Stein, E., 1988. Tangentiale Steifigkeitsmatrizen bei Anwendung von Projektionsverfahren in der Elastoplastizitätstheorie. Ing.-Arch. 58 (1), 15–24.

Halphen, B., Nguyen, Q.S., 1975. Sur les Matéraux Standards Généralisés. Journal de Mécanique 40, 39–63.

Hill, R., 1950. The Mathematical Theory of Plasticity. Claredon Press, Oxford.

Hu, H.C., 1955. On some variational principles in the theory of elasticity and plasticity. Sci. Sin. 4, 33–54.

Huber, J.E., Fleck, N.A., 2001. Multi-axial electrical switching of a ferroelectric: theory versus experiment. J. Mech. Phys. Solids 49 (4), 785–811.

Huber, J.E., Fleck, N.A., Landis, C.M., McMeeking, R.M., 1999. A constitutive model for ferroelectric polycrystals. J. Mech. Phys. Solids 47 (8), 1663–1697.

Hwang, S.C., Lynch, C.S., McMeeking, R.M., 1995. Ferroelectric/ferroelastic interactions and a polarization switching model. Acta Metall. Mater. 43 (5), 2073–2084.

Idiart, M.I., Bottero, C.J., 2020. A phenomenological constitutive theory for polycrystalline ferroelectric ceramics based on orientation distribution functions. Eur. J. Mech. A Solids 82, 103982.

Ikeda, T., 1996. Fundamentals of Piezoelectricity. Oxford University Press.

Jaffe, B., Cook, W.R., Jaffe, H., 1971. Piezoelectric Ceramics. Academic Press, London, New York.

Kamlah, M., 2001. Ferroelectric and ferroelastic piezoceramics - modeling of electromechanical hysteresis phenomena. Contin. Mech. Thermodyn. 4 (13), 219–268.

Kamlah, M., Böhle, U., 2001. Finite element analysis of piezoceramic components taking into account ferroelectric hysteresis behavior. Int. J. Solids Struct. 38 (4), 605–633.

Kamlah, M., Jiang, Q., 1999. A constitutive model for ferroelectric PZT ceramics under uniaxial loading. Smart Mater. Struct. 8 (4), 441–459.

Kamlah, M., Tsakmakis, C., 1999. Phenomenological modeling of the non-linear electro-mechanical coupling in ferroelectrics. Int. J. Solids Struct. 36 (5), 669–695.

Kamlah, M., Wang, Z., 2003a. A thermodynamically and microscopically motivated constitutive model for piezoceramics. Comput. Mater. Sci. 28 (3–4), 409–418.

Kamlah, M., Wang, Z., 2003b. A thermodynamically and microscopically motivated constitutive model for piezoceramics. Scientific report FZKA 6880, Forschungszentrum Karlsruhe.

Kessler, H., Balke, H., 2001. On the local and average energy release in polarization switching phenomena. J. Mech. Phys. Solids 49 (5), 953–978.

Klinkel, S., 2006a. A phenomenological constitutive model for ferroelastic and ferroelectric hysteresis effects in ferroelectric ceramics. Int. J. Solids Struct. 43 (22–23), 7197–7222.

Klinkel, S., 2006b. A thermodynamic consistent 1D model for ferroelastic and ferroelectric hysteresis effects in piezoceramics. Commun. Numer. Methods. Eng. 22 (7), 727–739.

Klinkel, S., Wagner, W., 2006. A geometrically non-linear piezoelectric solid shell element based on a mixed multi-field variational formulation. Internat. J. Numer. Methods Engrg. 65 (3), 349–382.

Klinkel, S., Wagner, W., 2008. A piezoelectric solid shell element based on a mixed variational formulation for geometrically linear and nonlinear applications. Comput. Struct. 86 (1–2), 38–46.

Kurzhöfer, I., Schröder, J., 2006. A hybrid element formulation for electromechanical problems. Proc. Appl. Math. Mech. 6, 451–452.

Landis, C.M., 2002a. Fully coupled, multi-axial, symmetric constitutive laws for polycrystalline ferroelectric ceramics. J. Mech. Phys. Solids 50 (1), 127–152.

Landis, C.M., 2002b. A new finite-element formulation for electromechanical boundary value problems. Internat. J. Numer. Methods Engrg. 55 (5), 613–628.

Landis, C.M., 2004. Non-linear constitutive modeling of ferroelectrics. Curr. Opin. Solid State Mater. Sci. 8 (1), 59–69.
Landis, C.M., Wang, J., Sheng, J., 2004. Micro-electromechanical determination of the possible remanent strain and polarization states in polycrystalline ferroelectrics and the implications for phenomenological constitutive theories. J. Intell. Mater. Syst. Struct. 15 (7), 513–525.
Laskewitz, B., 2007. Finite-Elemente-Implementierung konstitutiver nichtlinearer Stoffgesetze für piezokeramische Werkstoffe. Scientific report FZKA 7359, Forschungszentrum Karlsruhe.
Laskewitz, B., Kamlah, M., 2010. Finite element implementation of nonlinear constitutive models for piezoceramic materials. J. Mech. Mater. Struct. 5 (1), 19–45.
Laxman, L.V., Maniprakash, S., Arockiarajan, A., 2018. A phenomenological model for nonlinear hysteresis and creep behaviour of ferroelectric materials. Acta Mech. 229 (9), 3853–3867.
Linnemann, K., 2008. Magnetostriktive und piezoelektrische materialien: Konstitutive Modellierung und Finite-Element-Formulierung. (Dissertation). Institut für Baustatik, Universität Karlsruhe (TH).
Linnemann, K., Klinkel, S., Wagner, W., 2009. A constitutive model for magnetostrictive and piezoelectric materials. Int. J. Solids Struct. 46 (5), 1149–1166.
Lu, W., Fang, D.N., Li, C.Q., Hwang, K.C., 1999. Nonlinear electric–mechanical behavior and micromechanics modelling of ferroelectric domain evolution. Acta Mater. 47 (10), 2913–2926.
Lubliner, J., 1972. On the thermodynamic foundations of non-linear solid mechanics. Int. J. Non-Linear Mech. 7 (3), 237–254.
Lubliner, J., 1984. A maximum-dissipation principle in generalized plasticity. Acta Mech. 52 (3), 225–237.
Lynch, C.S., 1996. The effect of uniaxial stress on the electro-mechanical response of 8/65/35 PLZT. Acta Mater. 44 (10), 4137–4148.
MacNeal, R.H., Harder, R.L., 1985. A proposed standard set of problems to test finite element accuracy. Finite Elem. Anal. Des. 1 (1), 3–20.
Maniprakash, S., 2016. Phenomenological modelling and simulation of ferroelectric ceramics. (Dissertation). TU Dortmund.
Maniprakash, S., Arockiarajan, A., Menzel, A., 2016a. A multi-surface model for ferroelectric ceramics-application to cyclic electric loading with changing maximum amplitude. Phil. Mag. 96 (13), 1263–1284.
Maniprakash, S., Jayendiran, R., Menzel, A., Arockiarajan, A., 2016b. Experimental investigation, modelling and simulation of rate-dependent response of 1–3 ferroelectric composites. Mech. Mater. 94, 91–105.
MATLAB, 2022. Version 9.12.0.1884302 (R2022a). The MathWorks Inc., Natick, Massachusetts.
Maugin, G.A., 1988. Continuum Mechanics of Electromagnetic Solids. North-Holland, Amsterdam.
Maugin, G.A., 1993. Non-equilibrium thermodynamics of electromagnetic solids. In: Muschik, W. (Ed.), Non-Equilibrium Thermodynamics with Application to Solids. In: CISM Courses and Lectures, Vol. 336, Springer, Vienna, pp. 205–258.
McMeeking, R.M., Landis, C.M., 2002. A phenomenological multi-axial constitutive law for switching in polycrystalline ferroelectric ceramics. Internat. J. Engrg. Sci. 40 (14), 1553–1577.
Mehling, V., 2007. Phenomenological modeling of ferroelectric material behavior. Research Report, Vol. 15, Institut für Mechanik, Technischen Universität Darmstadt.
Mehling, V., Tsakmakis, C., Gross, D., 2007. Phenomenological model for the macroscopical material behavior of ferroelectric ceramics. J. Mech. Phys. Solids 55 (10), 2106–2141.
Meindlhumer, M., Pechstein, A., Humer, A., 2021. Variational inequalities for ferroelectric constitutive modeling. J. Intell. Mater. Syst. Struct. 32 (3), 317–330.
Miehe, C., 2002. Strain-driven homogenization of inelastic microstructures and composites based on an incremental variational formulation. Internat. J. Numer. Methods Engrg. 55 (11), 1285–1322.
Miehe, C., Rosato, D., 2011. A rate-dependent incremental variational formulation of ferroelectricity. Internat. J. Engrg. Sci. 49 (6), 466–496.
Miehe, C., Rosato, D., Kiefer, B., 2011. Variational principles in dissipative electro-magneto-mechanics: A framework for the macro-modeling of functional materials. Internat. J. Numer. Methods Engrg. 86 (10), 1225–1276.
Miehe, C., Vallicotti, D., Zäh, D., 2015. Computational structural and material stability analysis in finite electro-elasto-statics of electro-active materials. Internat. J. Numer. Methods Engrg. 102 (10), 1605–1637.
Mielke, A., Timofte, A.M., 2006. An energetic material model for time-dependent ferroelectric behaviour: existence and uniqueness. Math. Methods Appl. Sci. 29 (12), 1393–1410.
Moulson, A.J., Herbert, J.M., 1990. Electroceramics: Materials, Properties, Applications. Chapman & Hall, London, New York.
Ogden, R.W., 1997. Non-Linear Elastic Deformations. Courier Corporation, Dover.
Ortigosa, R., Gil, A.J., 2016. A new framework for large strain electromechanics based on convex multi-variable strain energies: Finite element discretisation and computational implementation. Comput. Methods Appl. Mech. Engrg. 302, 329–360.
Ortiz, M., Simo, J.C., 1986. An analysis of a new class of integration algorithms for elastoplastic constitutive relations. Internat. J. Numer. Methods Engrg. 23 (3), 353–366.
Ortiz, M., Stainier, L., 1999. The variational formulation of viscoplastic constitutive updates. Comput. Methods Appl. Mech. Engrg. 171 (3–4), 419–444.
Pechstein, A.S., Meindlhumer, M., Humer, A., 2018. New mixed finite elements for the discretization of piezoelectric structures or macro-fiber composites. J. Intell. Mater. Syst. Struct. 29 (16), 3266–3283.
Pechstein, A.S., Meindlhumer, M., Humer, A., 2020. The polarization process of ferroelectric materials in the framework of variational inequalities. Z. Angew. Math. Mech. 100 (6), e201900329.
Pechstein, A.S., Meindlhumer, M., Humer, A., 2021. High-order mixed finite elements for an energy-based model of the polarization process in ferroelectric materials. J. Intell. Mater. Syst. Struct. 32 (3), 355–368.
PI Ceramic GmbH, 2016. Piezoelectric Ceramic Products: Fundamentals, Characteristics and Applications. Lederhose, Germany.
Radovitzky, R., Ortiz, M., 1999. Error estimation and adaptive meshing in strongly nonlinear dynamic problems. Comput. Methods Appl. Mech. Engrg. 172 (1–4), 203–240.
Schröder, J., Gross, D., 2004. Invariant formulation of the electromechanical enthalpy function of transversely isotropic piezoelectric materials. Arch. Appl. Mech. 73 (8), 533–552.
Schröder, J., Romanowski, H., 2005. A thermodynamically consistent mesoscopic model for transversely isotropic ferroelectric ceramics in a coordinate-invariant setting. Arch. Appl. Mech. 74 (11), 863–877.
Schwaab, H., Grünbichler, H., Supancic, P., Kamlah, M., 2012. Macroscopical non-linear material model for ferroelectric materials inside a hybrid finite element formulation. Int. J. Solids Struct. 49 (3–4), 457–469.
Semenov, A.S., Kessler, H., Liskowsky, A., Balke, H., 2006. On a vector potential formulation for 3D electromechanical finite element analysis. Commun. Numer. Methods. Eng. 22 (5), 357–375.
Semenov, A.S., Liskowsky, A.C., Balke, H., 2010. Return mapping algorithms and consistent tangent operators in ferroelectroelasticity. Internat. J. Numer. Methods Engrg. 81 (10), 1298–1340.
Setter, N., Waser, R., 2000. Electroceramic materials. Acta Mater. 48 (1), 151–178.
Seyfert, L., Voss, A., Hemmert, W., Schwesinger, N., 2022. Contribution of converse flexoelectric effect in PZT ceramics in presence of strong electrical fields. In: Proc. of SPIE 12043. 120430L-1-13.
Simo, J.C., Honein, T., 1990. Variational formulation, discrete conservation laws, and path-domain independent integrals for elasto-viscoplasticity. J. Appl. Mech. 57 (3), 488–497.
Simo, J.C., Taylor, R.L., 1985. Consistent tangent operators for rate-independent elastoplasticity. Comput. Methods Appl. Mech. Engrg. 48 (1), 101–118.

Stark, S., Neumeister, P., Balke, H., 2016. Some aspects of macroscopic phenomenological material models for ferroelectroelastic ceramics. Int. J. Solids Struct. 80, 359–367.
Stark, S., Neumeister, P., Balke, H., 2016a. A hybrid phenomenological model for ferroelectroelastic ceramics. Part I: Single phased materials. J. Mech. Phys. Solids 95, 774–804.
Stark, S., Neumeister, P., Balke, H., 2016b. A hybrid phenomenological model for ferroelectroelastic ceramics. Part II: Morphotropic PZT ceramics. J. Mech. Phys. Solids 95, 805–826.
Stark, S., Roth, S., Neumeister, P., Balke, H., 2013. Modifications of the Newton–Raphson method for finite element simulations in ferroelectroelasticity. Int. J. Solids Struct. 50 (5), 773–780.
Stark, S., Semenov, A.S., Balke, H., 2015. On the boundary conditions for the vector potential formulation in electrostatics. Internat. J. Numer. Methods Engrg. 102 (11), 1704–1732.
Streich, F.A., Martin, A., Webber, K.G., Kamlah, M., 2022. Macroscopic constitutive model for ergodic and non-ergodic lead-free relaxors. J. Intell. Mater. Syst. Struct. 33 (8), 1002–1017.
Su, Y., Landis, C.M., 2007. Continuum thermodynamics of ferroelectric domain evolution: Theory, finite element implementation, and application to domain wall pinning. J. Mech. Phys. Solids 55 (2), 280–305.
Sze, K.Y., Pan, Y.S., 1999. Hybrid finite element models for piezoelectric materials. J. Sound Vib. 226 (3), 519–547.
Vogel, F., Bustamante, R., Steinmann, P., 2012. On some mixed variational principles in electro-elastostatics. Int. J. Non-Linear Mech. 47 (2), 341–354.
Voss, A., Seyfert, L., Hemmert, W., 2021. Stroboscopic video microscopy for in-plane motion measurements up to 2 MHz with picometer resolution. In: IEEE 34th Intern. Conf. on MEMS. pp. 1040–1043.
Voss, A., Seyfert, L., Schwesinger, N., Hemmert, W., 2022. Stroboscopic video microscopy with sub-nanometer accuracy for characterizing and monitoring MEMS. In: Proc. of SPIE 12047. 1204712-1-5.
Wang, J., Shi, S.Q., Chen, L.Q., Li, Y., Zhang, T.Y., 2004. Phase-field simulations of ferroelectric/ferroelastic polarization switching. Acta Mater. 52 (3), 749–764.
Washizu, K., 1955. On the variational principles of elasticity and plasticity. In: Aeroelastic and Structures Research Laboratory. Technical Report 25-18, MIT, Cambridge.
Wilkins, M.L., 1964. Calculation of elastic plastic flow. In: Alder, B., Fernbach, S., Rotenberg, M. (Eds.), Methods in Computational Physics. Vol. 3, Academic Press, New York, pp. 271–277.
Wriggers, P., 2008. Nonlinear Finite Element Methods. Springer-Verlag, Berlin, Heidelberg.
Zähringer, S., Menacher, M., Kirchner, P., Schwesinger, N., 2010. Normally closed piezoelectric micro valve. In: 2010 Symposium on Design Test Integration and Packaging of MEMS/MOEMS. DTIP, pp. 105–109.
Zähringer, S., Purr, J., Schwesinger, N., 2014. Manipulation of IDT-actuated piezoelectric membrane actuators by silicon clamping. Appl. Mech. Mater. 518, 215–219.
Zhou, D., 2003. Experimental investigation of non-linear constitutive behavior of PZT piezoceramics. Scientific report FZKA 6869, Forschungszentrum Karlsruhe.
Zhou, D., Kamlah, M., Gan, Y., Laskewitz, B., 2006a. Time-dependent nonlinear ferroelastic behaviour of soft lead zirconate titanate piezoceramics. Adv. Sci. Technol. 45, 2464–2471.
Zhou, D., Kamlah, M., Laskewitz, B., 2006b. Multi-axial non-proportional polarization rotation tests of soft PZT piezoceramics under electric field loading. In: Proc. of SPIE 6170. 617009–1-9.
Zhou, D., Kamlah, M., Munz, D., 2005a. Effects of bias electric fields on the non-linear ferroelastic behavior of soft lead zirconate titanate piezoceramics. J. Am. Ceram. Soc. 88 (4), 867–874.
Zhou, D., Kamlah, M., Munz, D., 2005b. Effects of uniaxial prestress on the ferroelectric hysteretic response of soft PZT. J. Eur. Ceram. Soc. 25 (4), 425–432.
Zhou, D., Wang, R., Kamlah, M., 2010. Determination of reversible and irreversible contributions to the polarization and strain response of soft PZT using the partial unloading method. J. Eur. Ceram. Soc. 30 (12), 2603–2615.
Zienkiewicz, O.C., Taylor, R.L., Zhu, J.Z., 2005. The Finite Element Method: Its Basis and Fundamentals, Sixth Edition. Elsevier, Butterworth-Heinemann, Oxford.
Zouari, W., Zineb, T.B., Benjeddou, A., 2011. A ferroelectric and ferroelastic 3D hexahedral curvilinear finite element. Int. J. Solids Struct. 48 (1), 87–109.